CHAPTER 3

RESULTS AND DISCUSSION

3.1 CdS synthesized by a HEC-assisted solvothermal method

3.1.1 X-ray diffraction (XRD)

XRD pattern of the products (Figure. 3.1-3.10) synthesized using different condition were indexed using Bragg's equation, and compared with that of the JCPDS software (reference code 41-1019) [109]. The products produced at different temperatures (Figure 3.1-3.6) were identified as CdS (hcp) with $P6_3mc$ space group. At 100 ^{o}C and 24 h solvothermal reaction, the spectrum is broad, showing that the product was composed of a number of nanoparticles. At higher solvothermal temperatures, the spectra became sharper and narrower, and the intensities were stronger. As a result, we can ascribe that the degree of crystallinity continuously increased with an increase in solvothermal temperatures. Crystallite sizes were also enlarged. At 100 ^{o}C, the (002) peak was the most dominant, relative to those of the (100) and (101). This may be due to high crystalline ordering nucleated along the *c*-axis and random ordering in the *x*–*y* planes [110]. It became less dominant at higher temperatures. The (100) and (101) peaks increased at faster rates than the (002) peak. Product crystallinity in the x–y planes developed along with the preferred orientation in the c-axis [110]. The I_{002}/I_{100} and I_{002}/I_{101} intensity ratios are the specification of the preferential growth along the c-axis. Two peaks diffracting from the (102) and (103) planes of the nanocrystals at 2θ of 36.62 and 47.84^{o} are the characteristics of hcp

phase [111]. Calculated lattice parameters for hcp structure are a = b = 0.413 nm and c = 0.669 nm, which are in accordance with those of the JCPDS software [109]. The present research detected no other characteristic peaks of impurities, showing that the products are pure phase.

When the times were prolonged and the amount of HEC was greater (Figure 3.6 - 3.10), CdS (hcp) phase was also detected, as in the above characterization. Furthermore, the FWHM value of (002) peak of CdS prepared using 0.50 g HEC was smaller than other ones indicating the best orientation growth of the products prepared using 0.5g HEC.

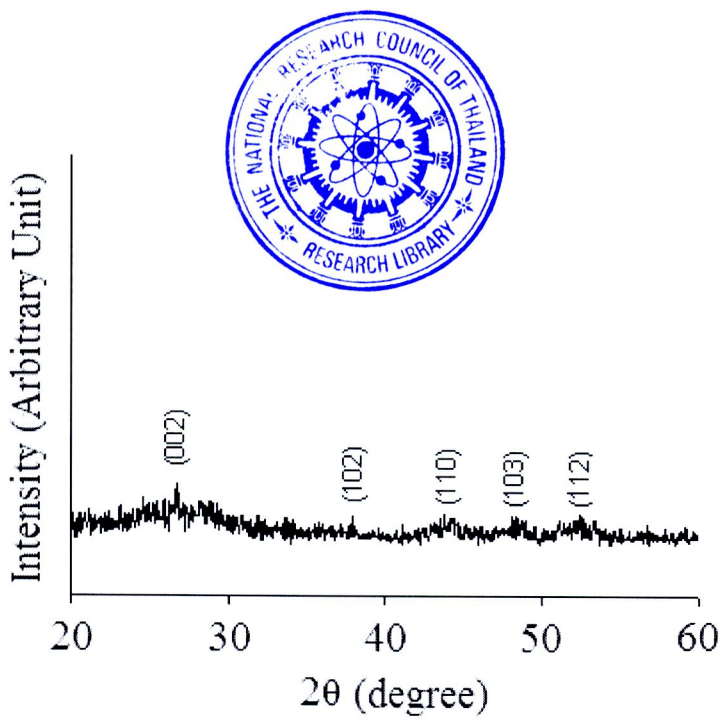

Figure 3.1 XRD pattern of the product synthesized using 0.25g HEC at 100 °C for 24 h

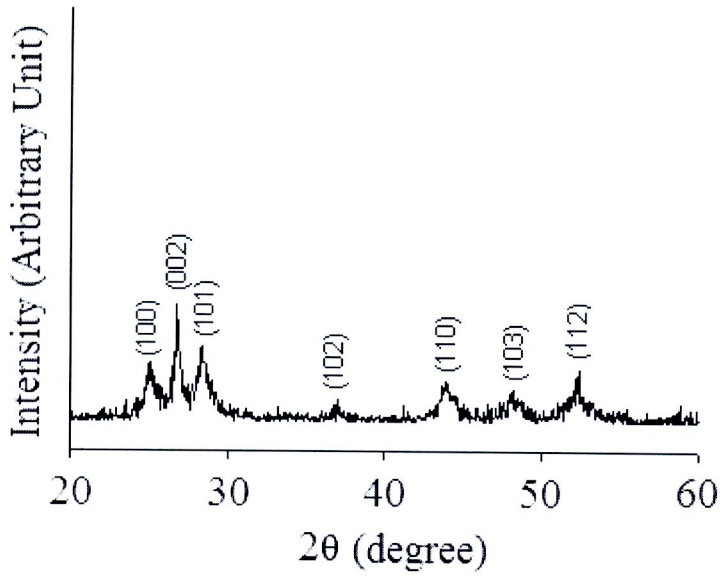

Figure 3.2 XRD pattern of the product synthesized using 0.25g HEC at 120 °C for 24 h

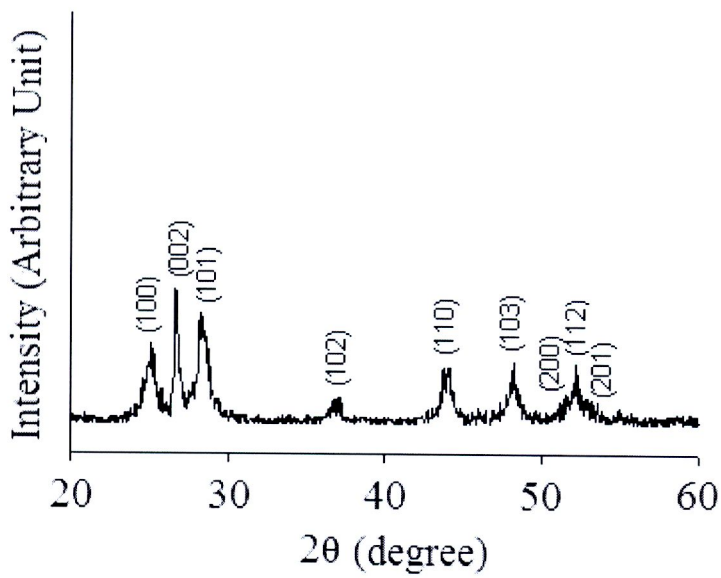

Figure 3.3 XRD pattern of the product synthesized using 0.25g HEC at 140 °C for 24 h

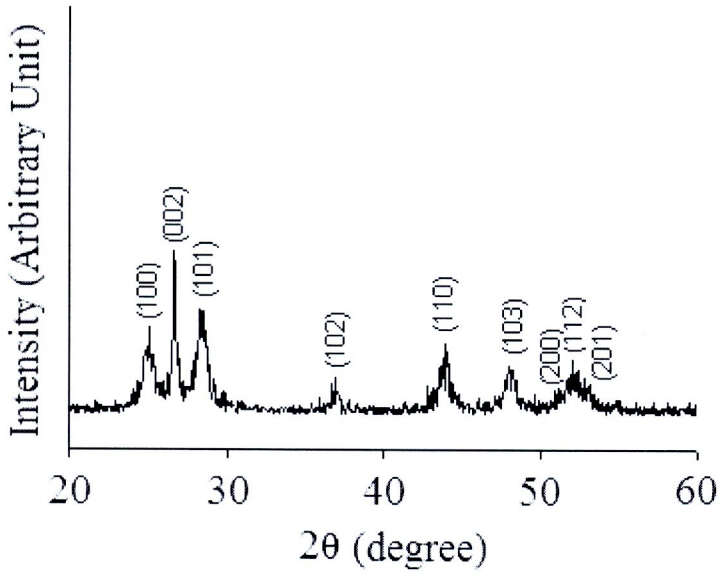

Figure 3.4 XRD pattern of the product synthesized using 0.25g HEC at 160 °C for 24 h

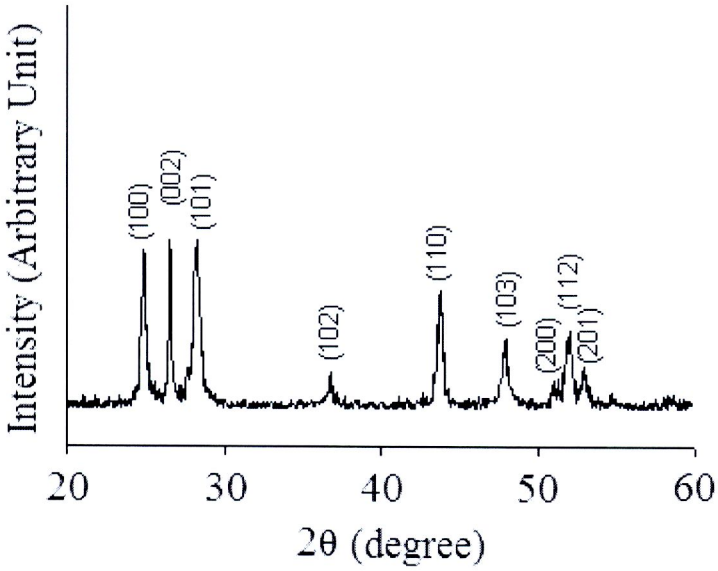

Figure 3.5 XRD pattern of the product synthesized using 0.25g HEC at 180 °C for 24 h

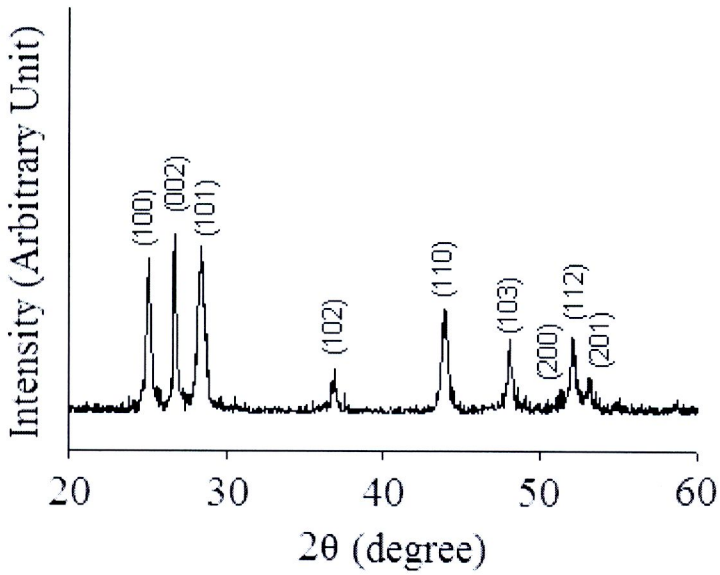

Figure 3.6 XRD pattern of the product synthesized using 0.25g HEC at 200 °C for 24 h

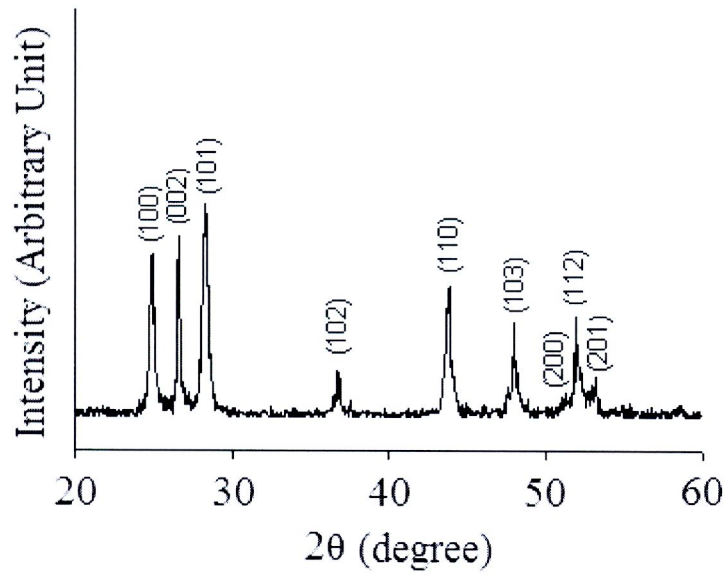

Figure 3.7 XRD pattern of the product synthesized using 0.25g HEC at 200 °C for 72 h

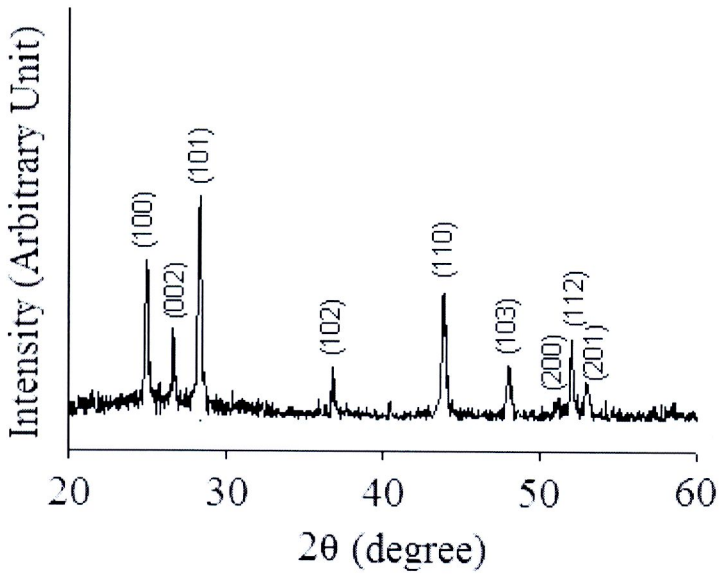

Figure 3.8 XRD pattern of the product synthesized using 0.50 g HEC at 200 ^{o}C for 72 h

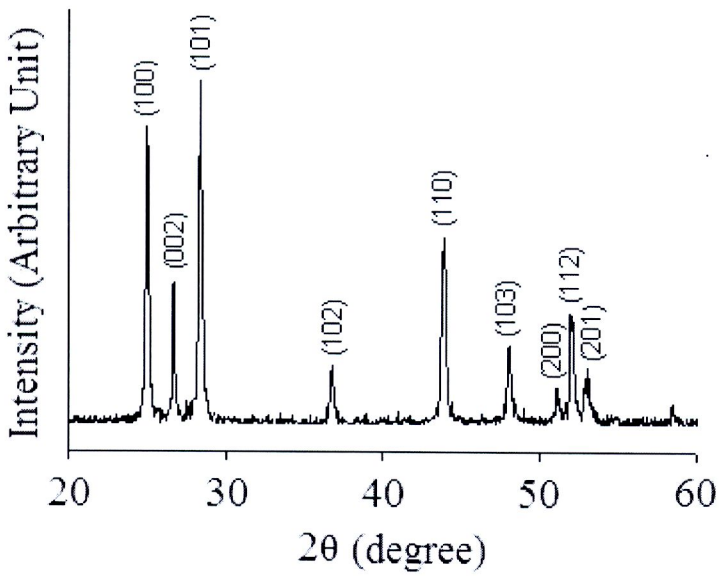

Figure 3.9 XRD pattern of the product synthesized using 0.75 g HEC at 200 ^{o}C for 72 h

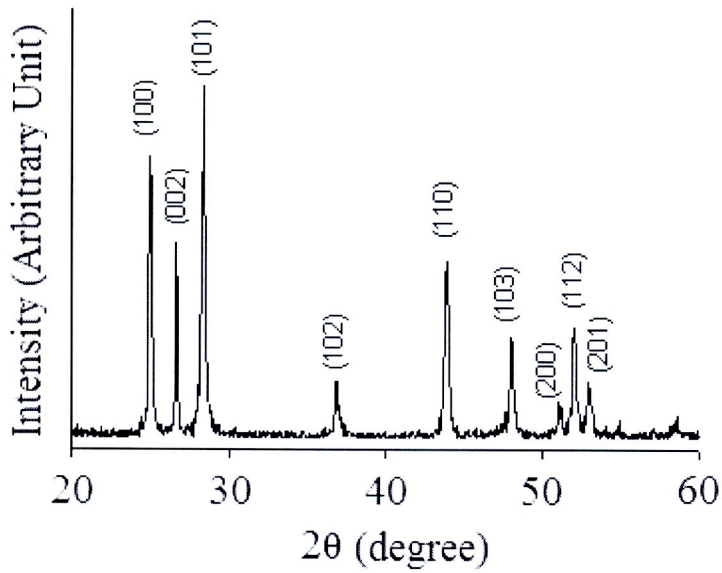

Figure 3.10 XRD pattern of the product synthesized using 1.00 g HEC at 200 °C for 72 h

3.1.2 Raman spectroscopy

The hexagonal wurtzite structured CdS nanorods belong to the point group C_{6v}. According to factor group analysis, the Raman active modes are $1A_1 + 1E_1 + 2E_2$, while $2B_2$ modes are silent. For A_1 branch the phonon polarization is in the *z* direction, whereas for the doubly degenerate E_1 and E_2 branches the phonon polarizations *xy* plane [112].

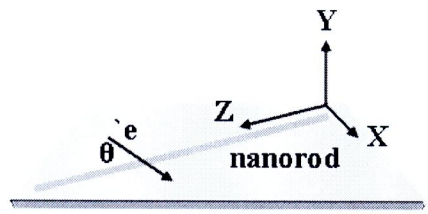

Figure 3.11 The Schematic setup of the Raman measurements which `e denotes incident light and the arrow denotes the polarization direction of light

Table 3.1 Raman vibration modes of CdS nanostructures

Vibration modes	Wavenumber (cm^{-1})			
	Experiment	Ref. [111]	Ref. [113]	Ref. [114]
1LO (Phonon vibration)	301	300	296	301
2LO (Phonon vibration)	599	600	598	604

Figure 3.12-3.21 shows Raman spectra of a CdS prepared using different reaction temperature and amount of HEC. The Raman spectra are very similar to each other although the products synthesized at different conditions. The two strong peaks at 301 and 599 cm^{-1} were attributed to the 1LO and 2LO of A_1 mode, respectively, which polarized in the *y-z* face (Figure 3.11) and strongly couple to the exciton along c axis [113-114]. Different Raman vibration modes of the present CdS nanorods and those of other reports are compared in Table 3.1. Intensity ratios of 2LO/ 1LO at temperatures of 100, 120, 140, 160, 180 and 200 °C are 0.30, 0.36, 0.42, 0.53, 0.74 and 0.89, respectively (as shown in Table 3.2 and Figure 3.23). They increase with the increasing of the solvothermal temperatures. Two peaks were also detected at the same wavenumbers although amount of HEC was increased. The 2LO/1LO ratios became 0.56, 1.01, 1.54, 1.48 and 1.35 for the use of 0.00, 0.25, 0.50, 0.75 and 1.00 g HEC in the process (as shown in Table 3.3 and Fig. 3.24). The ratio is the highest for 0.50 g HEC. Their relative intensities were strongly influenced by the anisotropic geometry of the products. As the length of CdS nanorod increases, the 2LO peaks became stronger in intensity. Because the strength of exciton – phonon coupling in semiconductors can be assessed by the intensity ratio of overtone of phonon to fundamental (I_{2LO} / I_{1LO}), the extraordinary large intensity ratio of the nanorods

reflects a strong exciton – LO phonon coupling in 1D semiconductor nanostructures [111].

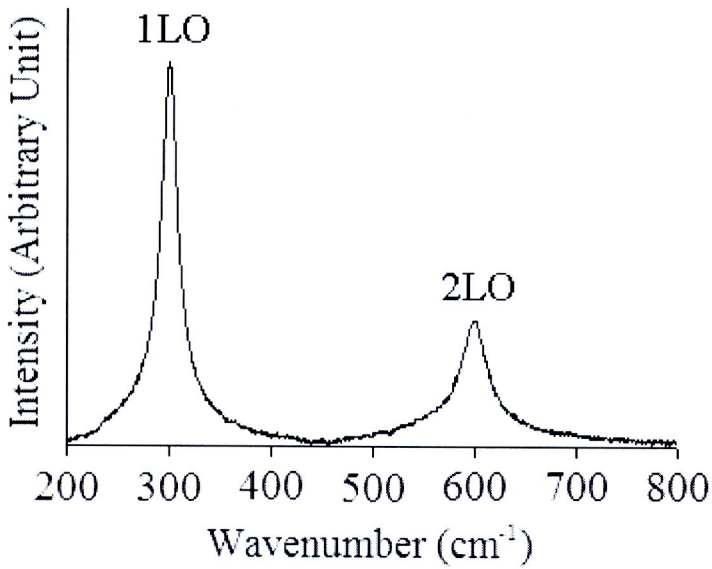

Figure 3.12 Raman pattern of the product synthesized using 0.25g HEC at 100 °C for 24 h

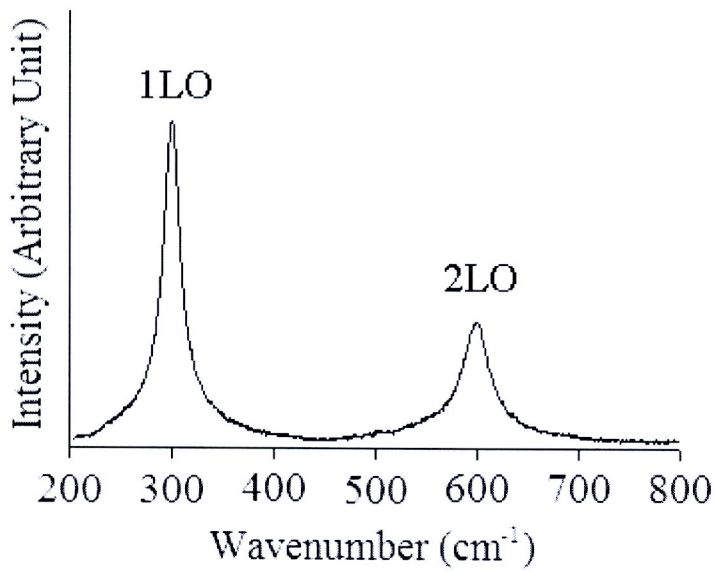

Figure 3.13 Raman pattern of the product synthesized using 0.25g HEC at 120 °C for 24 h

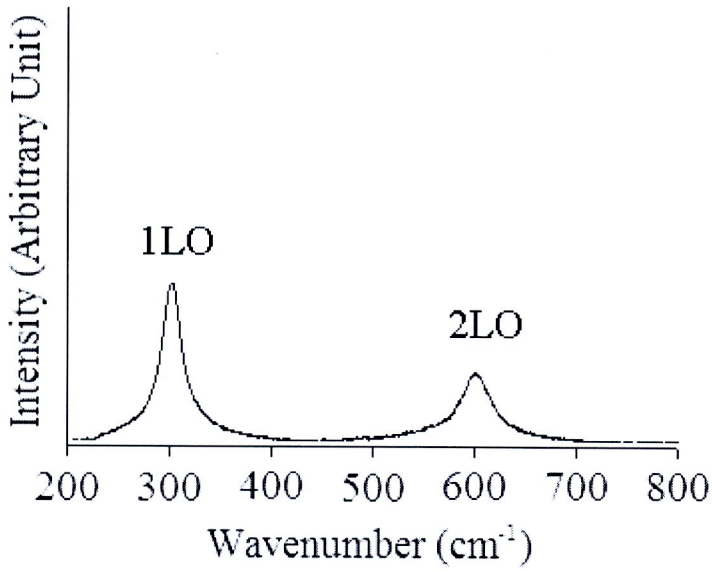

Figure 3.14 Raman pattern of the product synthesized using 0.25g HEC at 140 °C for 24 h

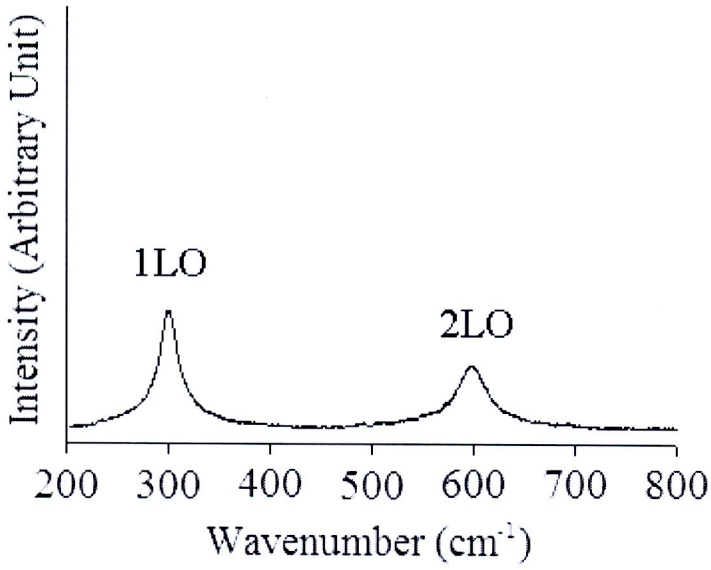

Figure 3.15 Raman pattern of the product synthesized using 0.25g HEC at 160 °C for 24 h

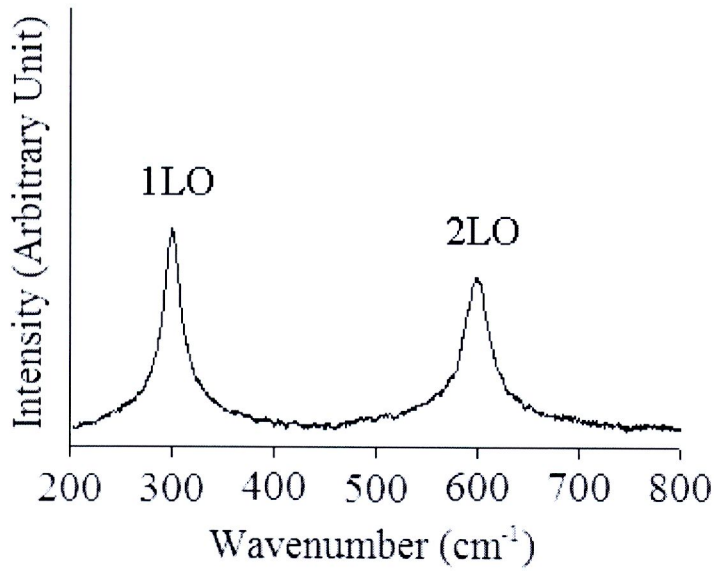

Figure 3.16 Raman pattern of the product synthesized using 0.25g HEC at 180 °C for 24 h

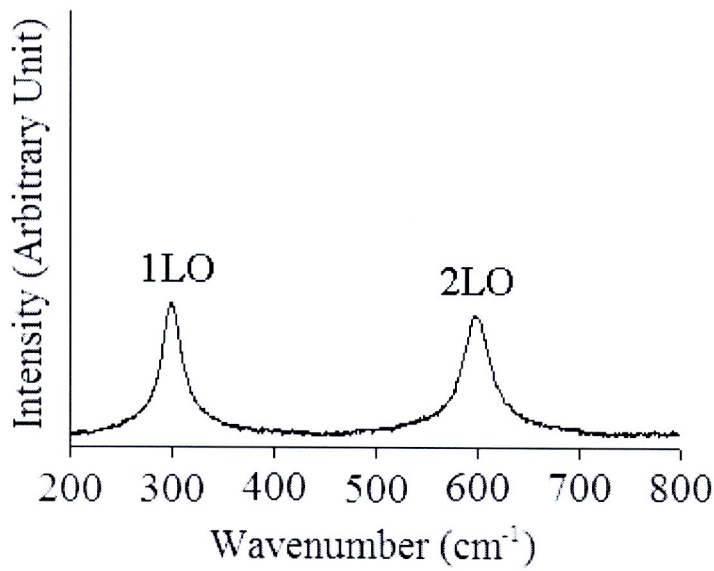

Figure 3.17 Raman pattern of the product synthesized using 0.25g HEC at 200 °C for 24 h

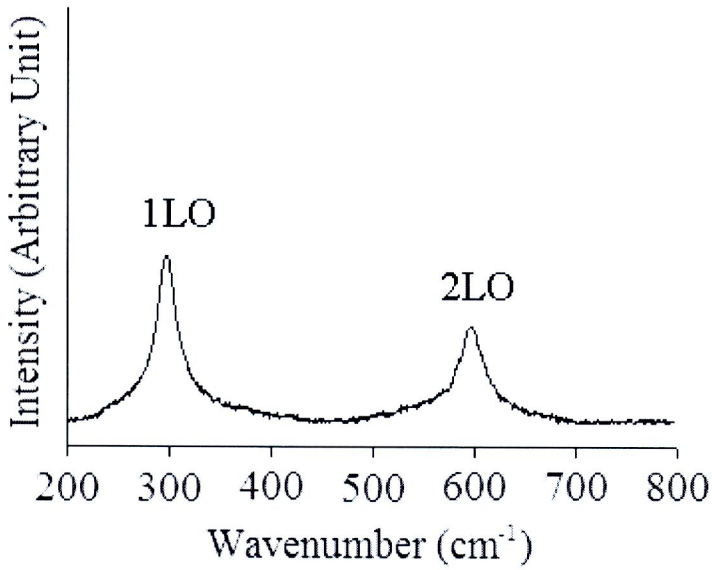

Figure 3.18 Raman pattern of the product synthesized using 0.00g HEC at 200 °C for 72 h

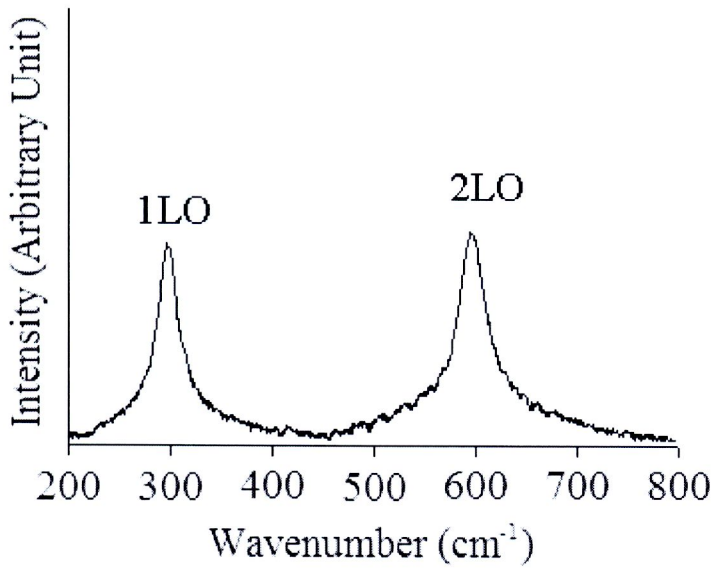

Figure 3.19 Raman pattern of the product synthesized using 0.25g HEC at 200 °C for 72 h

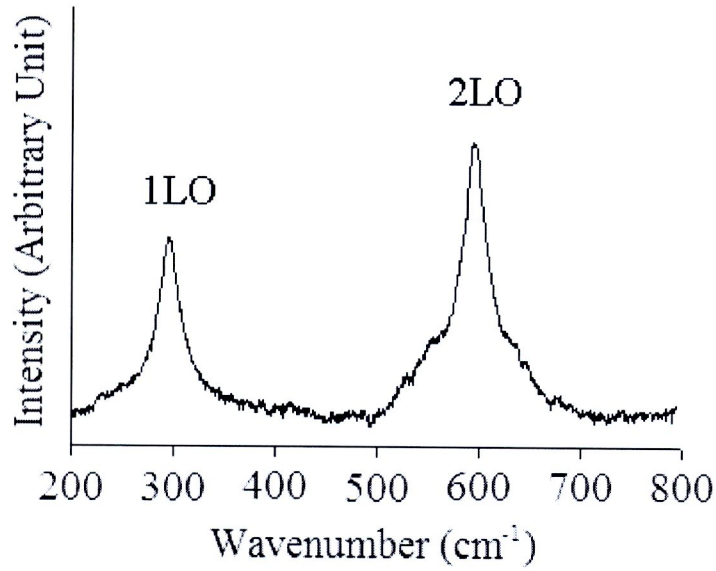

Figure 3.20 Raman pattern of the product synthesized using 0.50g HEC at 200 °C for 72 h

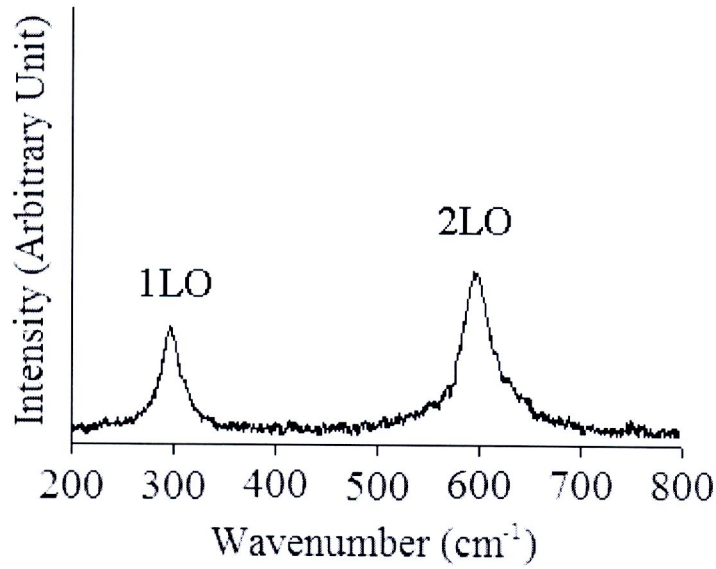

Figure 3.21 Raman pattern of the product synthesized using 0.75g HEC at 200 °C for 72 h

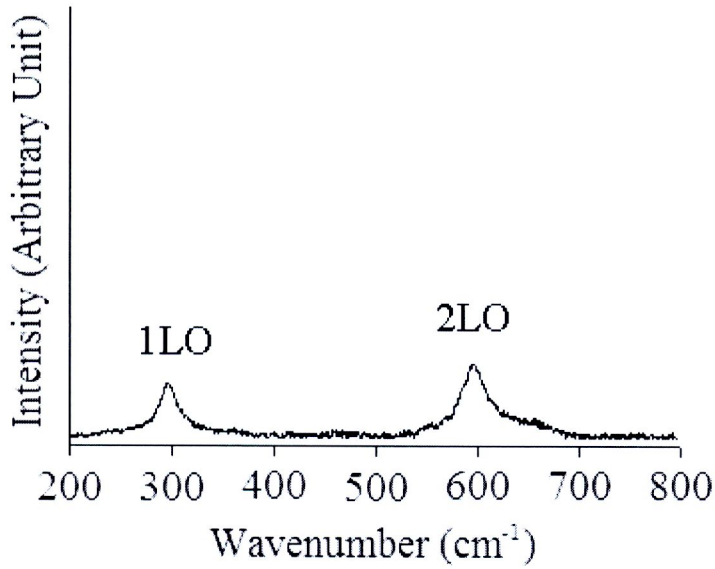

Figure 3.22 Raman pattern of the product synthesized using 1.00g HEC at 200 °C for 72 h

Table 3.2 Intensities ratio of 2LO to 1LO vibration modes of CdS samples prepared by using 0.25g of HEC at different temperature for 24 h

Condition (Temperature)	Intensities ratio 2LO/1LO
100 °C	0.30
120 °C	0.36
140 °C	0.42
160 °C	0.53
180 °C	0.74
200 °C	0.89

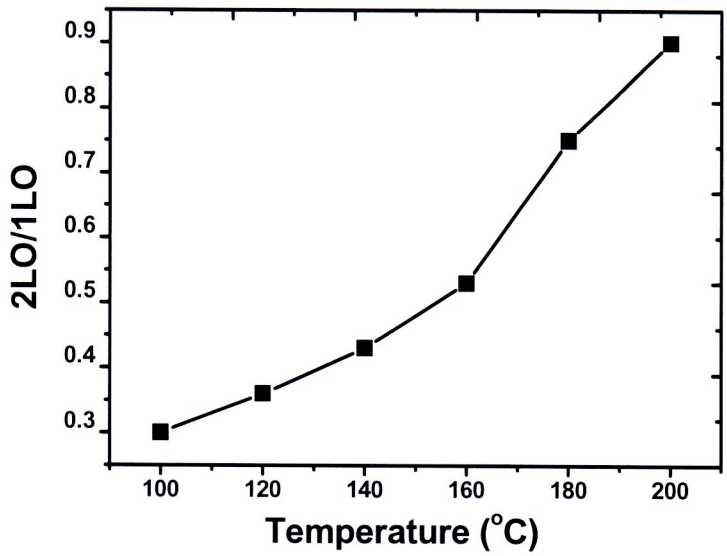

Figure 3.23 Vibration modes ratio (2LO/1LO) versus reaction temperature of CdS samples prepared by using 0.25g of HEC at different temperature for 24 h

Table 3.3 Intensities ratio of 2LO to 1LO vibration modes of CdS samples prepared by using the different amount of HEC at 200 °C for 72 h

Condition (HEC)	Intensities ratio LO2/LO1
0.00	0.56
0.25	1.01
0.50	1.54
0.75	1.48
1.00	1.35

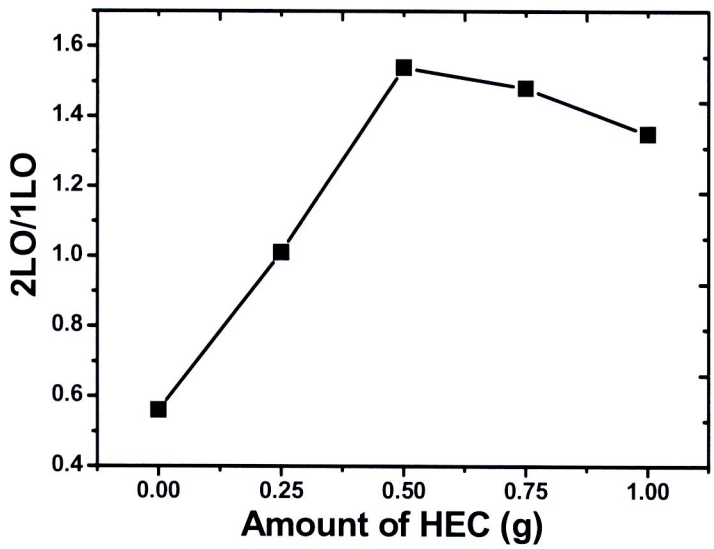

Figure 3.24 Vibration modes ratio (2LO/1LO) versus reaction temperature of CdS samples prepared by using the different amount of HEC at 200 °C for 72 h

3.1.3 Scanning electron microscopy (SEM)

The SEM images of the products synthesized using different conditions are shown in Figure 3.25-3.31. It was found that temperature and prolonged time affected on morphologies. At 100 °C, 24 h and 0.25 g HEC (Figure 3.25), the product was composed of a number of nanoparticles in clusters. When reaction temperature was increased to 200 °C (Figure 3.26), a number of nanorods with different orientations were detected. At 200 °C, 72 h and 0.25 g HEC (Figure 3.27), the nanorods were of greater length than the former product. From this result, we can conclude that the reaction temperature and period time affect slightly on the length of nanorods.

In order to investigate the effect of the HEC on the morphologies of as-prepared CdS samples, several samples were prepared under different amount of HEC. When the amount of HEC was increased, the nanorods became longer. They were the longest at 0.50 g HEC (Figure 3.28). Close examination of the product shows the elongated nanorods (Figure 3.29) to be perfect, with no defects detected. The nanorods became shorter using 0.75 and 1.00 g HEC (Figure 3.30 and 3.31). When less than 0.50 g of HEC was used, it was able to partially adsorb onto the nanorods and cause incomplete capping. But with excess HEC (more than 0.50 g), shorter nanorods were produced due to surplus capping. Thus, their axial growth was limited [115]. Some nanorods were in straight lines and some were bent, depending on the stress developed inside. For each condition, a number of different diameters and axial lengths of the nanorods were detected. This indicated that they nucleated at various times. Their growth rates were probably different as well.

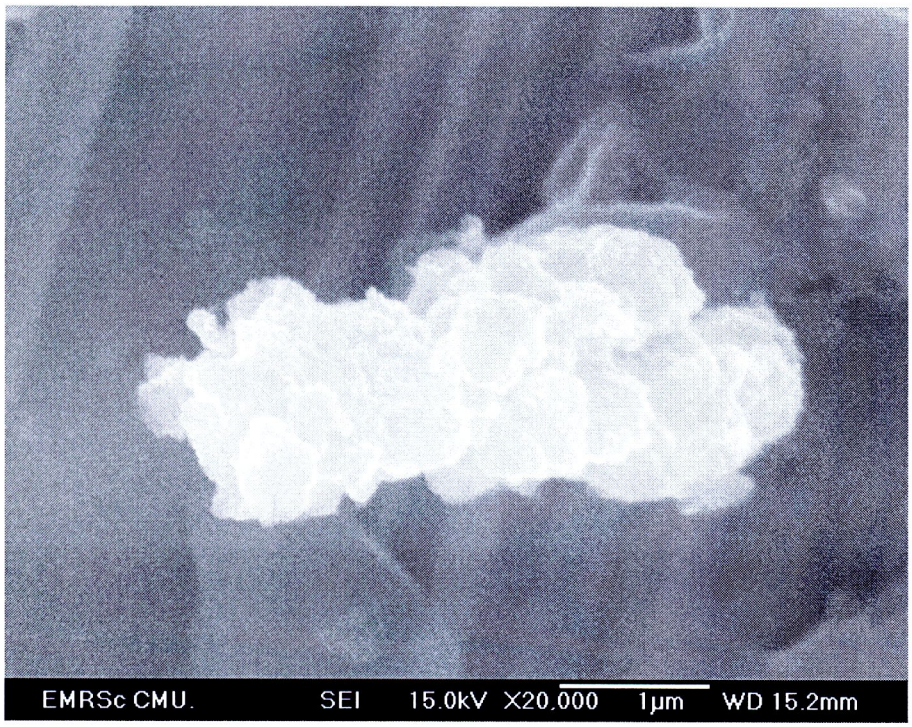

Figure 3.25 SEM image of the product synthesized using 0.25g HEC at 100 °C 24 h

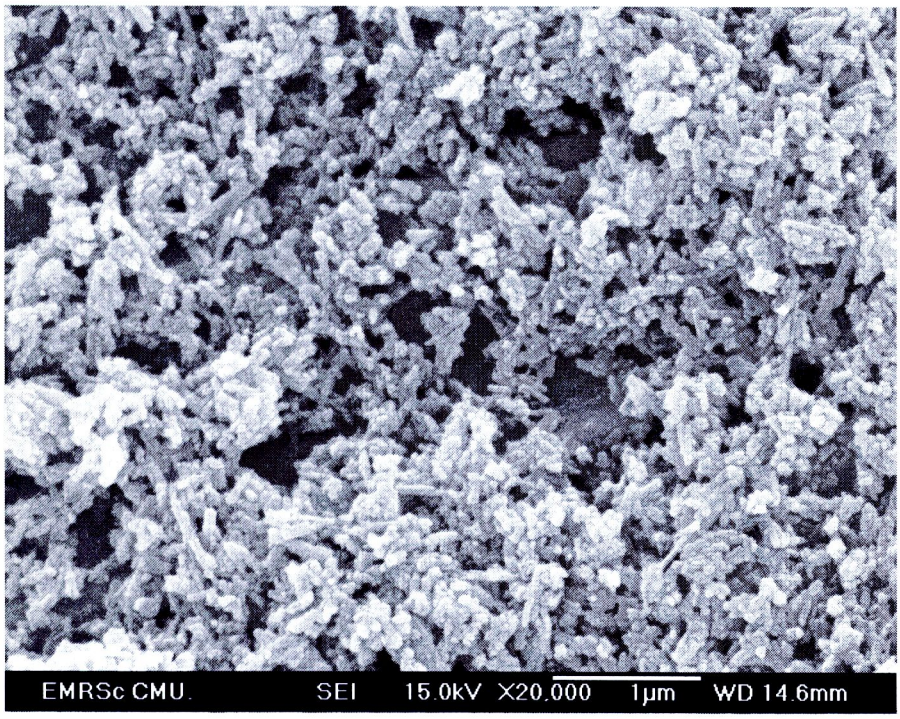

Figure 3.26 SEM image of the product synthesized using 0.25g HEC at 200 °C 24 h

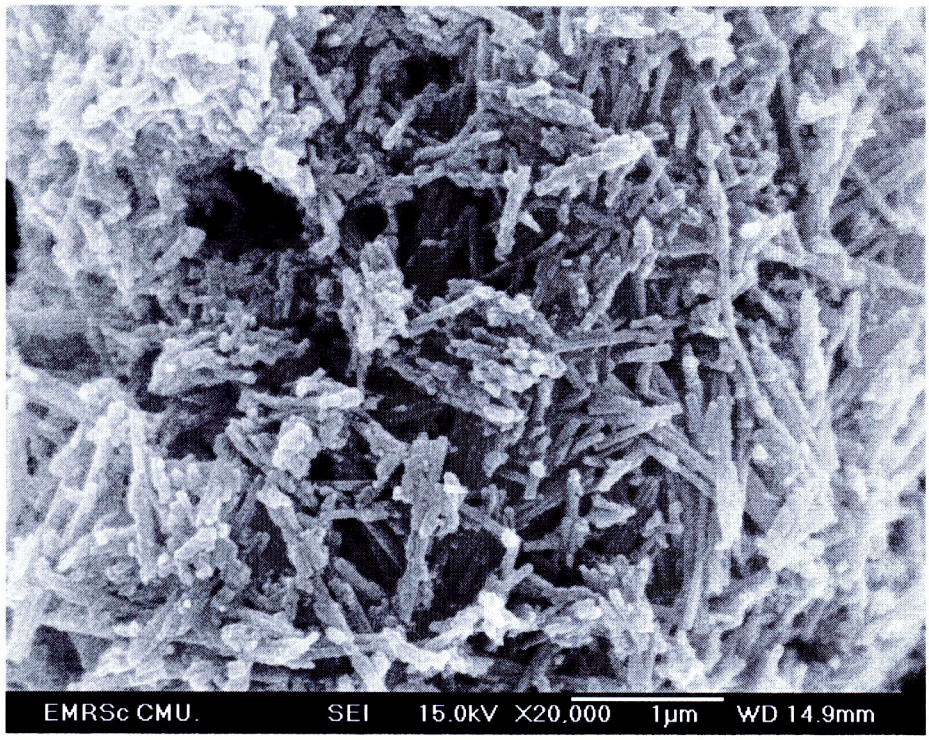

Figure 3.27 SEM image of the product synthesized using 0.25g HEC at 200 °C 72 h

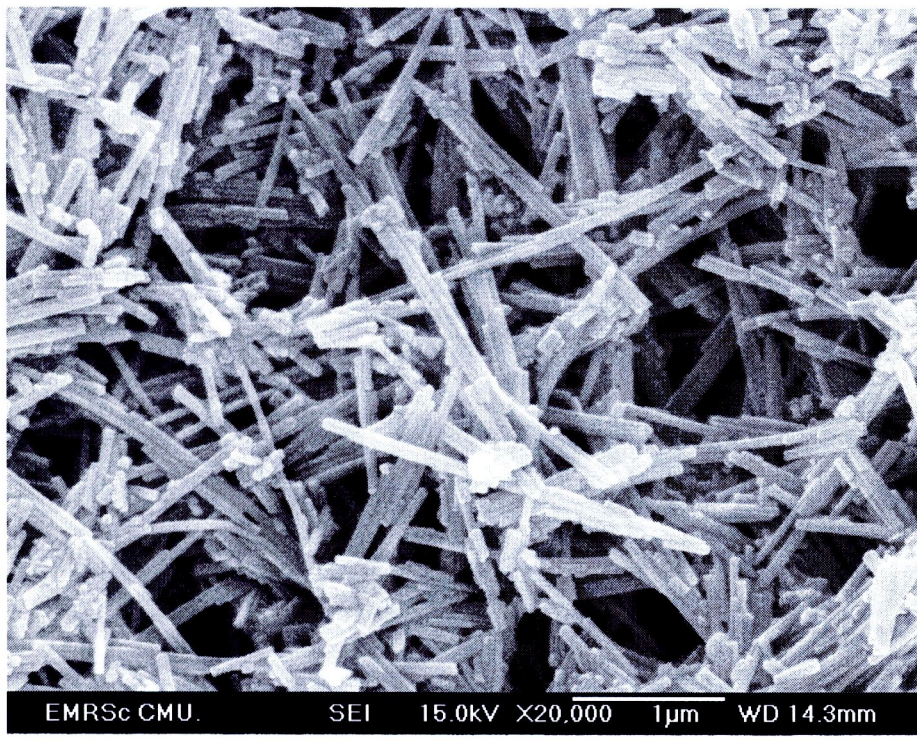

Figure 3.28 SEM image of the product synthesized using 0.50g HEC at 200 °C, 72 h

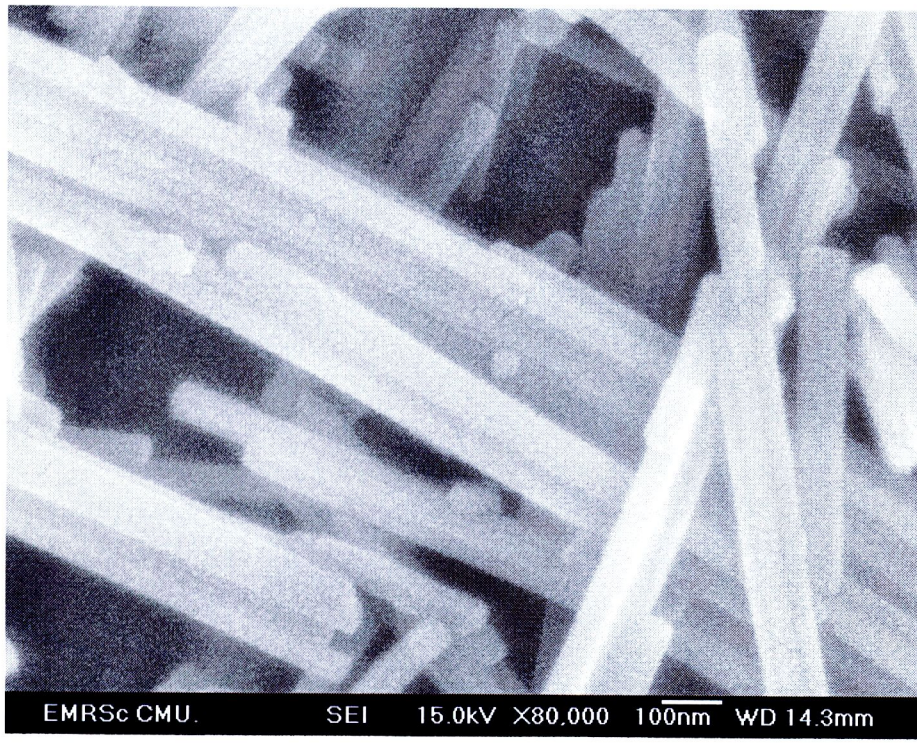

Figure 3.29 Magnified image of the product synthesized using 0.50g HEC at 200 °C, 72 h

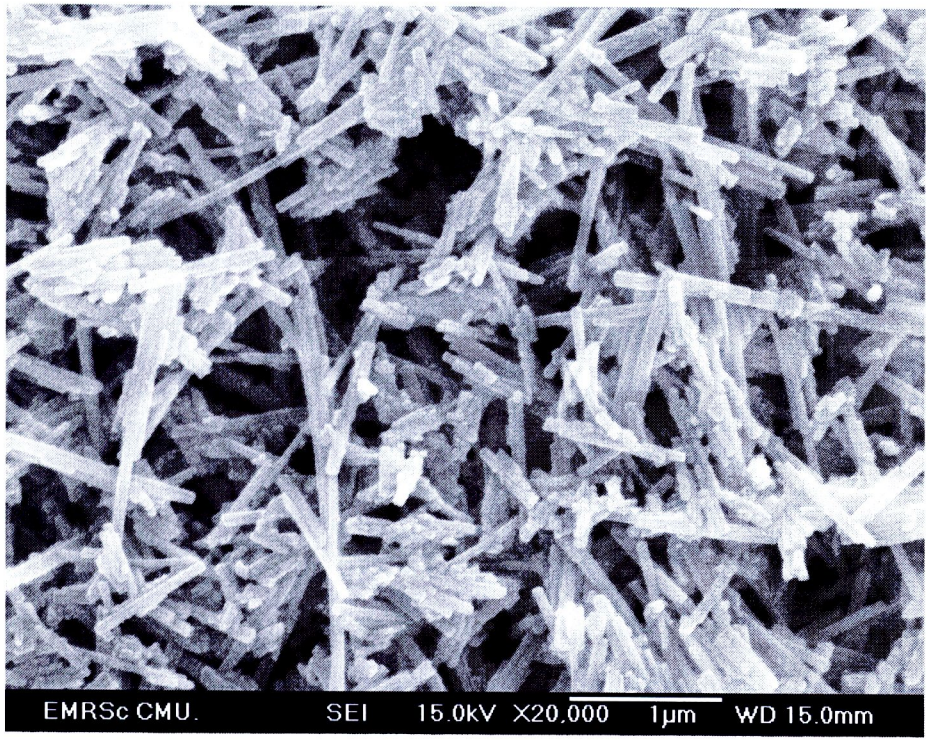

Figure 3.30 SEM image of the product synthesized using 0.75g HEC at 200 °C, 72 h

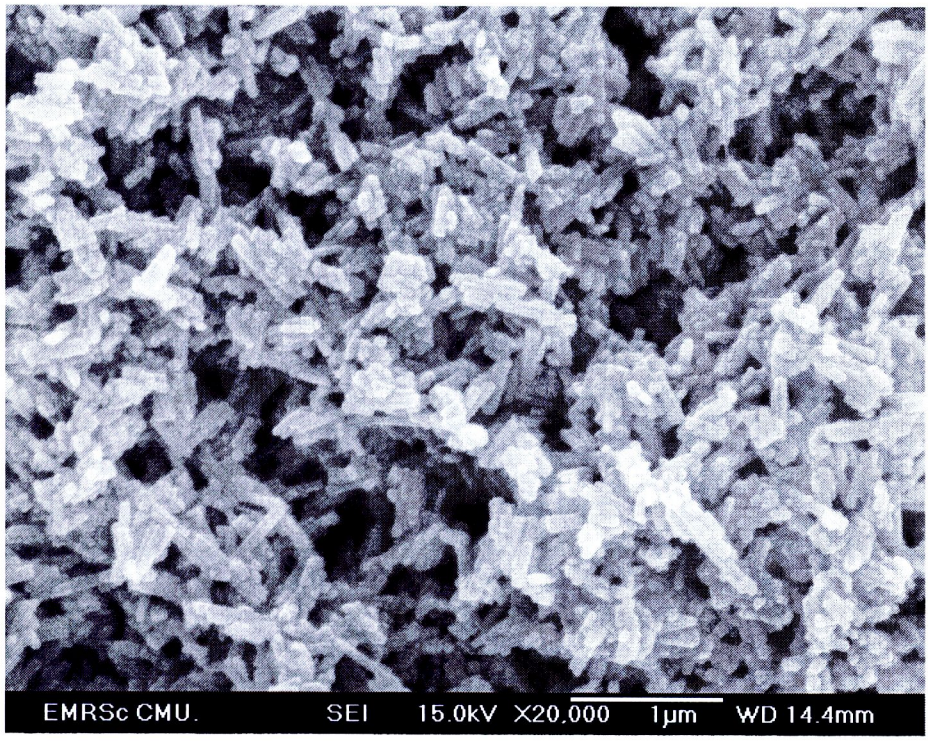

Figure 3.31 SEM image of the product synthesized using 1.00g HEC at 200 °C, 72 h

3.1.4 Transmission Electron Microscopy (TEM) and High Resolution Transmission Electron Microscopy (HRTEM)

TEM and HRTEM images (Figure 3.32-3.40) show the morphologies of the products synthesized using a variety of solvothermal temperatures, lengths of time, and amounts of HEC. For HEC-free system (Figure 3.32), the product was very fine nanoparticles in clusters although the temperature was as high as 200 °C and the time was as long as 72 h. At 100 °C, 24 h and 0.25 g HEC (Figure 3.33), the product was composed of a number of nanorods aligned in different directions; but the SEM image in Figure 3.25 shows the characteristics of nanoparticles in clusters. This disparity was caused by differences in magnification. The results show that HEC can play a role in templating the nanorods. When the temperature was increased to 200 °C (Figure 3.34) and the time prolonged to 72 h (Figure 3.35), the nanorods became

longer. To produce still longer nanorods, more HEC was required. Their lengths were increased to the longest value for 200 °C, 72 h and 0.50 g HEC (Figure 3.37), and decreased with the use of excess HEC (Figure 3.39). High magnification TEM images (Figure 3.36, 3,38, 3.40) show that the nanorods grew in the [001] direction although they were produced at different conditions. Close examination of the products revealed some defects contained in the nanorods as well. The HRTEM images show a number of the (002) planes aligning in systematic arrays. These show lattice atoms aligning in their crystal lattices. Their growth in the [001] direction is normal to the (002) planes. Each of them grew in the [001] direction. Growth direction of the nanorods is in accordance with the previous description of the XRD results.

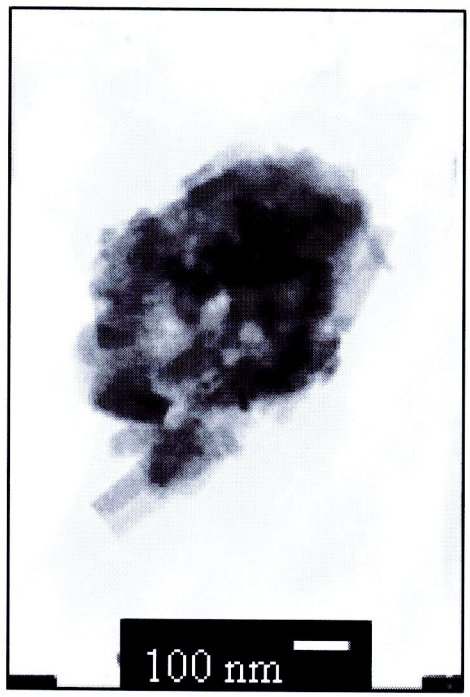

Figure 3.32 TEM image of the product synthesized using 200 °C, 72 h, 0.00g HEC

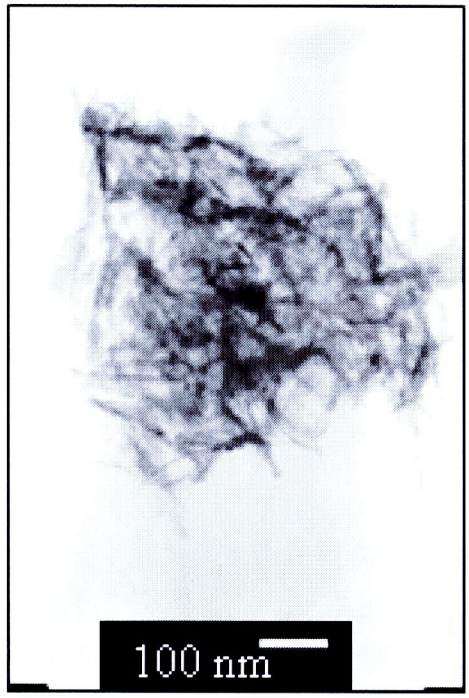

Figure 3.33 TEM image of the product synthesized using 100 °C, 24 h, 0.25g HEC

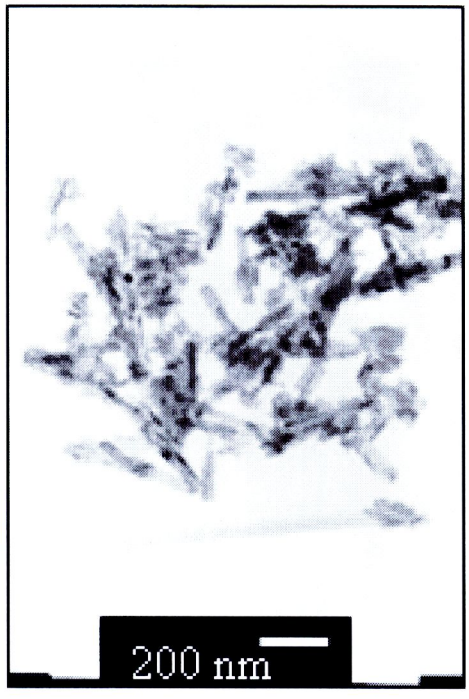

Figure 3.34 TEM image of the product synthesized using 200 °C, 24 h, 0.25g HEC

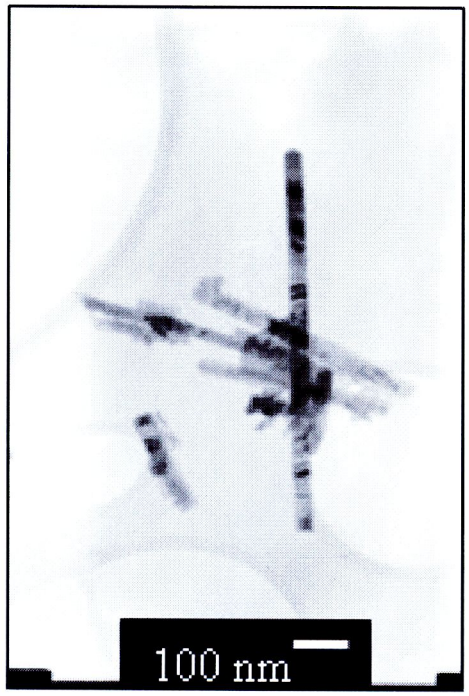

Figure 3.35 TEM image of the product synthesized using 200 °C, 72 h, 0.25g HEC

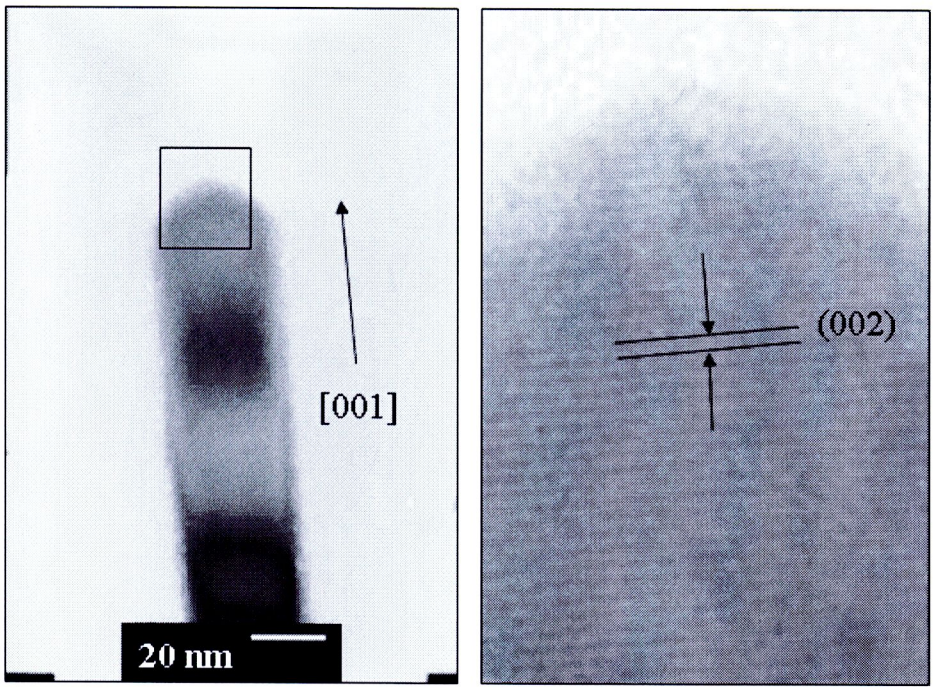

Figure 3.36 HRTEM image of the product synthesized using 200 °C, 72 h, 0.25g HEC

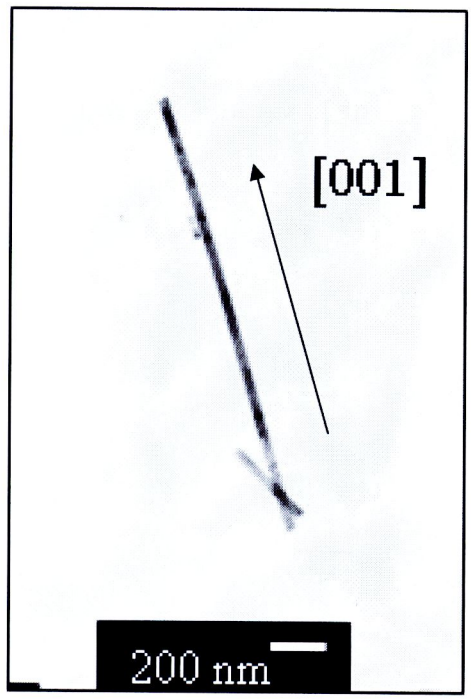

Figure 3.37 TEM image of the product synthesized using 200 °C, 72 h, 0.50g HEC

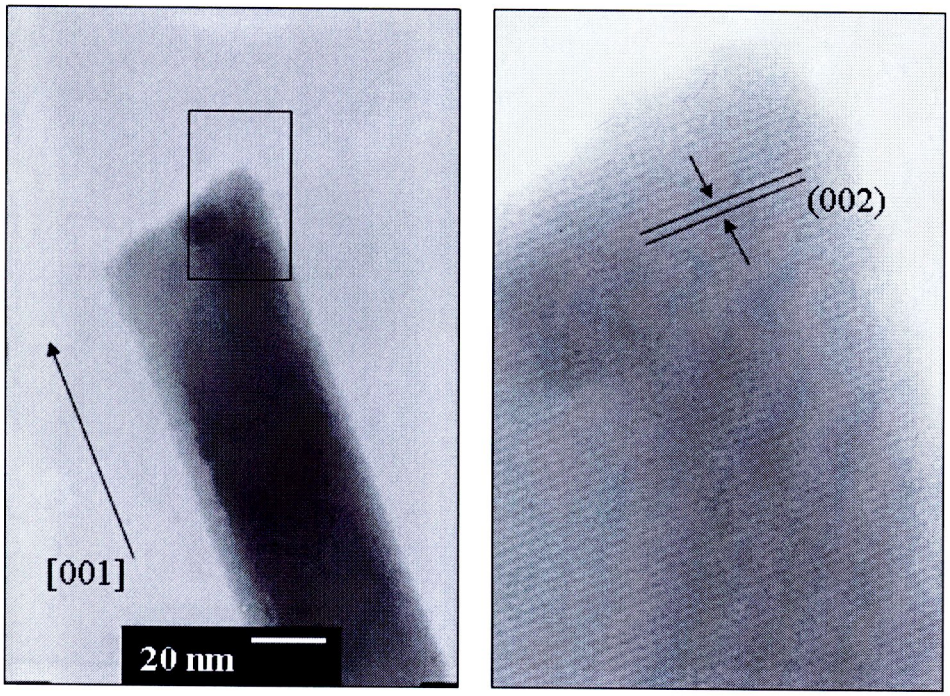

Figure 3.38 HRTEM image of the product synthesized using 200 °C, 72 h, 0.50g HEC

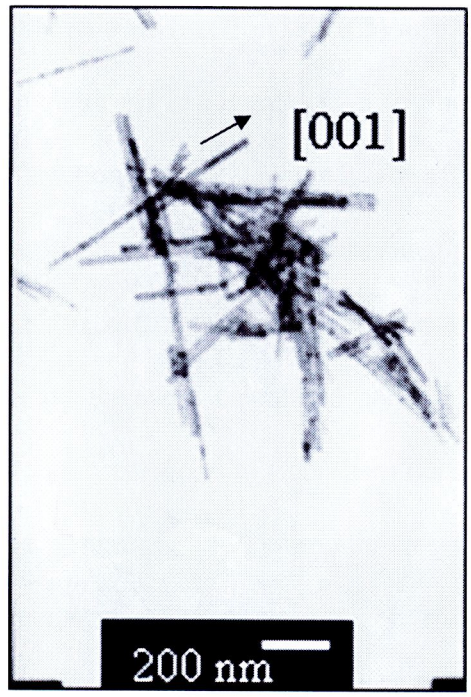

Figure 3.39 TEM image of the product synthesized using 200 °C, 72 h, 0.75g HEC

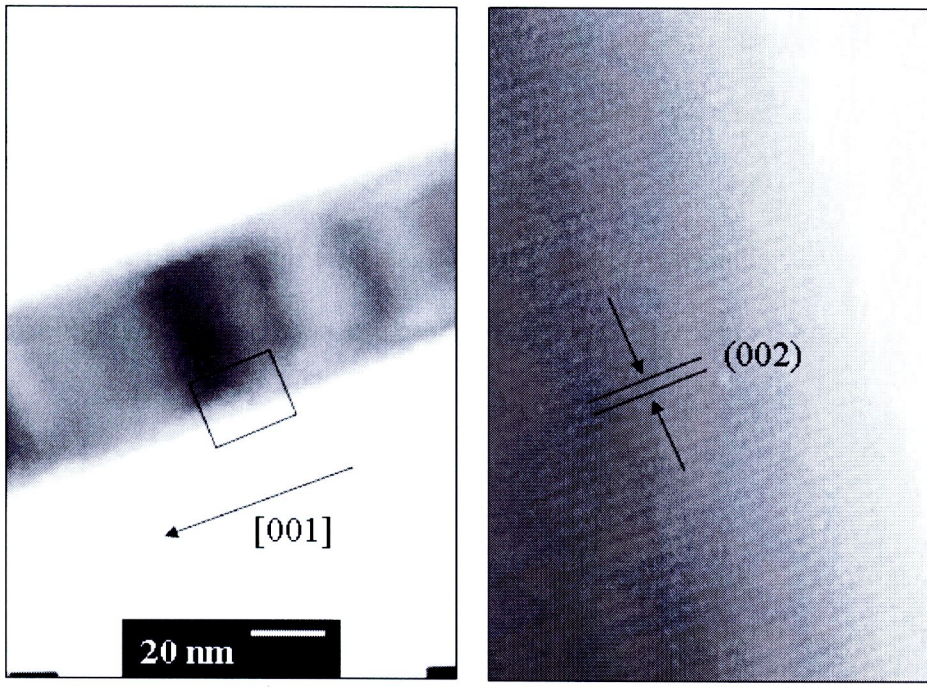

Figure 3.40 HRTEM image of the product synthesized using 200 °C, 72 h, 0.75g HEC

3.1.5 Selected area electron diffraction (SAED) and simulated patterns

SAED patterns of the nanorods in Figure 3.41-3.43 show bright concentric rings corresponding to their diffraction planes. The rings are diffuse and hollow showing that the products were composed of a number of nanosized particles. Diameters of the rings were measured from the diffraction patterns on the films. The calculated d-spacing of the diffraction planes were calculated and compared with those of the JCPDS software. The patterns correspond to CdS (hcp). Other SAED patterns (Figure 3.44, 3.46, 3.48) appear as symmetric and systematic arrays of bright spots, showing that a number of atoms were arranged in crystal lattices. The patterns were interpreted [94] and specified as CdS (hcp). Calculated electron beams are in the same direction of [-110], the direction that the electron beams were sent to the crystal facets. Diffraction patterns with a [-110] zone axis were simulated (Figure 3.45, 3.47, 3.49) [24]. The simulated spots in the specified crystallographic planes are in systematic and symmetric arrays. The interpreted and simulated patterns are thus in good accordance. The a*, b* and c* lattice vectors are in the [100], [010] and [001] directions, respectively. For the crystal structure, the corresponding lattice vectors are the same although the products were produced under different conditions.

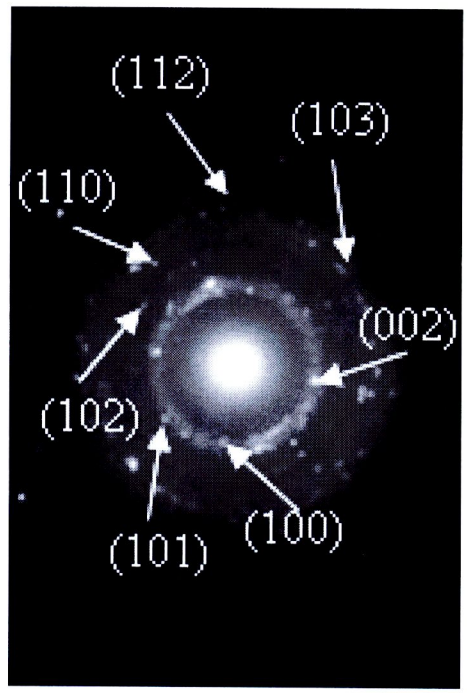

Figure 3.41 SAED pattern of the product synthesized using 200 °C, 72h, 0.00g HEC

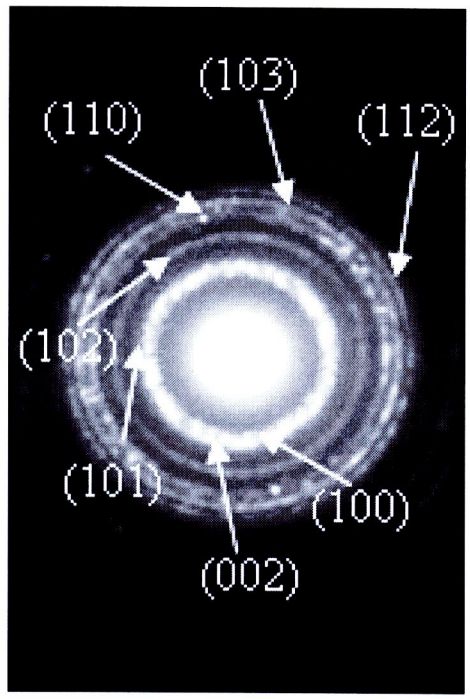

Figure 3.42 SAED pattern of the product synthesized using 100 °C, 24 h, 0.25g HEC

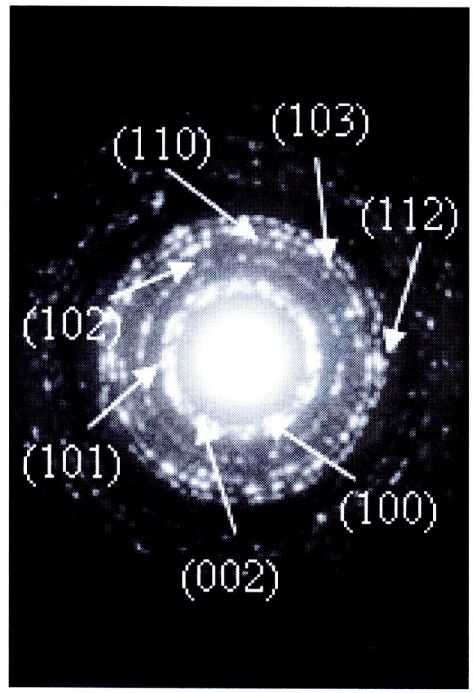

Figure 3.43 SAED pattern of the product synthesized using 200 °C, 24 h, 0.25g HEC

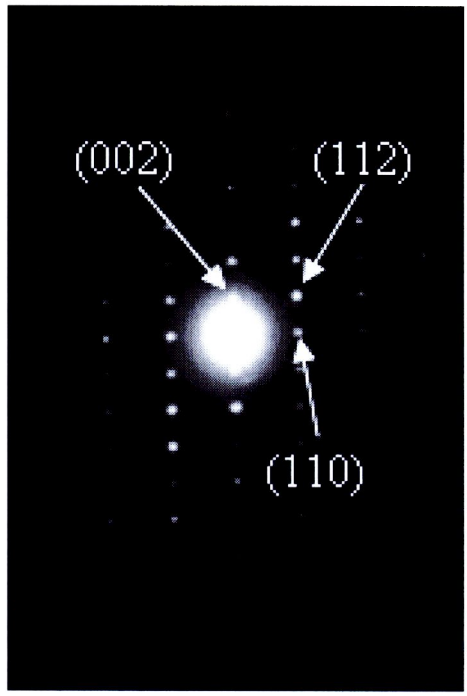

Figure 3.44 SAED pattern of the product synthesized using 200 °C, 72 h, 0.25 g HEC

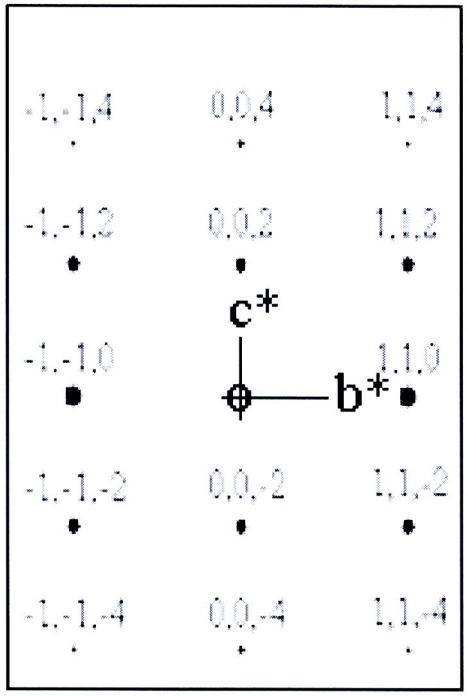

Figure 3.45 Simulated pattern of the product synthesized using 200 °C, 72 h, 0.25 g HEC

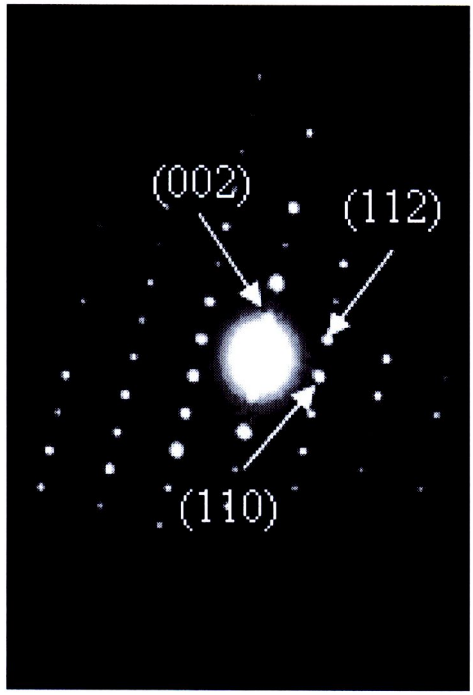

Figure 3.46 SAED pattern of the product synthesized using 200 °C, 72 h, 0.50 g HEC

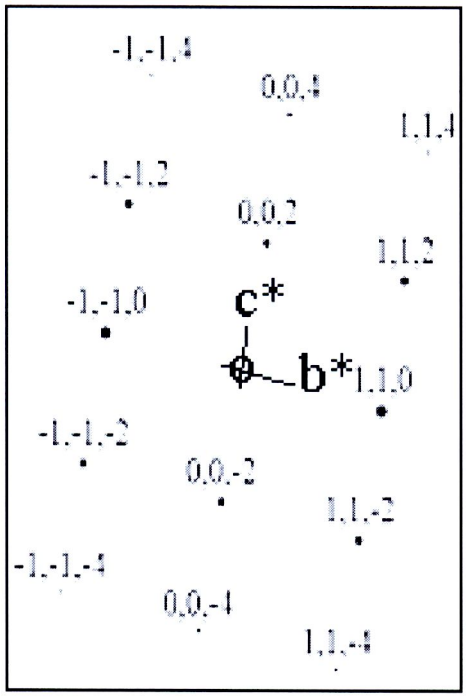

Figure 3.47 Simulated pattern of the product synthesized using 200 °C, 72 h, 0.50 g HEC

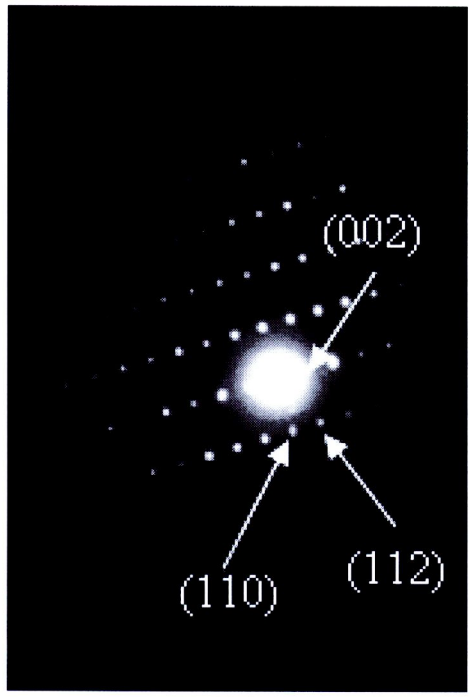

Figure 3.48 SAED pattern of the product synthesized using 200 °C, 72 h, 0.75 g HEC

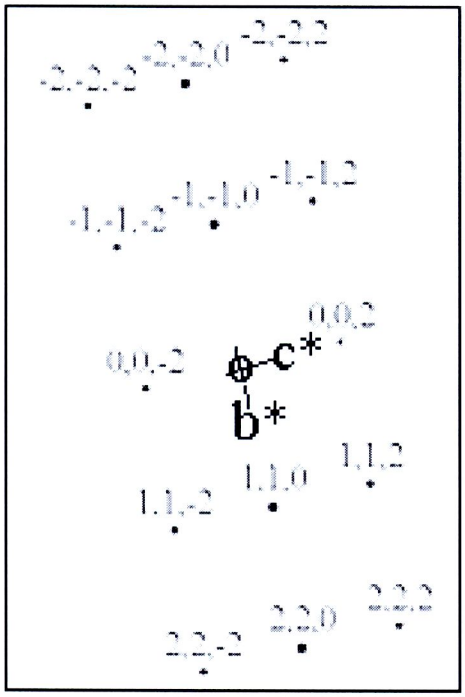

Figure 3.49 Simulated pattern of the product synthesized using 200 °C, 72 h, 0.75 g HEC

3.1.6 Proposed mechanism

For the present research, the formation of CdS nanorods is proposed as follows,

$$Cd(CH_3COO)_2 + 2en \longrightarrow [Cd(en)_2]^{2+} \quad \text{---------- (1)}$$

$$\left.\begin{aligned} S_n + 2NH_2CH_2CH_2NH_2 &\longrightarrow [NH_2CH_2CH_2NH\text{-}S_{n-1}\text{-}2NHCH_2CH_2NH_2] + H_2S \\ H_2S &\longrightarrow 2H^+ + S^{2-} \end{aligned}\right\} \text{---(2)}$$

$$[Cd(en)_2]^{2+} + S^{2-} \longrightarrow CdS \quad \text{---------- (3)}$$

$Cd(CH_3COO)_2$ – HEC gel reacted with ethylenediamine (en), a strongly bidentate ligand, to form $[Cd(en)_2]^{2+}$ complex ions (Equation. 1). At the same time, S powder was reduced by ethylenediamine to form S^{2-} ions (Equation. 2). $[Cd(en)_2]^{2+}$ and S^{2-} ions were mixed and further reacted in home-made stainless steel autoclaves at different temperatures, lengths of time, and amounts of HEC. Finally, CdS (hcp) was produced (Equation. 1). The CdS nuclei that formed were not fully developed (nascent). Initially, HEC adsorbed onto the side walls of the nuclei, which caused termination of lateral growth. Their tips were uncovered, axial growth proceeded very rapidly. As seen from TEM and HRTEM, growth in the x and y directions was limited. The nuclei grew in the z or [001] direction via the diffusion process. Hence, CdS nanorods were produced. These CdS nanorods grew in the same direction as those prepared by other researchers [115]. To form the longest nanorods, the appropriate amount of HEC was used. The details are explained in the above section. The present research shows that HEC played an important role in one dimensional growth of CdS nanorods in the stainless steel autoclaves. HEC concentrations have a strong influence in templating and limiting the axial lengths of the nanorods.

3.1.7 Photoluminescent Spectroscopy (PL)

Photoluminescent (PL) spectra (Figure 3.50) were analyzed using 210 nm excitation wavelength (λ_{ex}). Two distinct emissions were detected at approximately 470 and 575 nm, which are very close to results previously reported [116]. Some energy was lost during the characterization, and the emission of longer wavelengths than λ_{ex} was detected. The first peak was caused by the electron-hole recombination, and the second by surface trapping induced emission [116]. The use of 0.50 g HEC resulted in the strongest intensity of the recombination band. The intensity of the surface trapping induced emission band was between those of the 1.00 g HEC and the HEC-free system. The lesser intensity of the HEC-free product was caused by non-capping. But for excess HEC, the stronger surface emission was caused by surplus capping. The present results thus show that HEC dosages have an influence on the PL emissions of the products. The use of 0.50 g HEC was the appropriate amount to produce the longest nanorods with the strongest recombination intensity. Compared to the 515 nm wavelength of bulk CdS (hcp) [116], the 470 nm wavelength of the current nanorods is blue-shifted due to the quantum size effect [117-118]. The extent of blue-shift increased with a decrease in particle sizes or an increase in the surface-to-volume ratios.

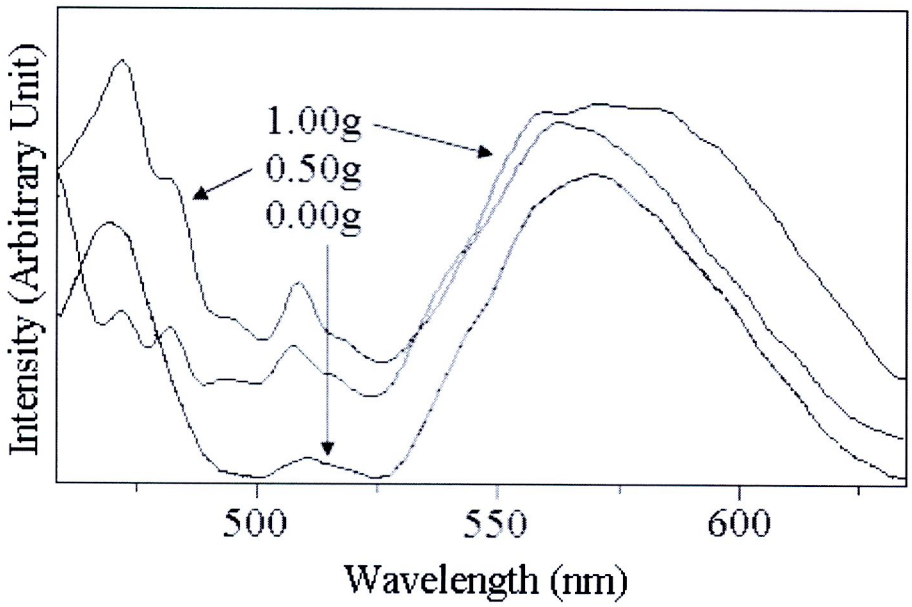

Figure 3.50 PL spectra of CdS powders synthesized using the different amount of HEC at 200 °C for 72 h

Table 3.4 λ_{max} of emission and surface emission peaks of CdS powders prepared by using the different amount of HEC at 200 °C for 72 h

Conditions (HEC)	Emission peak (electron-hole recombination)	Surface emission (surface trap induced emission)
0.00g	470	575
0.50g	470	575
1.00g	470	575

3.2 Bi_2S_3 synthesized by a polymer-assisted hydrothermal method

3.2.1 X-ray diffraction (XRD)

XRD spectra of Bi_2S_3 produced by a hydrothermal method under different conditions are shown in Figure 3.51-3.56. All XRD spectra were indexed and interpreted as orthorhombic Bi_2S_3 of the JCPDS No. 17-0320 [109]. The products are pure phase without detection of any impurities, such as Bi_2O_3 and Bi. In polymer-free solutions at 100 °C for 2 h (Figure 3.51), XRD peaks are rather broad, specifying that lattice atoms were in a state of disorder to some degrees. When only the temperature was increased to 200 °C (Figure 3.52), or both the temperature and time were increased to 200 °C and 20 h (Figure 3.53), the spectra became narrower and sharper. These were also true for the products produced in polymer-added solutions. Lattice atoms became in a state of more complete order, and the products have higher degree of crystallinity.

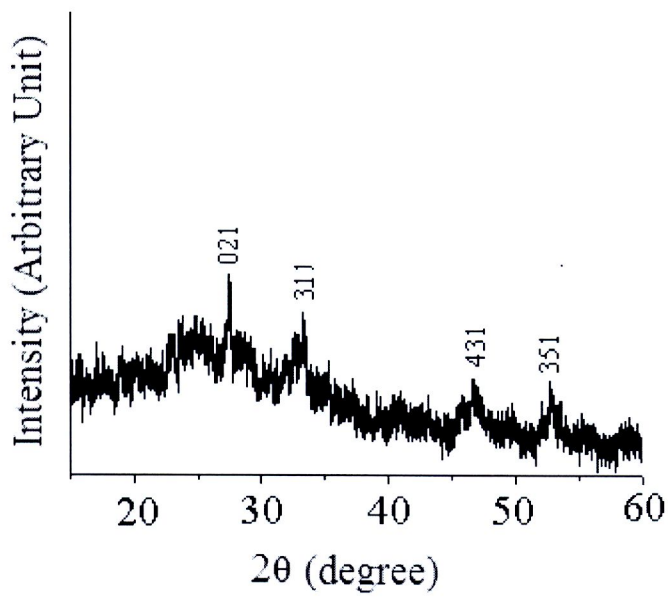

Figure 3.51 XRD pattern of Bi_2S_3 hydrothermally produced in polymer-free solution at 100 °C, 2 h

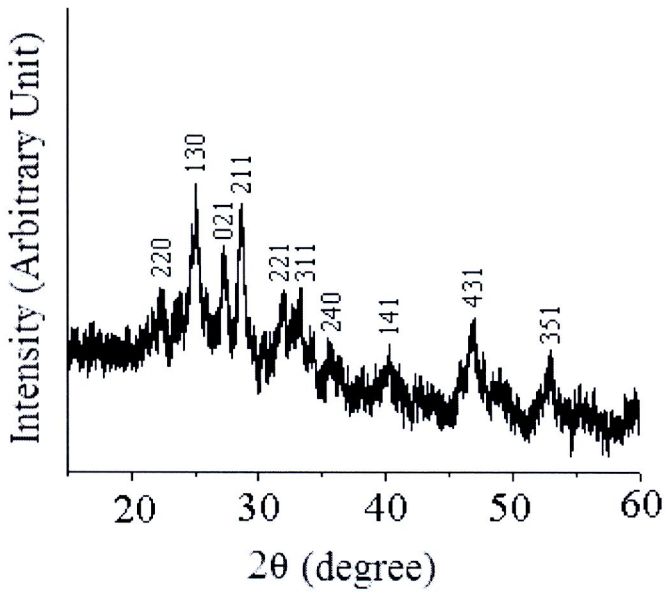

Figure 3.52 XRD pattern of Bi_2S_3 hydrothermally produced in polymer-free solution at 200 °C, 2 h

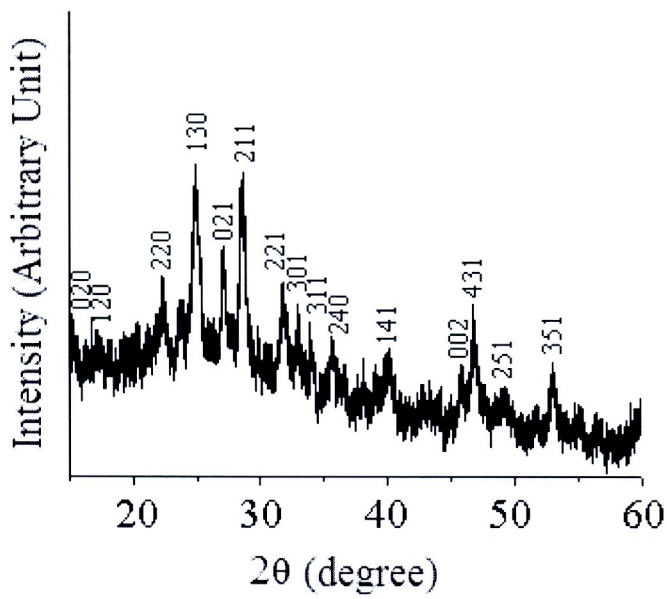

Figure 3.53 XRD pattern of Bi_2S_3 hydrothermally produced in polymer-free solution at 200 °C, 20 h

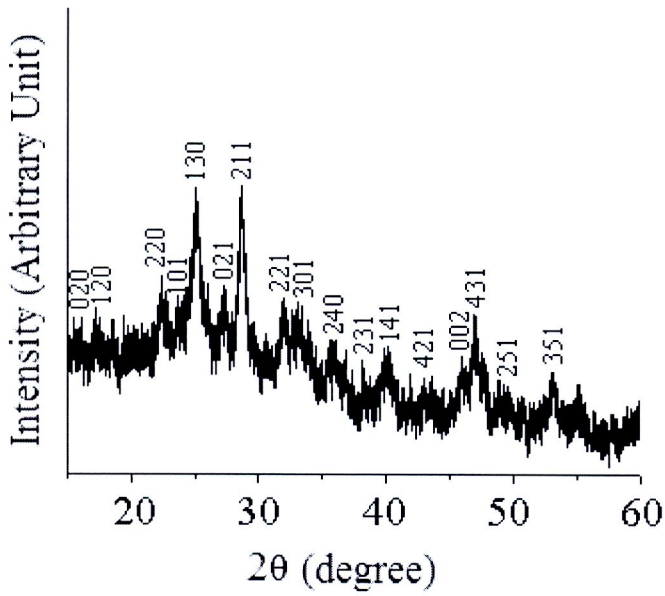

Figure 3.54 XRD pattern of Bi_2S_3 hydrothermally produced by using 1 g PVA at 200 ^{o}C, 20 h

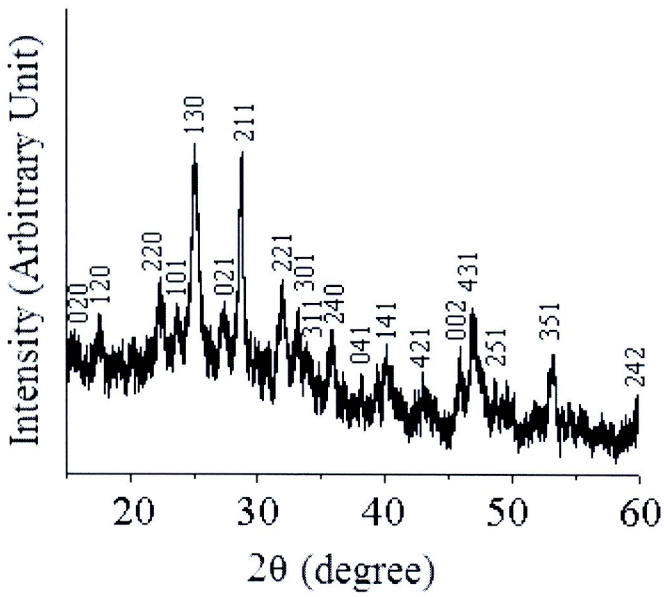

Figure 3.55 XRD pattern of Bi_2S_3 hydrothermally produced by using 1 g PEG at 200 ^{o}C, 20 h

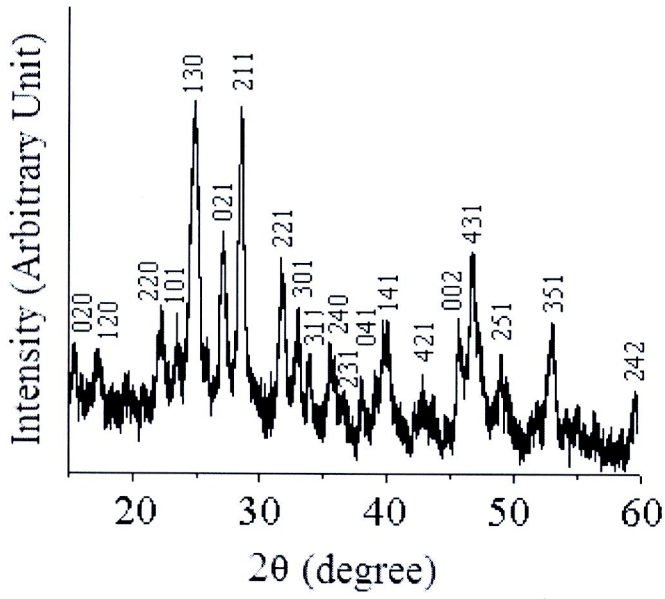

Figure 3.56 XRD pattern of Bi_2S_3 hydrothermally produced by using 1 g PVP at 200 °C, 20 h

3.2.2 Raman Spectroscopy

A definite existence of Bi_2S_3 was analyzed using a Raman spectrometer. Raman spectra of the produces produced in polymer-free solution and solution containing one gram of PVA, PVP, and PEG at 200 °C for 20 h, are shown in Figure 3.57, 3.58, 3.59 and 3.60, respectively. All spectra show four vibration modes at 139.6, 253.7, 310.0 and 968.9 cm^{-1}. The first mode is in accordance with the surface phonon vibration of the nanorod [119]. The last three ones correspond to vibration mode of Bi-S bonds [119-121]. Different Raman vibration modes of the present Bi_2S_3 and those of other reports are compared in Table 3.5. These detections strongly support the above XRD analysis, which specified that the products are orthorhombic Bi_2S_3 with Pbnm space group.

Table 3.5 Raman vibration modes of Bi_2S_3 nanostructures

Vibration modes	Wavenumber (cm^{-1})				
	Experiment	Ref. [119]	Ref. [120]	Ref. [121]	Ref. [122]
Phonon vibration	139.6	139.4	-	-	-
Bi-S vibration	252, 310, 968.9	252	253	250	250

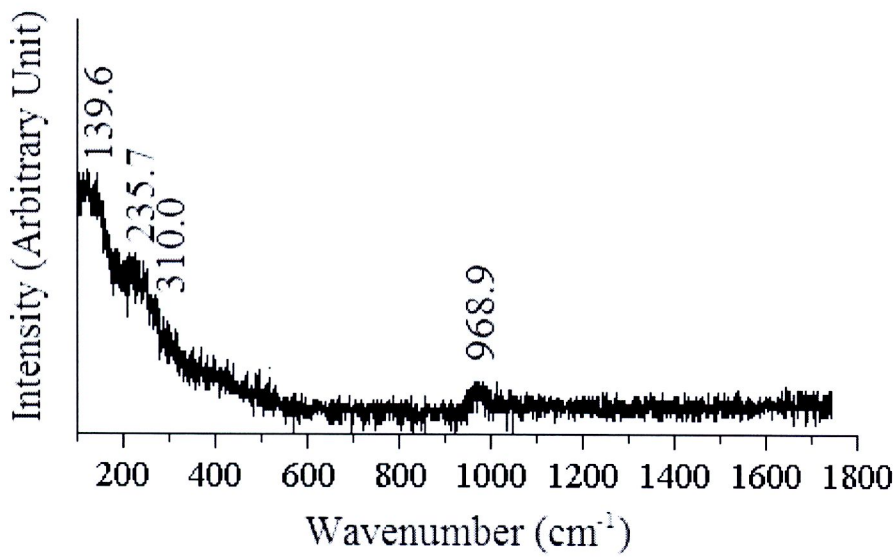

Figure 3.57 Raman spectrum of Bi_2S_3 hydrothermally produced in polymer-free solution at 200 ^{o}C, 20 h

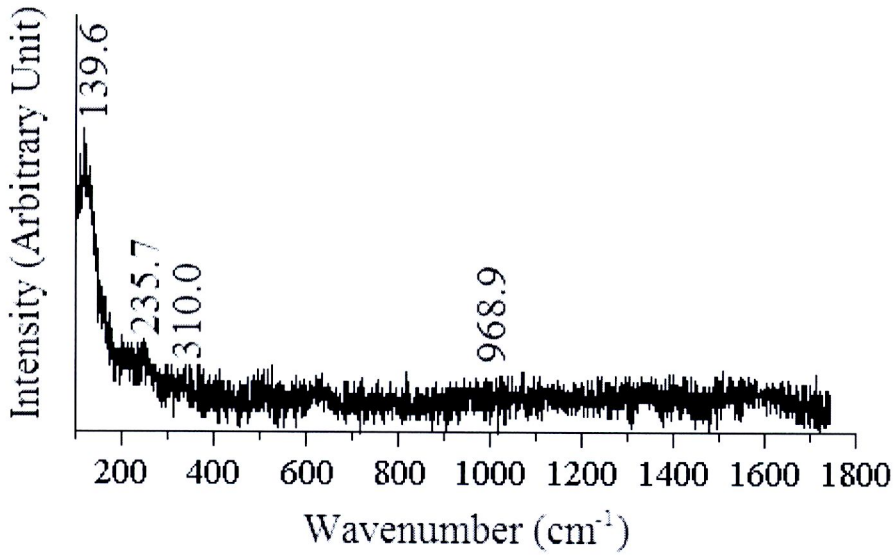

Figure 3.58 Raman spectrum of Bi_2S_3 hydrothermally produced by using 1 g PVA at 200 °C, 20 h

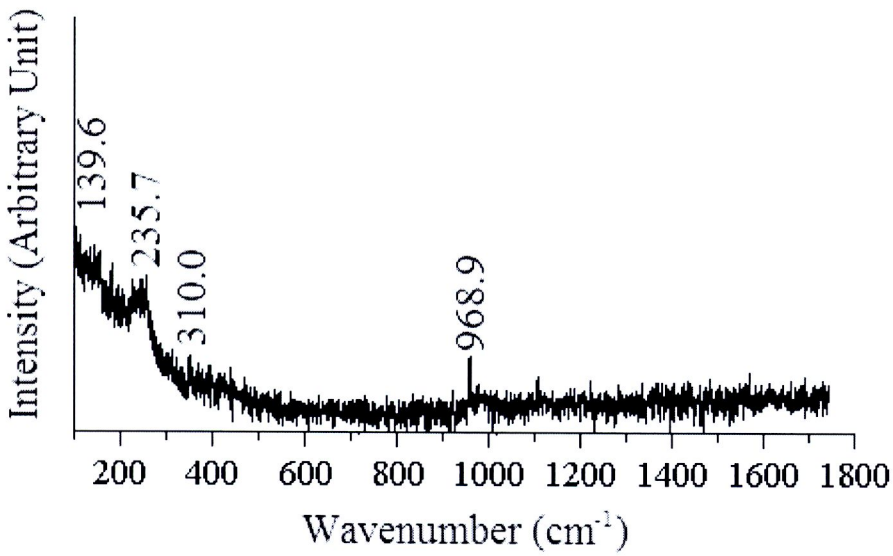

Figure 3.59 Raman spectrum of Bi_2S_3 hydrothermally produced by using 1 g PVP at 200 °C, 20 h

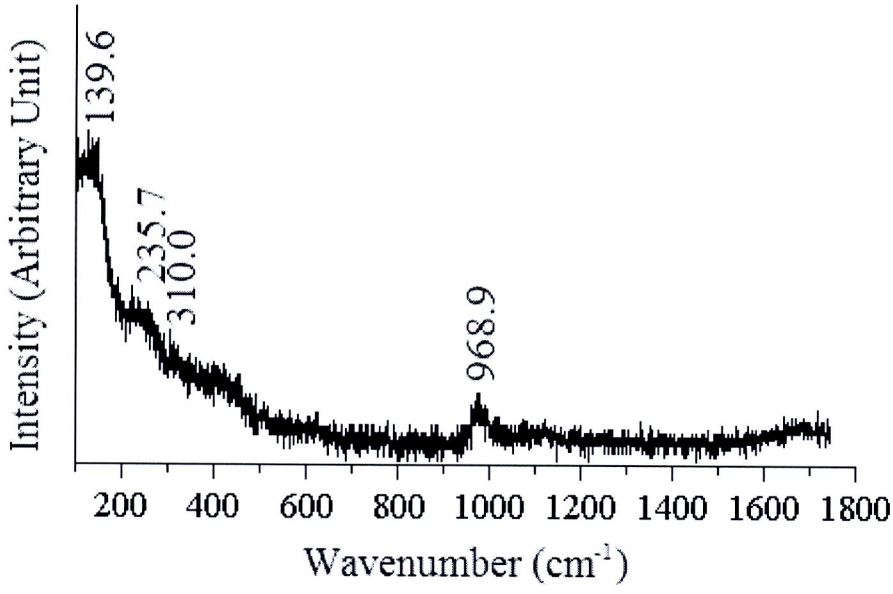

Figure 3.60 Raman spectrum of Bi_2S_3 hydrothermally produced by using 1 g PEG at 200 °C, 20 h

3.2.3 Scanning electron microscopy (SEM)

SEM images of the products prepared using different conditions are shown in Figure 3.61-3.66. In polymer-free solutions at 100 °C for 2 h (Figure 3.61), the product was composed of irregular and short nanorods with different orientations. When only the temperature was increased to 200 °C (Figure 3.62), the longer rods were detected. And both the temperature and time were increased to 200 °C and 20 h (Figure 3.63), the nanorods were of greater length than the former product and they were in clusters. They became flower-like clusters of nanospears, nanorods and nanoplates in PVA-, PEG- and PVP-added solutions, respectively (Figure 3.64-3.66). It is noteworthy that these polymers functioned as templates to control both the shapes and sizes of the nanocrystals (nanospears, nanorods and nanoplates). The nanocrystals in the polymer-added solutions became lengthened, as well. These microsized flowers nucleated and grew from cores, controlled by the templates, nucleation and growth.

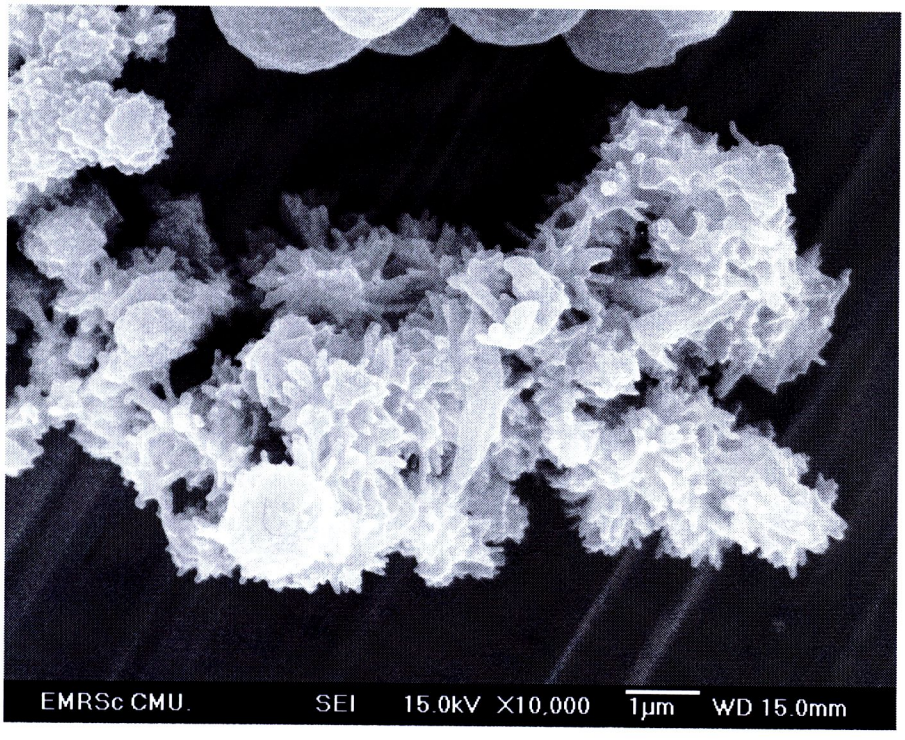

Figure 3.61 SEM image of Bi_2S_3 hydrothermally produced in polymer-free solution at 100 °C, 2 h

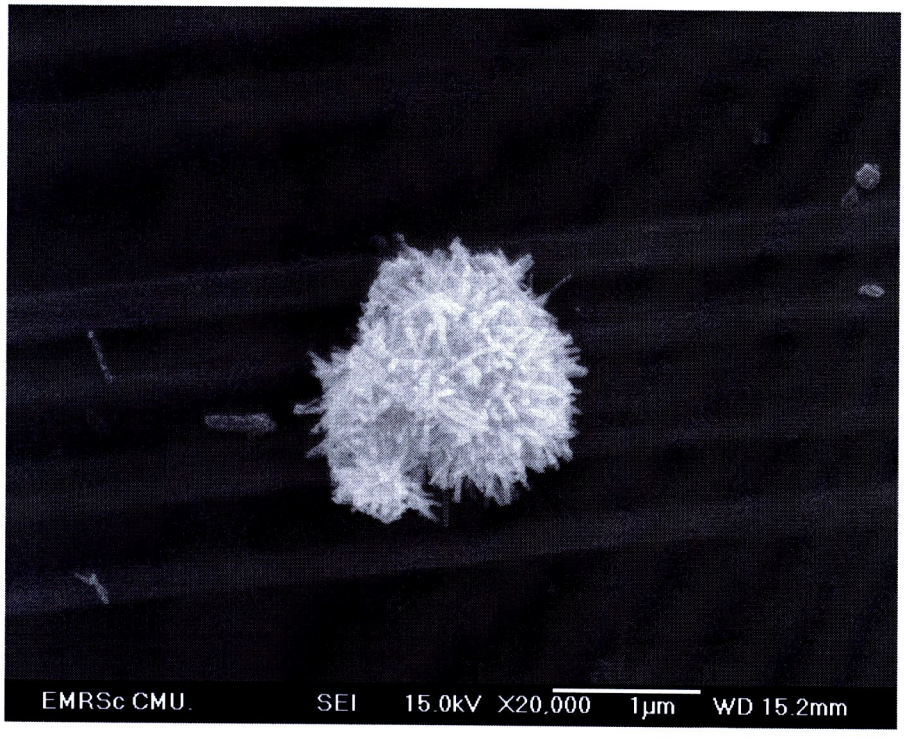

Figure 3.62 SEM image of Bi_2S_3 hydrothermally produced in polymer-free solution at 200 °C, 2 h

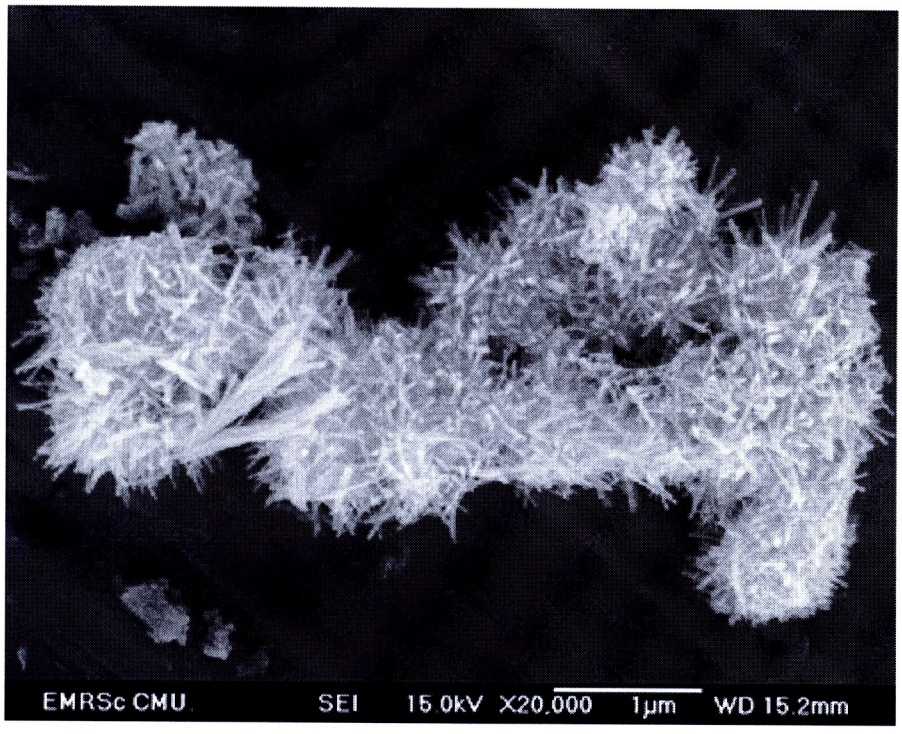

Figure 3.63 SEM image of Bi_2S_3 hydrothermally produced in polymer-free solution at 200 °C, 20 h

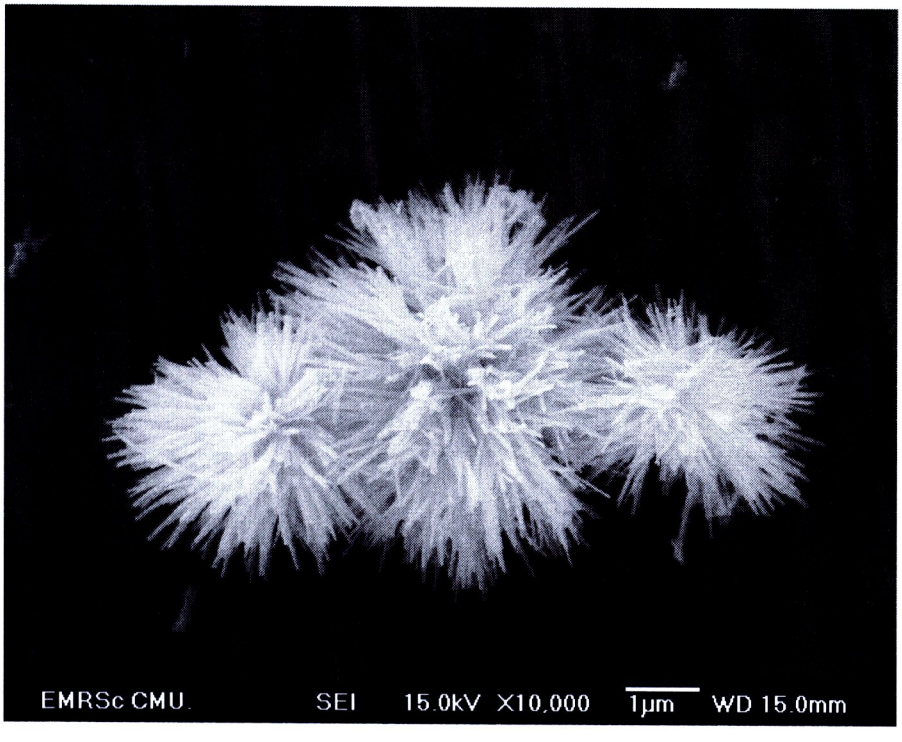

Figure 3.64 SEM image of Bi_2S_3 hydrothermally produced by using 1 g PEG at 200 °C, 20 h

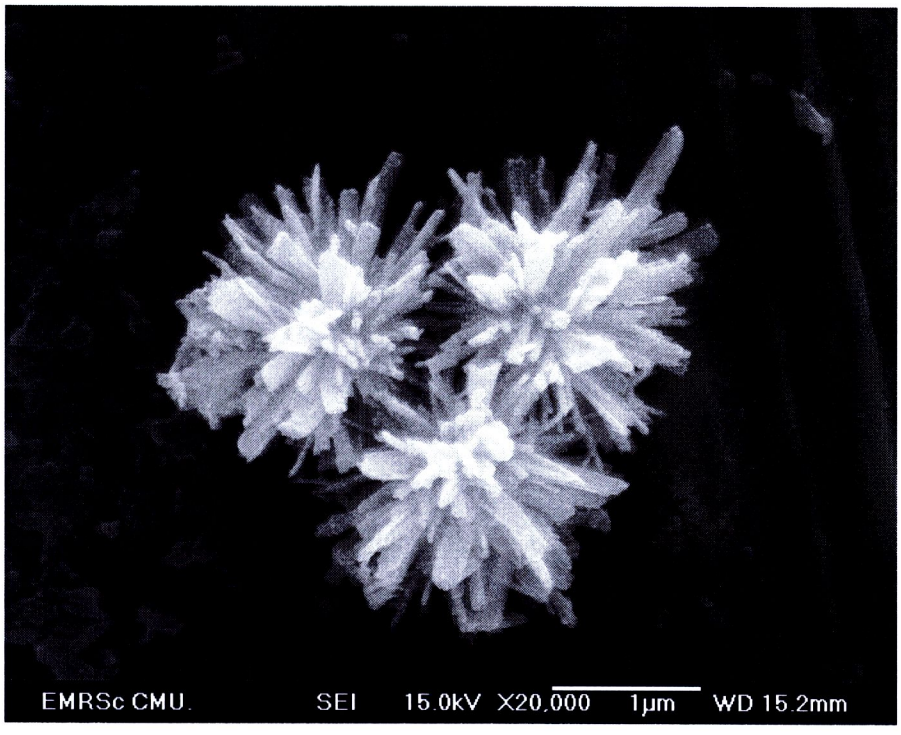

Figure 3.65 SEM image of Bi_2S_3 hydrothermally produced by using 1 g PVP at 200 °C, 20 h

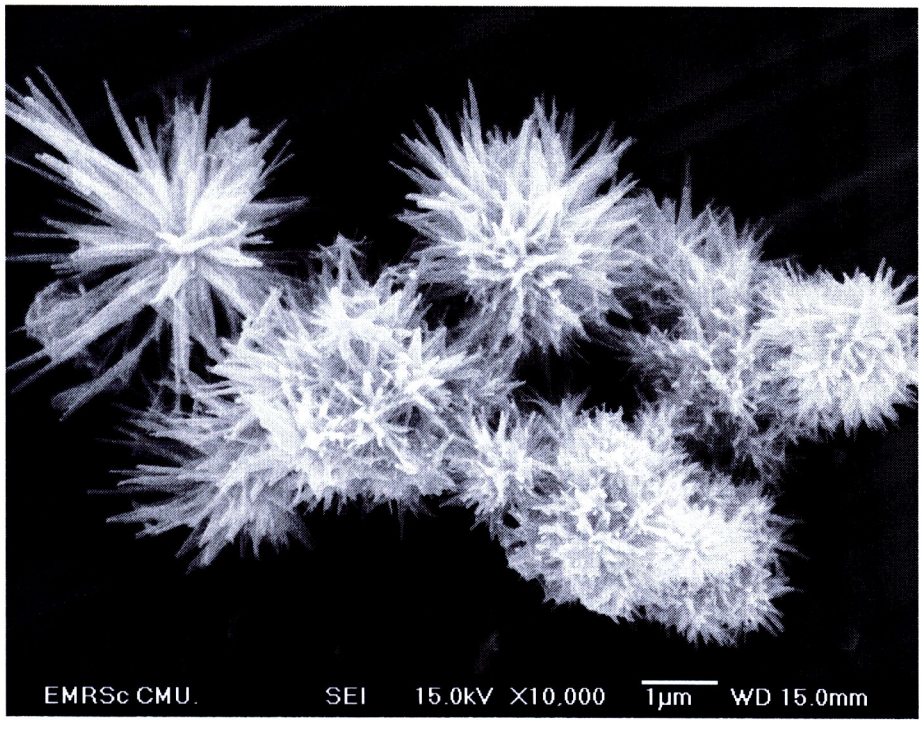

Figure 3.66 SEM image of Bi_2S_3 hydrothermally produced by using 1 g PVA at 200 °C, 20 h

3.2.4 Transmission Electron Microscopy (TEM) and High Resolution Transmission Electron Microscopy

Figures 3.67-3.82 show TEM and HRTEM images of the products produced in different solutions. In polymer-free solution, the product (Figure 3.67) was nanorods with very smooth surfaces, and different diameters - controlled by nucleation and growth, growing in the [001] direction. In polymer-added solutions, the products were flower-like clusters of nanorods (Figure 3.69), nanospears (Fig. 3.71) and nanoplates (Figure 3.74). There was some stress developed inside these nanocrystals as well, such as bent nanospears (Fig. 3.71-3.73). HRTEM analysis show that nanorods, nanospears and nanoplates grew in the same direction of [001] (Figure 3.70, 3.72-3.73, 3.75-3.76). Their growth direction is in accordance with those characterized by other researchers [123-126]. A number of crystallographic planes composing these nanocrystals were detected. They are the (220) planes (Figure 3.70, 3.72, 3.75) which are parallel to the [001] direction. But for the (211) planes (Figs. 3.73, 3.76), they were at different angles to the growth direction, controlled by the electron beam direction relative to the corresponding nanocrystals.

Figure 3.67 TEM image of Bi_2S_3 hydrothermally produced in polymer-free solution at 200 ^{o}C, 20 h

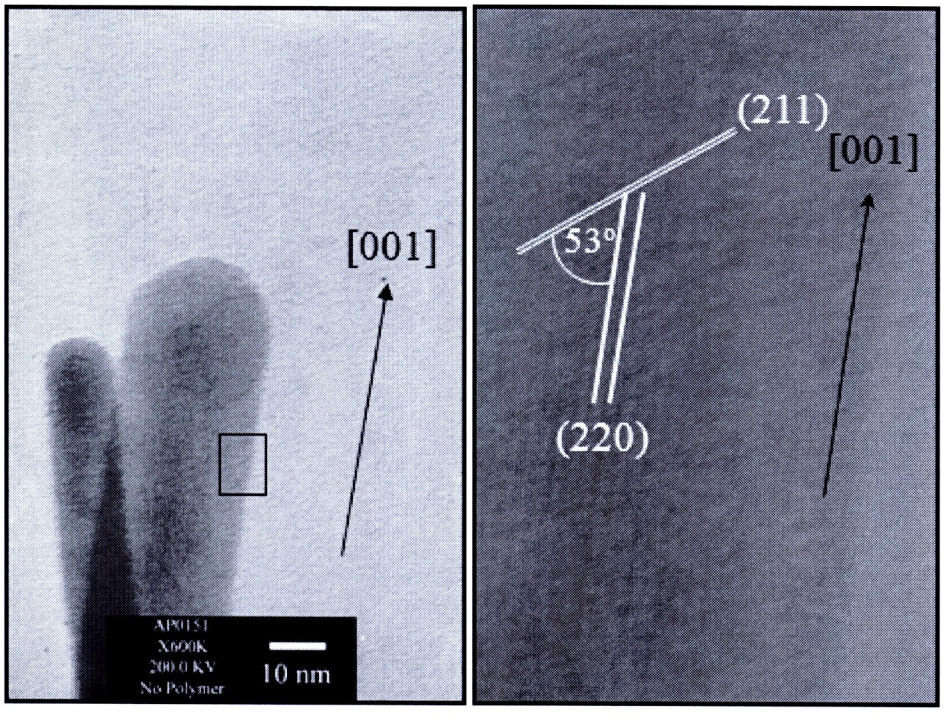

Figure 3.68 HRTEM image of Bi_2S_3 hydrothermally produced in polymer-free solution at 200 ^{o}C, 20 h

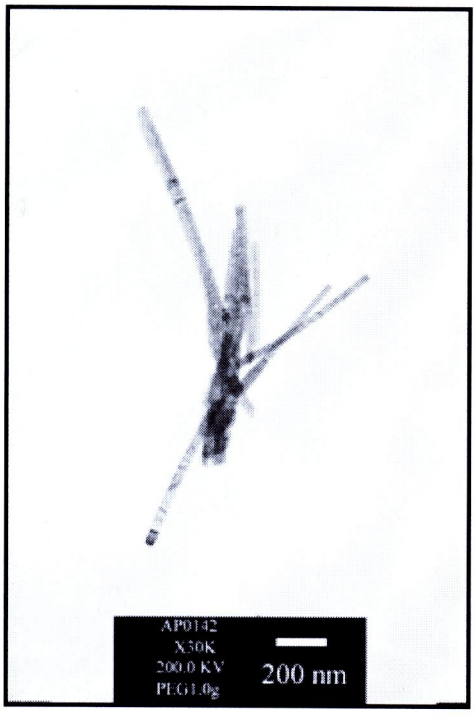

Figure 3.69 TEM image of Bi_2S_3 hydrothermally produced PEG-added solution at 200 °C, 20 h

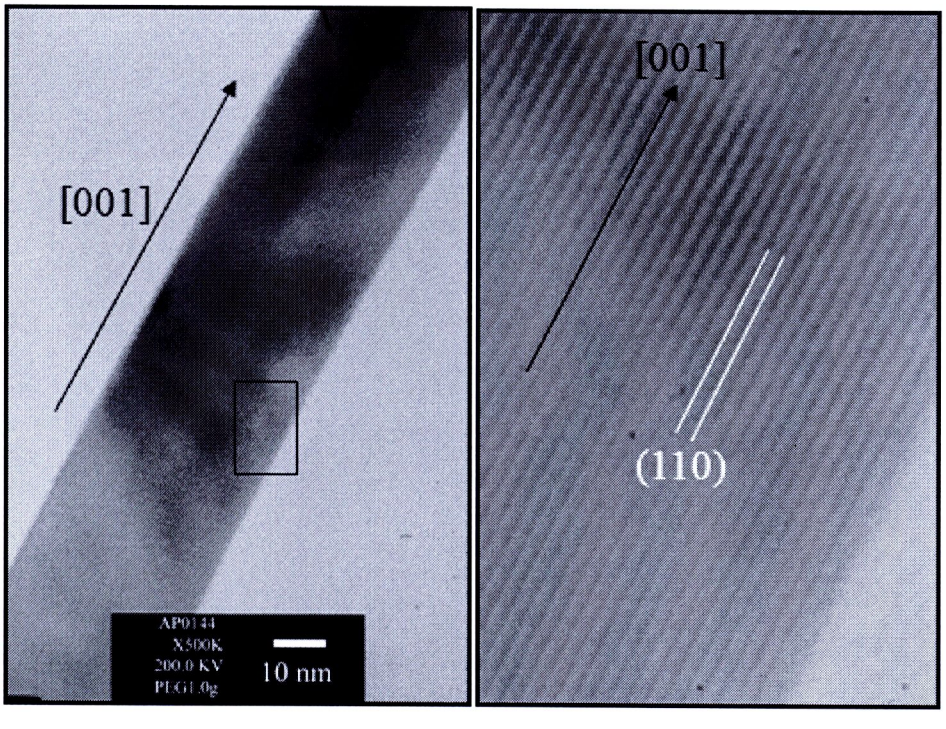

Figure 3.70 HRTEM image of Bi_2S_3 hydrothermally produced in PEG-added solution at 200 °C, 20 h

Figure 3.71 TEM image of Bi_2S_3 hydrothermally produced in PVA-added solution at 200 °C, 20 h

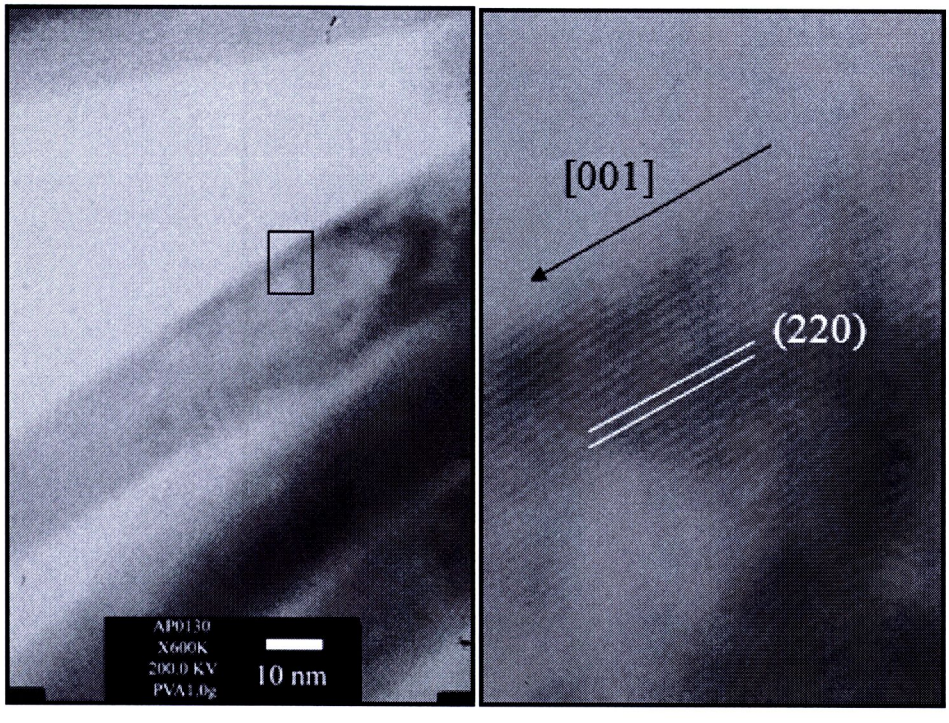

Figure 3.72 HRTEM image of Bi_2S_3 hydrothermally produced in PVA-added solution at 200 °C, 20 h

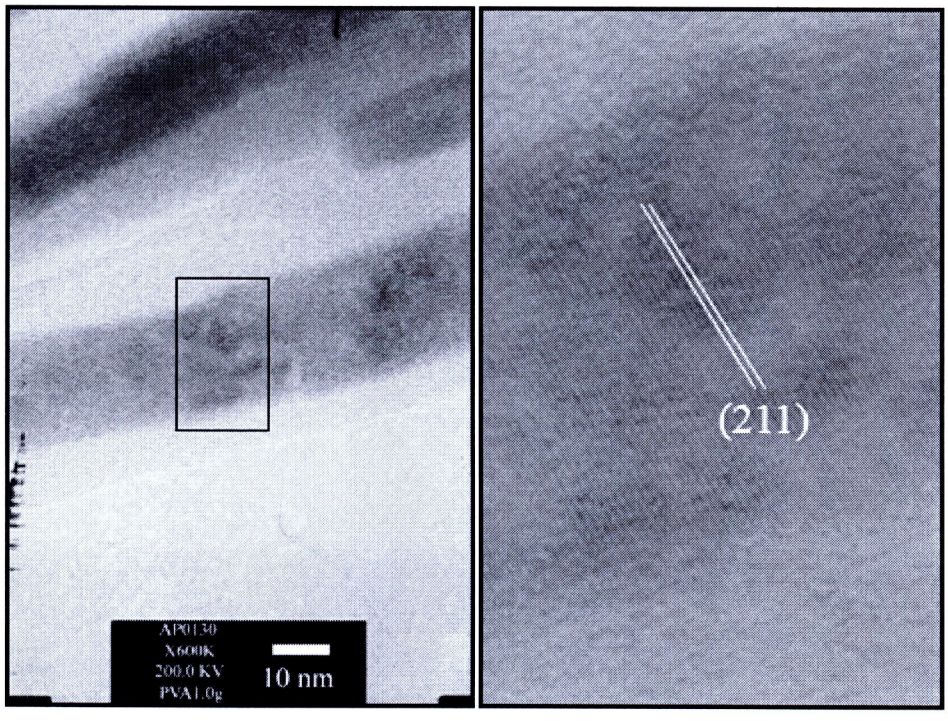

Figure 3.73 HRTEM image of Bi_2S_3 hydrothermally produced in PVA-added solution at 200 °C, 20 h

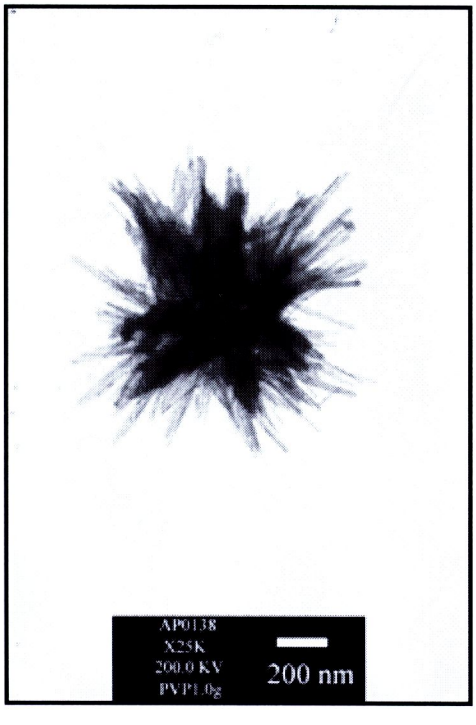

Figure 3.74 TEM image of Bi_2S_3 hydrothermally produced in PVP-added solution at 200 °C, 20 h

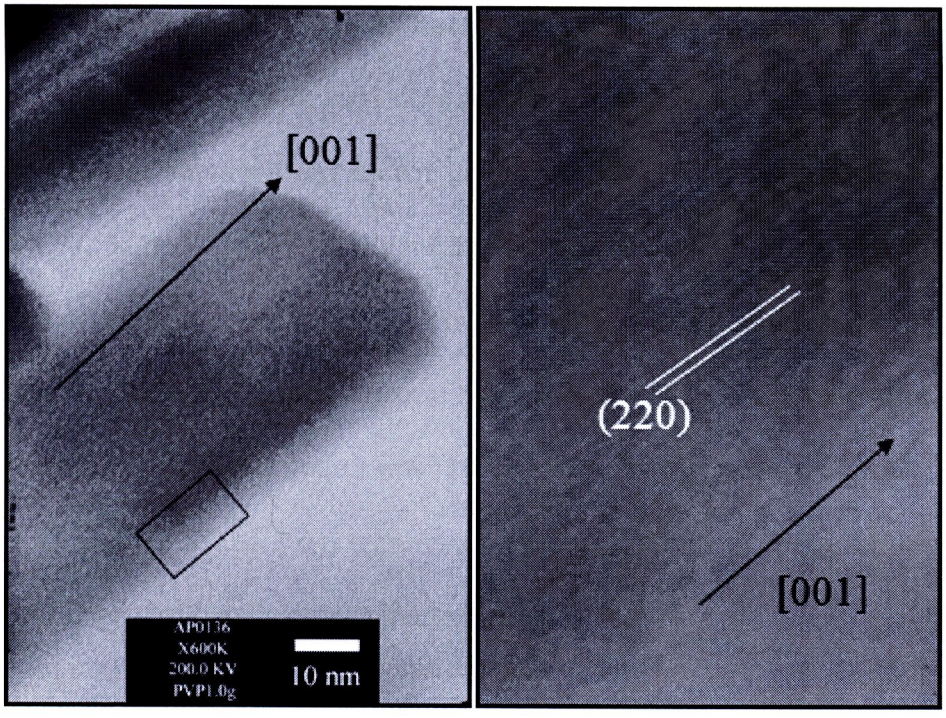

Figure 3.75 HRTEM image of Bi_2S_3 hydrothermally produced in PVP-added solution at 200 °C, 20 h

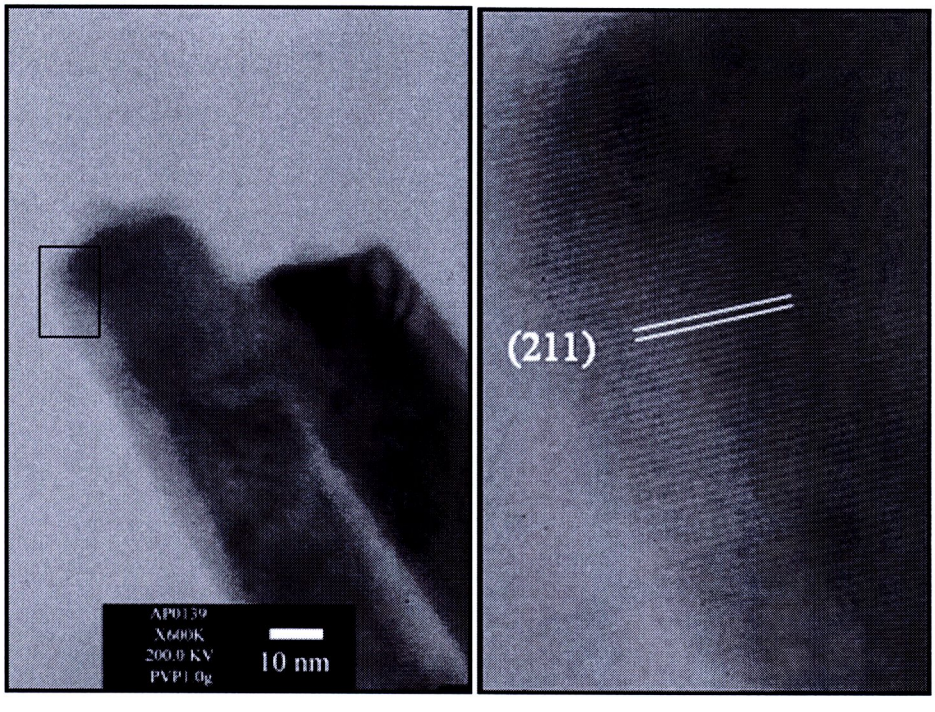

Figure 3.76 HRTEM image of Bi_2S_3 hydrothermally produced in PVP-added solution at 200 °C, 20 h

3.2.5 Selected area electron diffraction (SAED) and simulated patterns

SAED patterns and their simulated pattern of the products produced at 200 ^{o}C, 20 h in different solutions are shown in Figure 3.77-3.84. All diffraction patterns (Figure 3.77, 3.79, 3.81 and 3.83) appears as systematic arrays of spots which show the nature of a single crystal of Bi_2S_3. These patterns were interpreted and indexed to orthorhombic Bi_2S_3. Calculated electron beam direction was in the same direction of [2-10] except PVP-added solution was [100]. A simulated electron diffraction pattern (Figs. 3.78, 3.80, 3.82and 3.84) appears as systematic arrays of spots, corresponding to the SAED pattern obtained from the experiment.

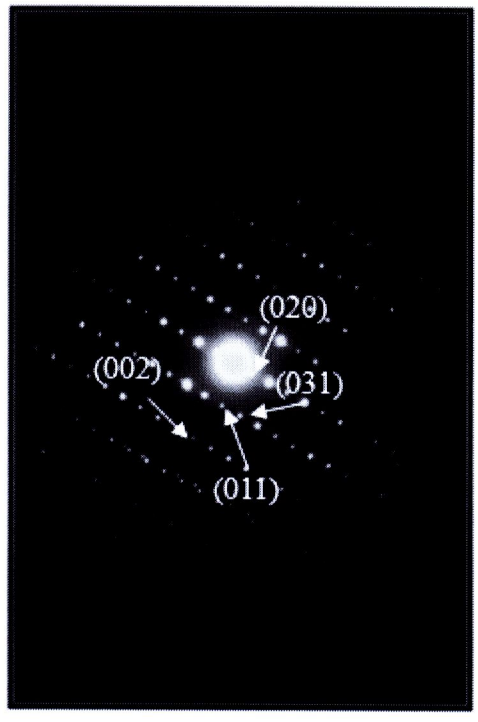

Figure 3.77 SAED pattern of Bi_2S_3 hydrothermally produced in polymer-free solution at 200 °C, 20 h

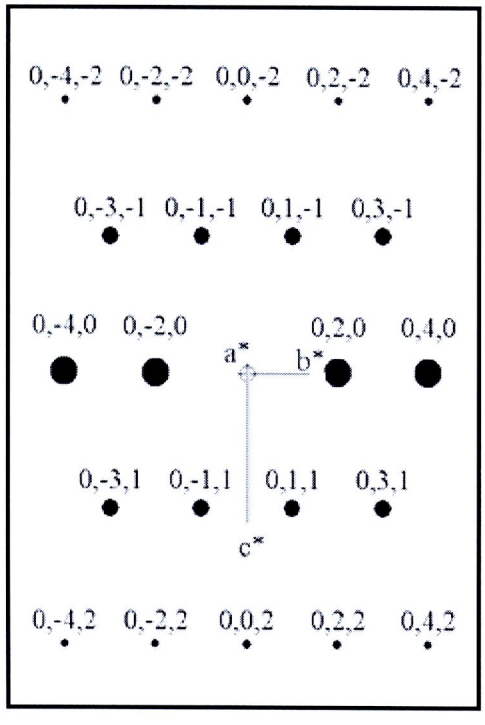

Figure 3.78 Simulated SAED pattern of Bi_2S_3 hydrothermally produced in polymer-free solution at 200 °C, 20 h

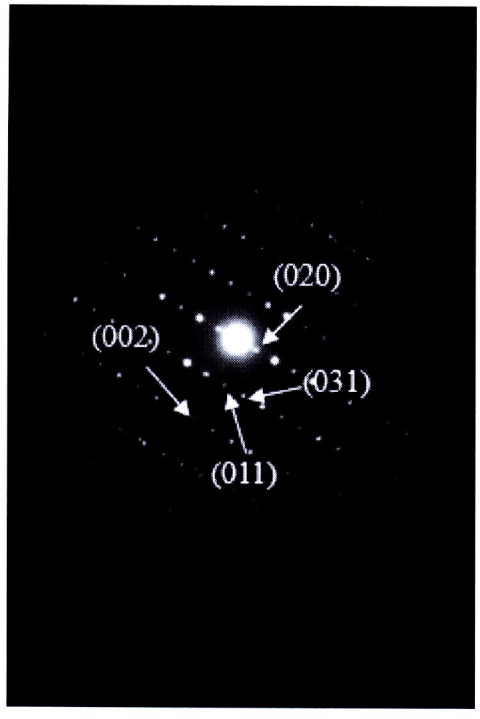

Figure 3.79 SAED pattern of Bi_2S_3 hydrothermally produced in PEG-added solution at 200 °C, 20 h

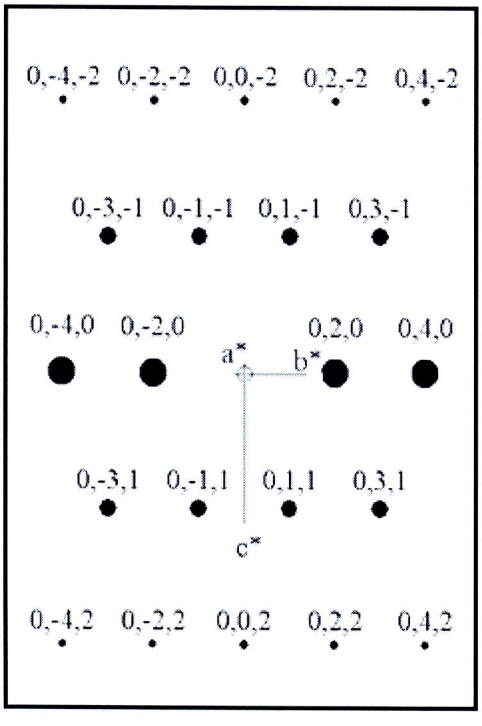

Figure 3.80 Simulated SAED pattern of Bi_2S_3 hydrothermally produced in PEG-added solution at 200 °C, 20 h

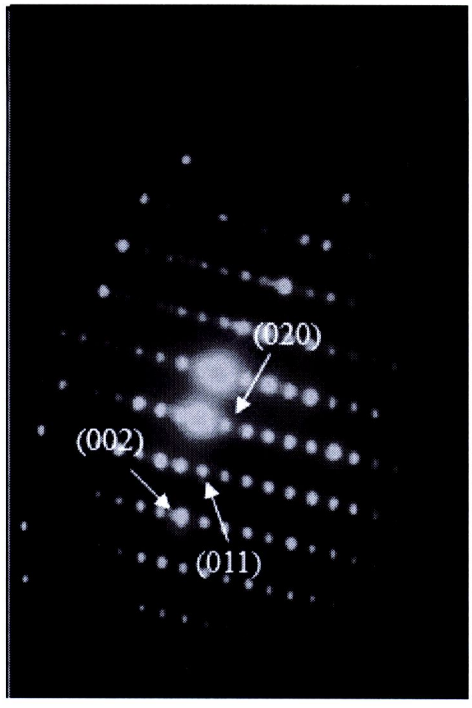

Figure 3.81 SAED pattern of Bi_2S_3 hydrothermally produced in PVA-added solution at 200 °C, 20 h

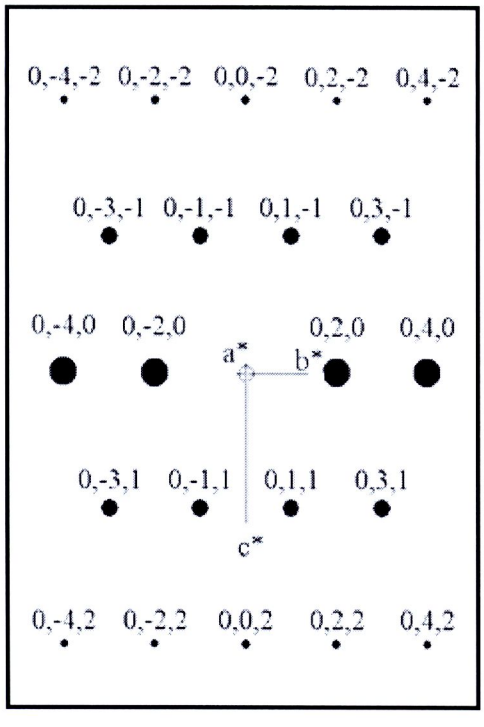

Figure 3.82 Simulated SAED pattern of Bi_2S_3 hydrothermally produced in PVA-added solution at 200 °C, 20 h

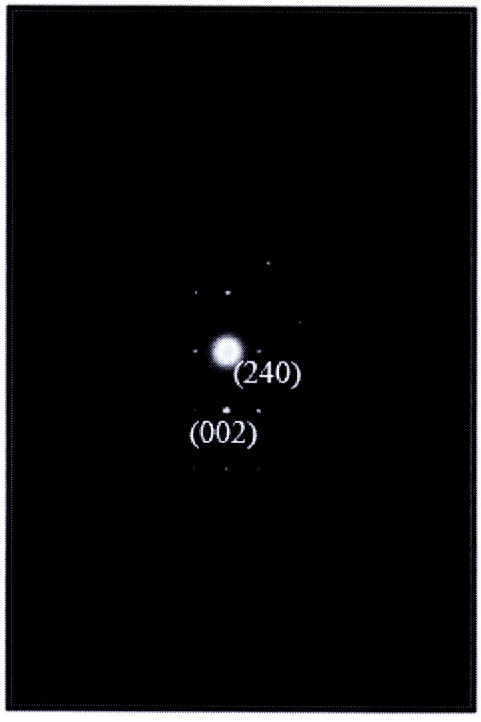

Figure 3.83 SAED pattern of Bi_2S_3 hydrothermally produced in PVP-added solution at 200 °C, 20 h

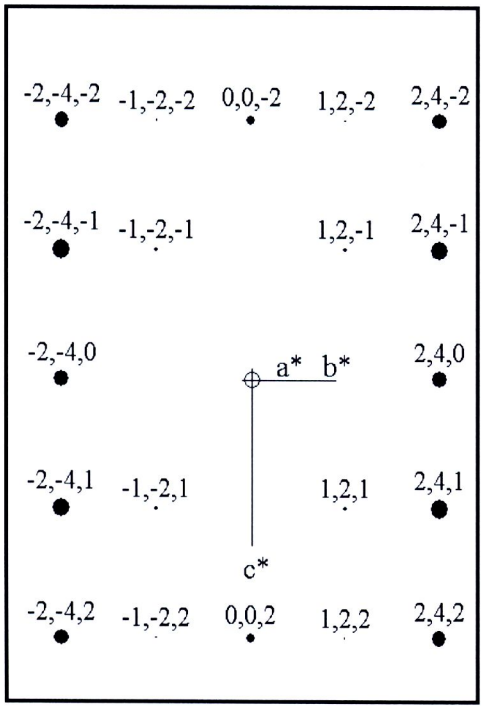

Figure 3.84 Simulated SAED pattern of Bi_2S_3 hydrothermally produced in PVP-added solution at 200 °C, 20 h

3.2.6 Optical properties

Photoluminescent (PL) properties of the products (Figure. 3.85) produced in different solutions were characterized using 300 nm excitation wavelength at room temperature. PL peaks of nanorod clusters, and flower-like clusters were detected at the same wavelengths of 700 nm. The peak was attributed to electron-hole recombination emission. It was also found that the use of one gram PEG resulted in the strongest of the recombination peak. While the use of PEG or PVP still resulted in stronger of the recombination peak than that obtained in polymer-free solution.

UV-NIR spectrum of Bi_2S_3 produced in PEG-added solution (Figure 3.86) shows a wide absorption up to approximately 1200 nm. From this result, we can estimated band gap energy or E_g by the relation between absorbance and photon energy as shown in this equation

$$\alpha h\nu = A(h\nu - E_g)^{1/2}$$

The band gap E_g was determined by extrapolating the straight-line portion of the plot of absorbance versus photon energy to the energy axis at $\alpha = 0$. It was found that the band gap energy of the Bi_2S_3 produced in PEG-added solution was approximately 1.7 eV. From these results, we can conclude that the use of polymers (especially for PEG) can improve the optical properties of Bi_2S_3.

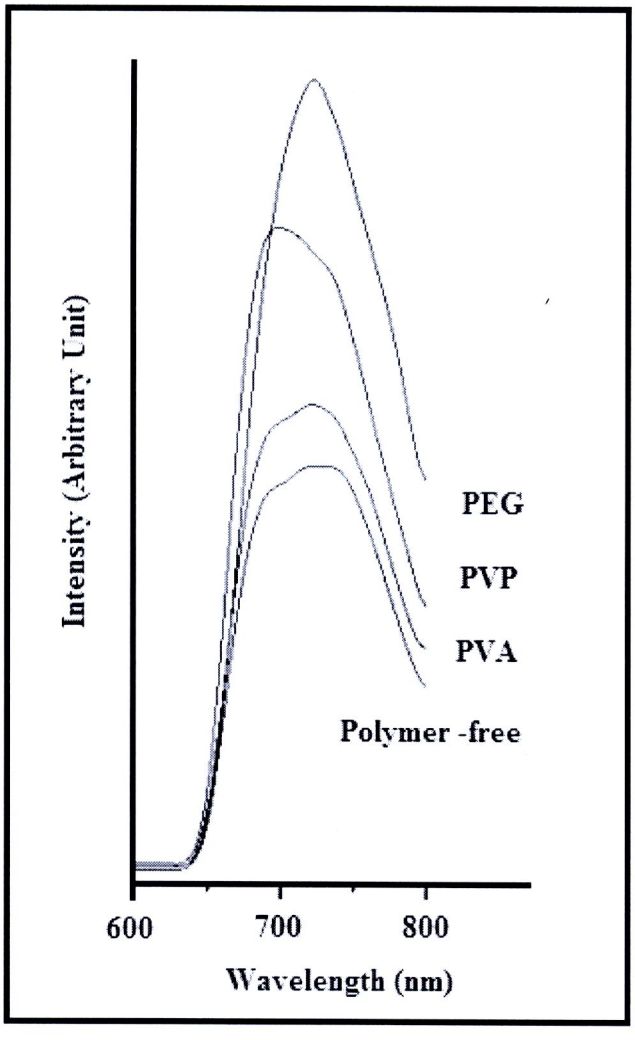

Figure 3.85 PL emissions of Bi_2S_3 hydrothermally produced in different solutions at 200 ^{o}C, 20 h

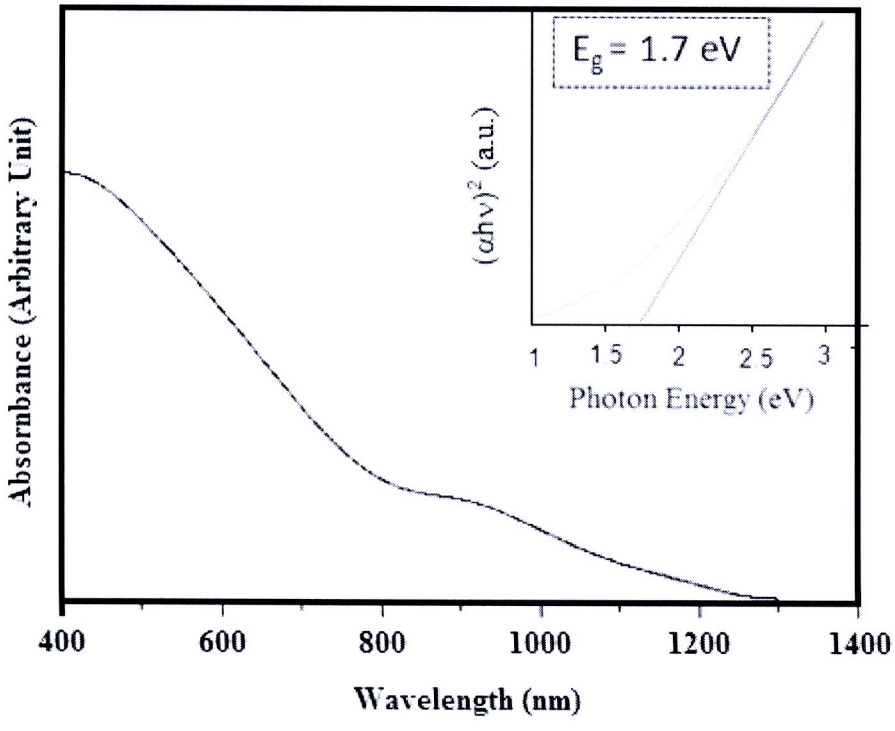

Figure 3.86 UV-NIR absorption of Bi_2S_3 hydrothermally synthesized PEG-added solutions at 200 ^{o}C for 20 h

3.2.7 Formation mechanism

For the present research, the formation of Bi_2S_3 is proposed as follows. At room temperature, Bi_2O_3 reacted with HCl to form $BiCl_3$ [127].

$$Bi_2O_3 + 6HCl \rightarrow 2BiCl_3 + 3H_2O$$

Bi^{3+} formed complex with CH_6N_4S, and color of the solutions was yellow tea.

$$Bi^{3+} + 3CH_6N_4S \rightarrow [Bi(CH_6N_4S)_3]^{3+} \text{ (yellow tea)}$$

$[Bi(CH_6N_4S)_3]^{3+}$ complex hydrothermally decomposed, and Bi_2S_3 black precipitates were produced.

$$2[Bi(CH_6N_4S)_3]^{3+} \rightarrow Bi_2S_3 \text{ (black)}$$

In polymer-free solution, Bi_2S_3 nuclei formed and grew into nanorods along the [001] direction, due to their Bi-S inherent chain type structure [129], which simultaneously clustered into groups. In polymer-added solutions, nuclei were attached on polymer chain via electrostatic interaction between metal ions and oxygen atoms in polymer and then clustered into very tiny spheres. There are a number of active sites on these spherical surfaces, at which nanocrystals (nanospears, nanorods and nanoplates) grew. Simultaneously, polymer molecules adsorbed on side walls of these nanocrystals, of which the lateral growths were inhibited to some extent. The tips were the most active, and these nanocrystals became lengthened [128]. Their Bi-S inherent chain type structure [129] has the influence in promoting the formation of the nanocrystals, growing from cores, as well. Thus Bi_2S_3 nanocrystals grew out of the active sites on the spheres, and flower-like clusters were finally produced.

3.2.7 Utilization of Bi_2S_3 in solar cell

As mentioned in the introduction part, solar cells are considered as one of the most promising options to solve the energy crisis. One of the technical issues with the solar cells is the cost to efficiency ratio. Dye-sensitized solar cells (DSSCs) have recently stimulated much research interests, largely due to its lower cost as compared to the silicon based and thin film counterparts. However, there are some drawbacks of such solar cell for example stability, efficiency and etc. Various approaches have been explored in attempts for further improvement, including the use of nanocrystalline semiconductors, the hole- transport material, NIR dyes, and dual sensitization of dyes or QDs and dyes. In this work, metal sulfides synthesized in this research were utilized to improve the efficiency of the DSSC.

It was reported that the flower-like nanorod can provide larger surface area, increased light-dye interactions, and better electron transportation [130]. Thus, Bi_2S_3 nanoflower synthesized by PEG-assisted hydrothermal method was used as cosensitized material in hybrid (Bi_2S_3 and Eosin Y) sensitized solar cell (HSSC). Hybrid structures of semiconductor and dye can, in an ideal case, simultaneously satisfy several important requirements for light harvesting materials for example (i) extend the spectral absorption range by adding up the absorption ranges of both components, (ii) reduce the internal charge recombination by fast hole scavenging from semiconductor and efficient spatial separation of electrons and holes via a multistep charge separation cascade and (iii) improve charge extraction by the reduction of recombination losses in semiconductor [131].

In typical fabrication of HSSC, TiO_2 paste was coated on FTO glass (Solaronic, 8Ω/□) by using doctor blade method, followed by calcinations at 400 °C for 1 h (Film

area = 1x1 cm^2). After that, Bi_2S_3 nanoflower was coated on the photoelectrode by spin coating. Then, Bi_2S_3 coated photoelectrode was soaked in Eosin Y solution overnight. After that the TiO_2/Bi_2S_3/Eosin Y photoelectrode was assembled with Pt counter electrode. The gap between two electrodes was maintained by thermal plastic spacer. Finally, the gel electrolyte (PEG and iodide electrolyte) was injected into the cell by capillary effect. Figure 3.87 shows schematic arrangement of normal DSSC and HSSC with their J-V curves.

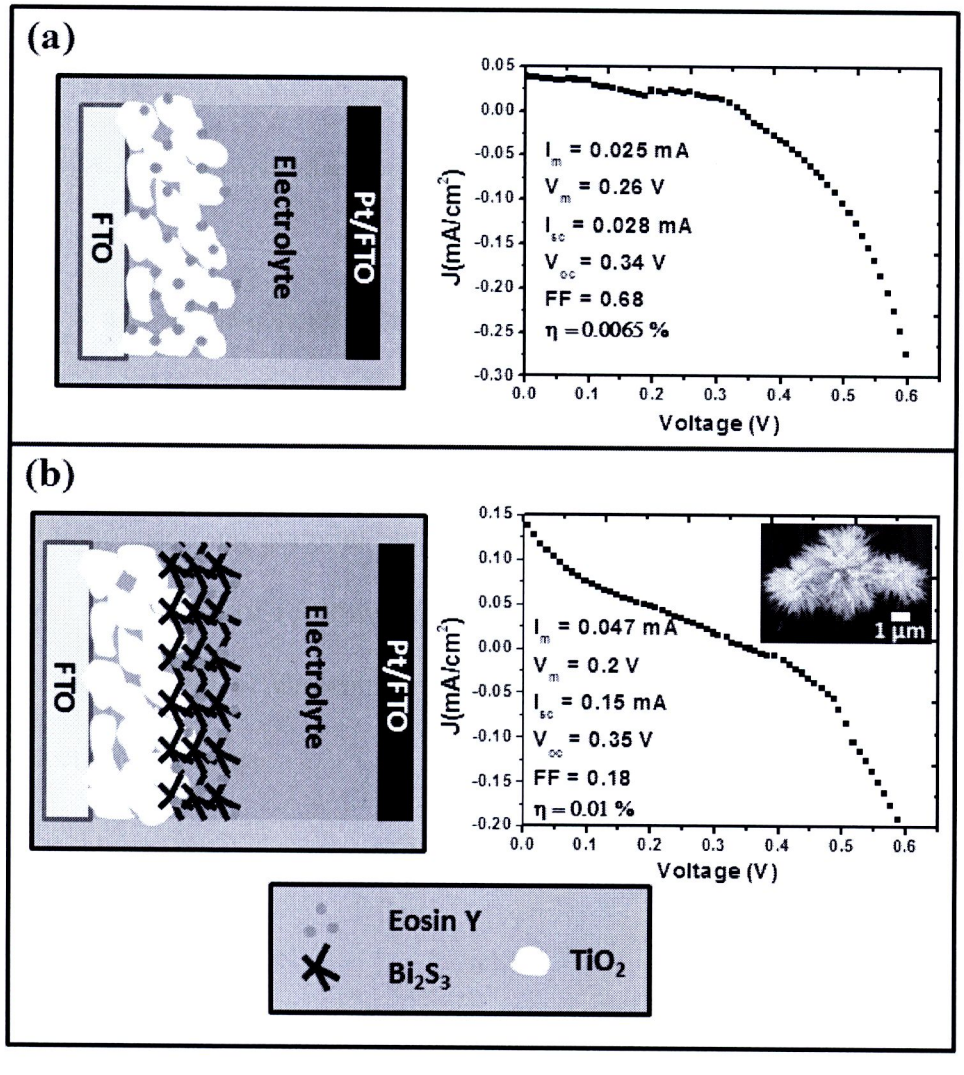

Figure 3.87 Schematic arrangements and J-V curves of (a) DSSC, and (b) HSSC

The photoelectrochemical characteristics of both DSSCs and HSSC were tested under simulated sunlight AM 1.5 came from a solar simulator with the radiant power of 100 mW/cm^2. The incident light intensity was calibrated with thermal sensor. J-V characteristic were measured with a DC voltage and current source which interfaced and controlled by a computer. The photoconversion efficiency (η) was determined from the measured J-V curves. It can be seen that the current density (J_{sc}) and open-circuit voltages (V_{oc}) of DSSC and HSSC are 0.028, 0.15 mA/cm^2, and 0.34, 0.35 V, respectively. The fill factor (FF) of HSSC (0.18) is lower than that of DSSC (0.68). This may be due to the high sheet resistance of HSSC. However, the photoconversion efficiency of HSSC is higher than that observed in DSSC because the use of Bi_2S_3 as co-sensitized can enhance charge carrier density and reduce internal recombination within the cell.

This is a proof-of-concept that the use of Bi_2S_3 as co-sensitizer in HSSC can improve the efficiency of the solar cell. However, the efficiency was still low. The future development of HSSC will rely on three main aspects, (i) materials, including not only light-absorbing material but also electron and hole conductors and counter electrodes, (ii) control of recombination and band alignment by surface treatments, and (iii) development of absorbing nanocomposites with enhanced light-harvesting and -collecting properties.

3.3 CuS synthesized by a PEG-assisted solvothermal method

3.3.1 X-ray diffraction (XRD)

Figures 3.88-3.91 show XRD patterns of the as-synthesized products in 5 g PEG6000-added solution with different amount of formic acid (HCOOH). For HCOOH-free solution and solution containing 1.5 ml formic acid, all diffraction peaks were indexed and specified as hexagonal structure covellite CuS, with no detection of impurities such as metallic copper and cupric oxide. They were narrow and sharp, specifying that the X-ray radiation reflected and diffracted from atoms arranged in lattice order. Calculated lattice constants were a = b = 3.78 Å and c = 16.32 Å, which were in accordance with the JCPDS database [109]. However, cupric sulfide (Cu_2S) was detected in solution containing 3.0 and 5.0 ml formic acid. This may be due to a strong reductant of formic acid which can reduce Cu^{2+} to Cu^{+}[132]. Thus, excess formic acid was not requested.

XRD pattern of covellite CuS was also simulated using CaRIne program [24] in combination with the calculated lattice constants (Figure 3.92). This simulated pattern was used to specify that the experimental pattern could exist in reality. The 2□ Bragg's angles and relative intensities (I_R) of the diffraction peaks obtained from the experiment, simulation and database are summarized in Table 3.4. The XRD peaks obtained from the experiment were in good accordance with those of the simulation and JCPDS database. Relative intensity of the (110) peak obtained from the experiment was significantly stronger than those of the simulation and database, which indicates the preferential growth process.

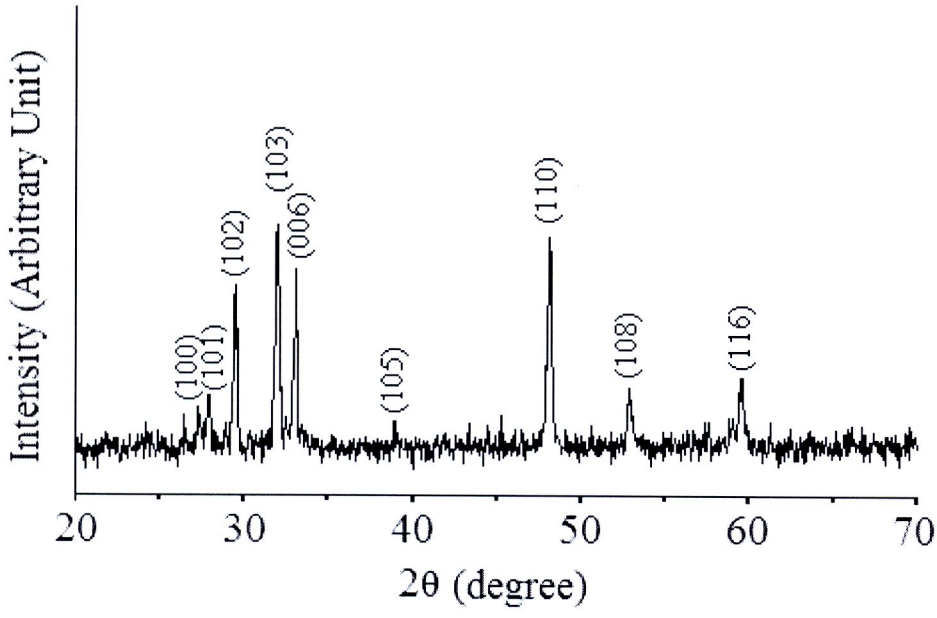

Figure 3.88 XRD pattern of the product synthesized in 5 g PEG6000-added solution containing 0.0 ml HCOOH at 200 °C for 5 h

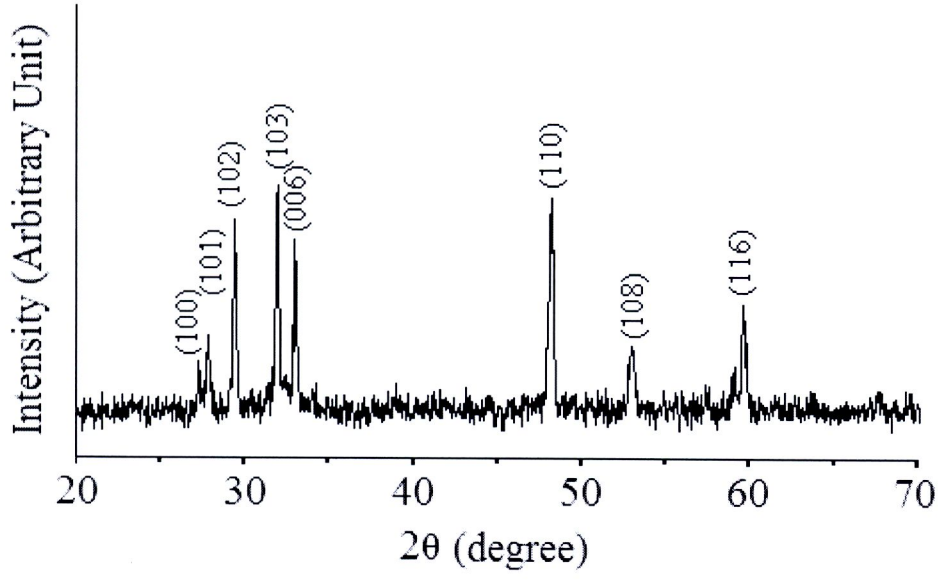

Figure 3.89 XRD pattern of the product synthesized in 5 g PEG6000-added solution containing 1.5 ml HCOOH at 200 °C for 5 h

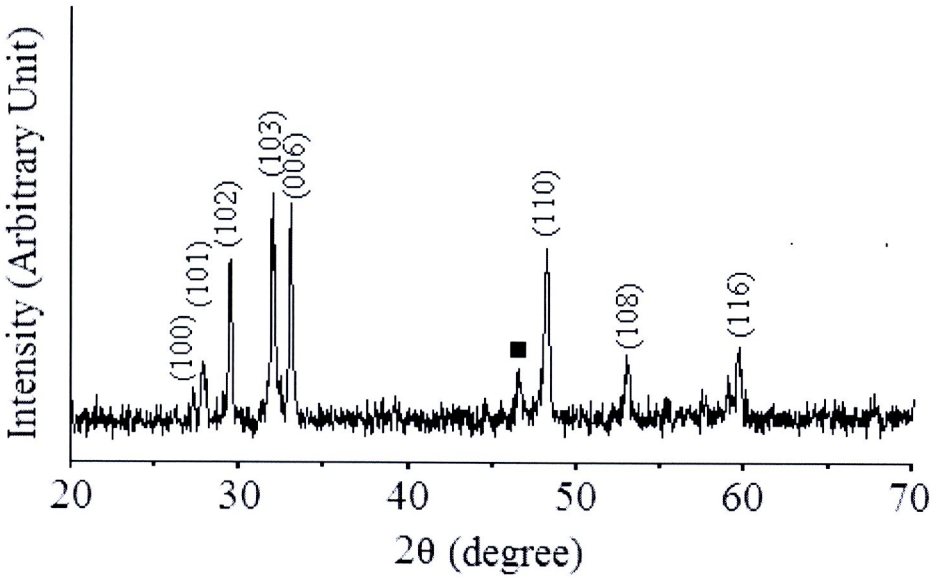

Figure 3.90 XRD pattern of the product synthesized in 5 g PEG6000-added solution containing 3.0 ml HCOOH at 200 °C for 5 h

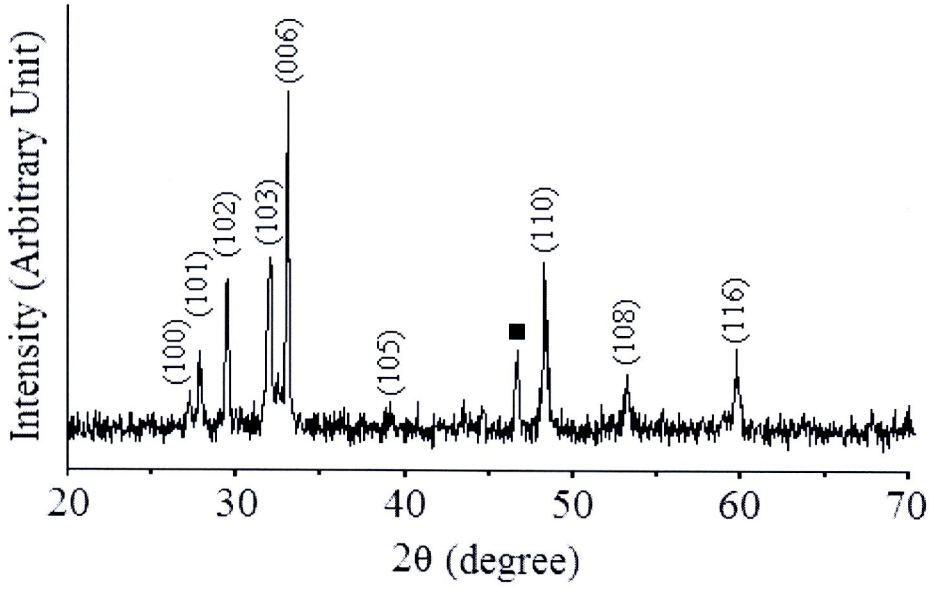

Figure 3.91 XRD pattern of the product synthesized in 5 g PEG6000-added solution containing 5.0 ml HCOOH at 200 °C for 5 h

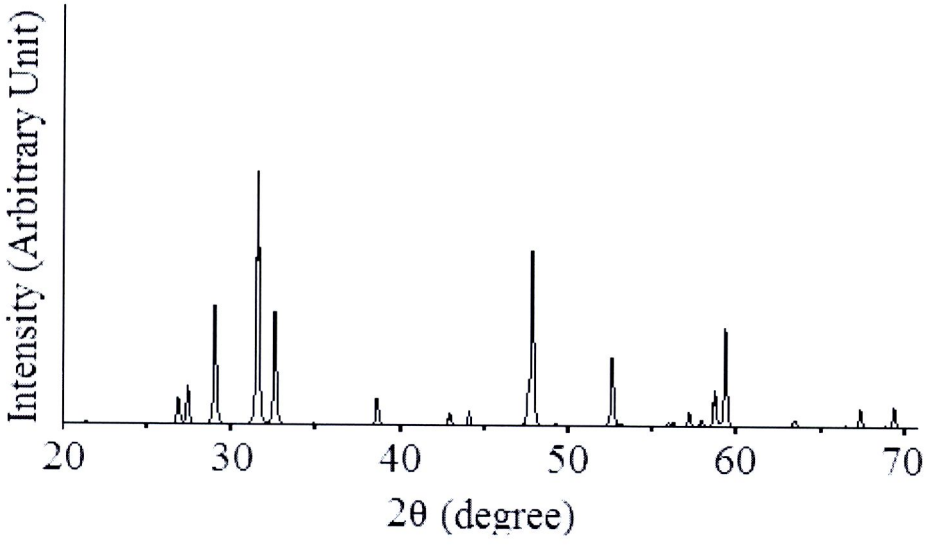

Figure 3.92 Simulated XRD patternof CuS hexagonal structure

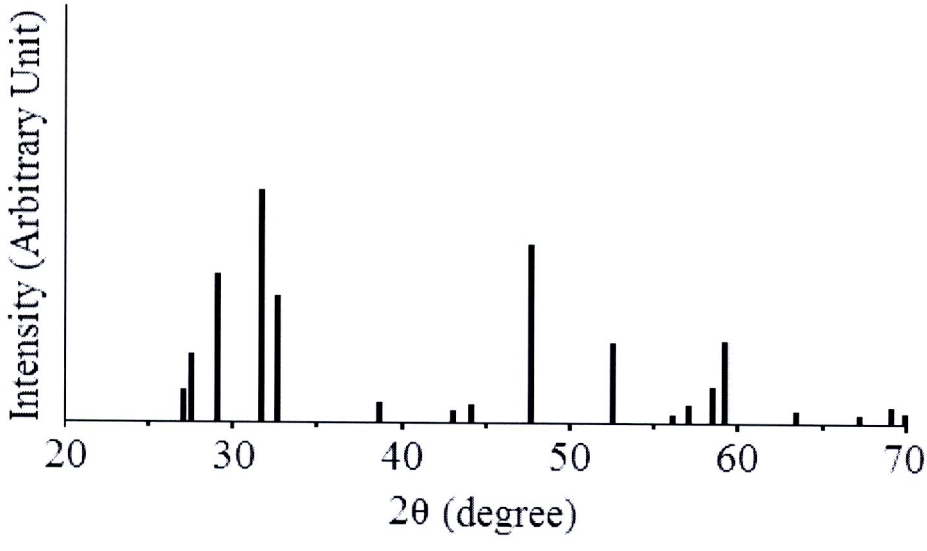

Figure 3.93 JCPDS database of XRD patterns of CuS hexagonal structure

Table 3.6 The 2θ Bragg's angles and relative intensities (I_R) of the diffraction peaks obtained from the experiment, simulation and database

Plane	Experiment		Simulation		JCPDS database	
	2θ	I_R	2θ	I_R	2θ	I_R
(102)	29.41	35.29	29.37	47.00	29.29	65.00
(103)	31.93	100.00	31.88	100.00	31.79	100.00
(006)	32.99	81.21	32.90	45.00	32.85	55.00
(110)	48.15	103.11	48.10	69.10	47.94	75.00

3.3.2 Raman spectroscopy

Figure 3.94-3.96 shows Raman spectra of the product produced in solution containing different amount of formic acid. In formic acid-free solution, the sharp peak at 475 cm^{-1} was caused by lattice vibration and the broaden peak at 263 cm^{-1} by Cu-S vibration [78]. By using 1.5 ml formic acid, Raman peak at 475 cm^{-1}, lattice vibration mode became rather broad. This may be due to nanosized effect of the product. When 5.0 ml formic acid was added in the solution, the Raman peaks was also detected at approximately 470 cm^{-1} although cubic phase was detected. However, Raman spectroscopy cannot distinguish between cubic phase and hexagonal phase.

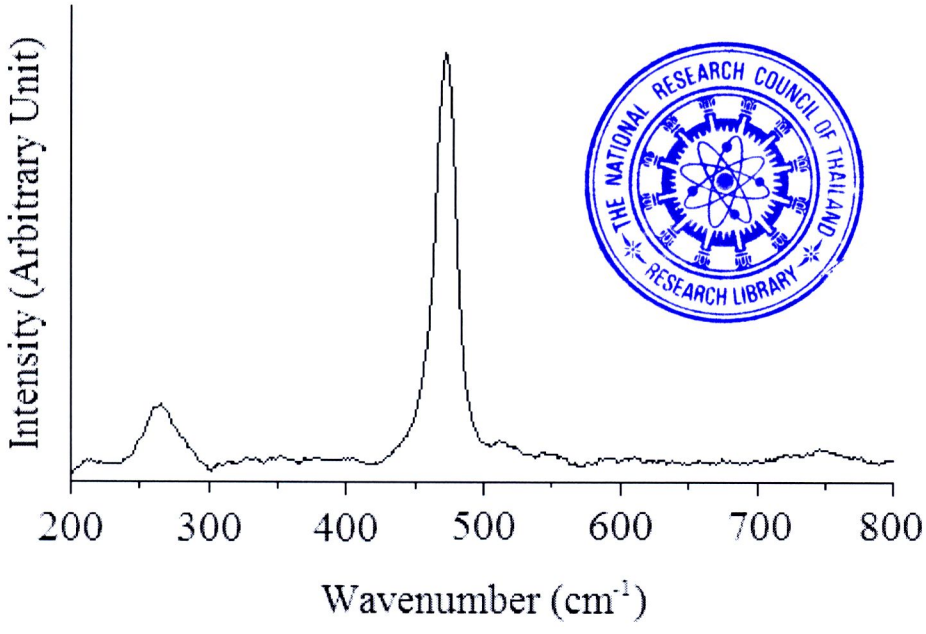

Figure 3.94 Raman spectrum of the product synthesized in 5 g PEG6000-added solution containing 0.0 ml HCOOH at 200 °C for 5 h

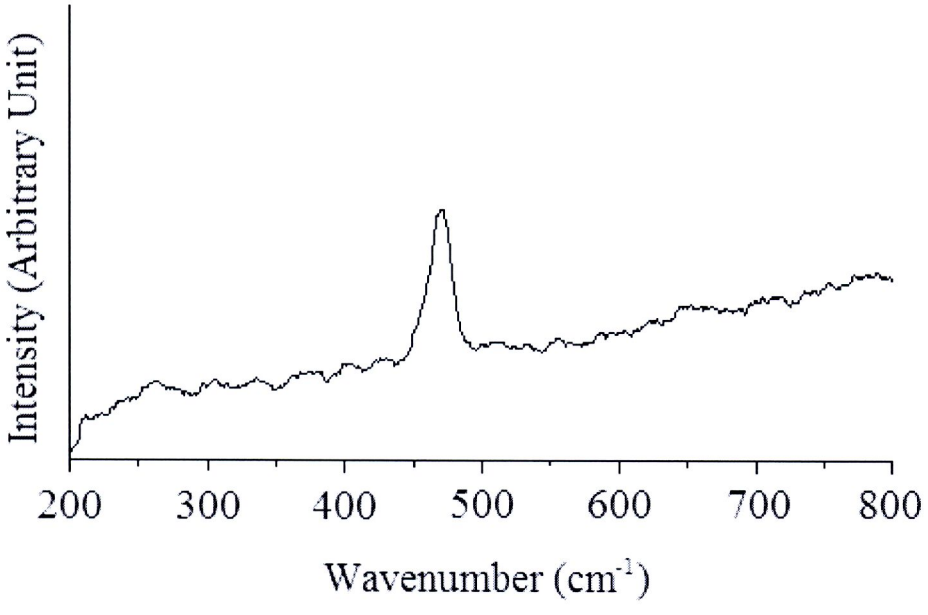

Figure 3.95 Raman spectrum of the product synthesized in 5 g PEG6000-added solution containing 1.5 ml HCOOH at 200 °C for 5 h

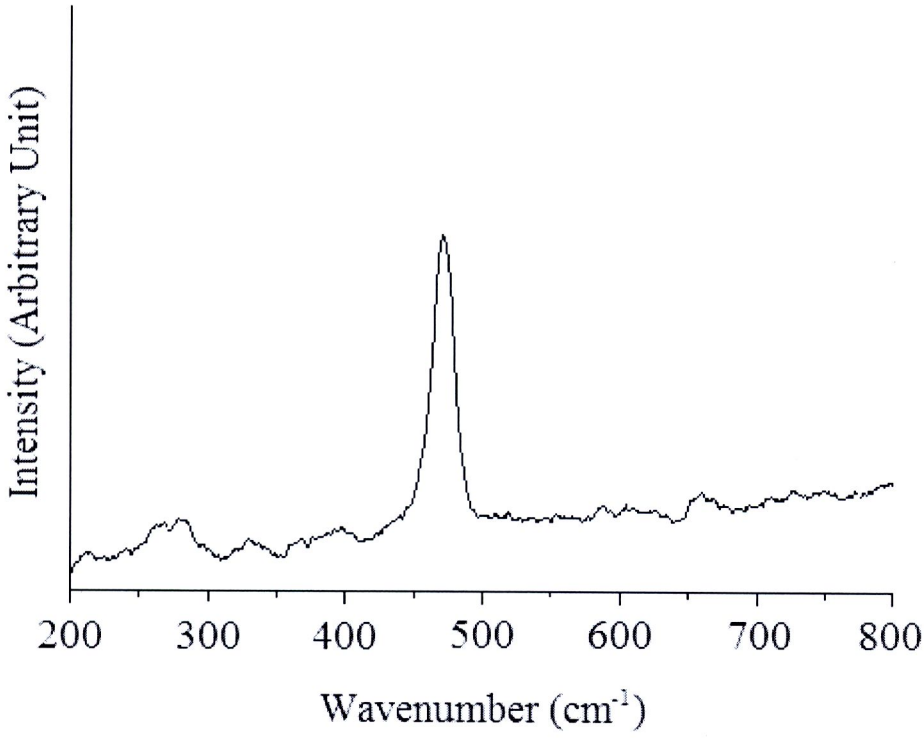

Figure 3.96 Raman spectrum of the product synthesized in 5 g PEG6000-added solution containing 5 ml HCOOH at 200 °C for 5 h

3.3.3 Scanning electron microscopy (SEM)

Figure 3.98-3.101 show SEM images of the products synthesized in 5 g PEG6000-added solution with different amount of formic acid (HCOOH) at 200 °C for 5 h. In formic acid-free solution, CuS microflowers were detected but the use of formic acid, CuS nanoplates were obtained. From this result, it may be ascribed that formic acid, weak electrolyte with low degree of dissociation, can stabilize a pH in the system. The suitable pH value could kinetically control the growth rate of nanoplates. However, excess formic acid, not only irregular plate shape but also cubic phase (Cu_2S) was also detected (as mentioned above).

By using 1.5 ml HCOOH, 5 g PEG6000 and 1 h, the product (Fig. 3.102) was composed of nanoplatelets and nanoparticles. As the reaction time passed, the product became larger by the Ostwald ripening process: larger particles grow at the expense of smaller ones [133]. More nanoplates and less nanoparticles were detected in the product synthesized for 3 h (Fig. 3.103). There were a number of hexagonal plates with no nanoparticles existing in the product of 5 g PEG6000 and 5 h (Figure 3.99).

Figure 3.97 shows the formation diagram of CuS nanoplates, $CuCl_2.2H_2O$ reacted with $(NH_4)_2S$ to form CuS nuclei. Each CuS nuclei grew to form platelets composing of hcp unit cells in lattice order. Growth proceeded according to the crystal structure, which were associated with energies of different faces on the nuclei, specifying the final shape [134]. The intrinsic anisotropic characteristics of CuS hexagonal crystal structure have the strong influence on the shapes of the products [134]. PEG is a dominant surfactant, which play the role in changing surface energies of growing crystal faces by selectively adsorbed on different faces of nuclei or seeds [133-134]. Growth in the [110] direction became faster and that in the [001] direction

was slower [135]. Hexaplates, surrounded by the (100), (010), (-110), (-100), (0-10) and (1-10) planes, were synthesized. Their sizes were also influenced by the concentration and diffusion of nuclei in the solutions. Solubilities, reactivities, diffusivities, and other chemical and physical properties of the reagents and the precursors (intermediates) play the role in the product morphologies, by influencing the growth and self-assemblies of nuclei [135].

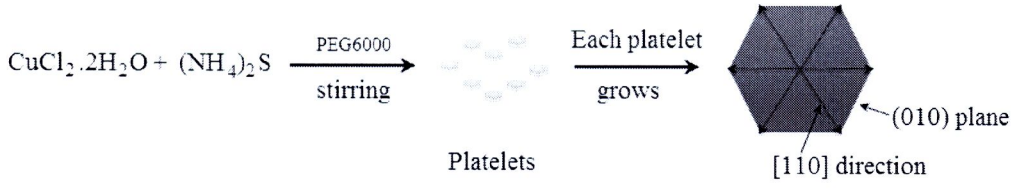

Figure 3.97 Formation mechanism for CuS hexaplates

When different amounts of PEG6000 with the same prolonged time of 5 h were used, different morphologies were synthesized (Figure 3.104, 3.105). For 1 g PEG6000, the product (Figure 3.104) was composed of non-uniform plates and nanoparticles, caused by the incomplete capping on the CuS crystallographic faces. When 10 g PEG6000 was used, nanoparticles were no longer detected and the plates shaped like a hexagon still exist in the product (Fig. 3.105), but these plates were in clusters. Thus, excess PEG6000 was not required.

Morphologies of the products synthesized at 200 ^{o}C for 5 h in the solutions containing different molecular weights (MWs) of 5 g PEG were also studied (Figure 3.106-3.109). By using PEG8000, the degree of HCOOH in stabilizing a pH of the solution became lessened. Thus formation mechanism changed. For PEG8000, individual nanoparticles and plate-shaped particles (Figure 3.106) with different

geometry were synthesized. In general, PEG chain molecules become lengthened with their heavier MWs. When PEGs with heavier MWs were used in the solutions, the degree or extent of these PEGs in prohibiting the growth of individual nanoparticles and plate-shaped particles became more intense. For PEG10000, their chain molecules were long enough to entangle these nuclei in the solution to form clusters of nuclei with active sites residing on their surfaces, at which the nuclei grew to form clusters of plate-shaped particles (Figure 3.107). These clusters gradually transformed into incomplete flower-like shapes for PEG12000 (Figure 3.108), and complete flower-like shapes for PEG20000 (Fig. 3.109) afterwards. These plates were self-assemble into clusters and flower-like clusters, in order to reduce their surface areas and to minimize the interfacial free energies [137].

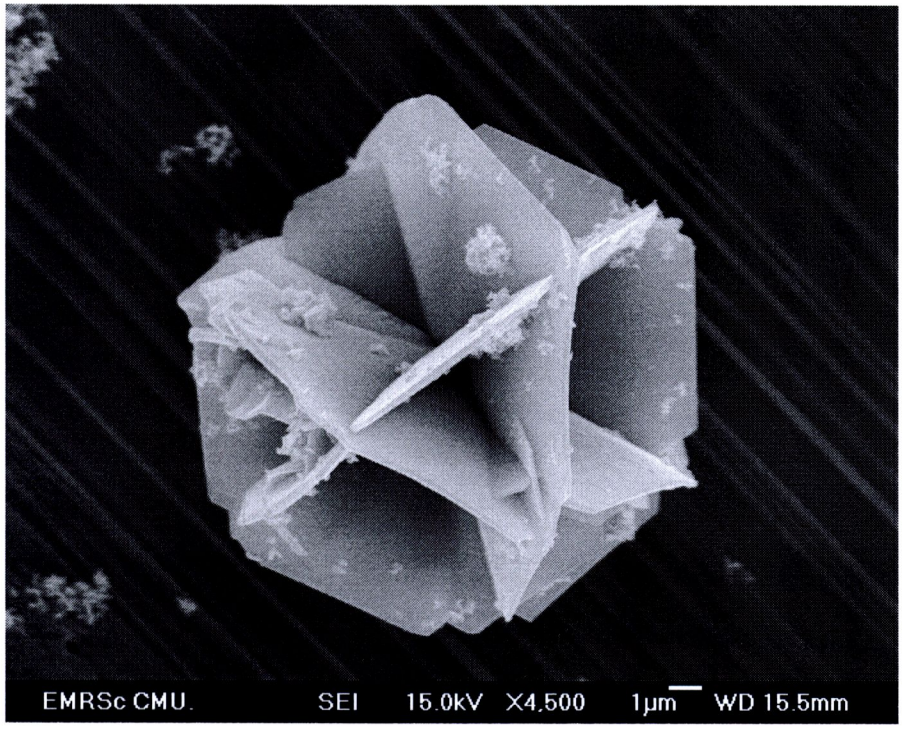

Figure 3.98 SEM image of the product synthesized in 5 g PEG6000-added solution containing HCOOH-free at 200 °C for 5 h

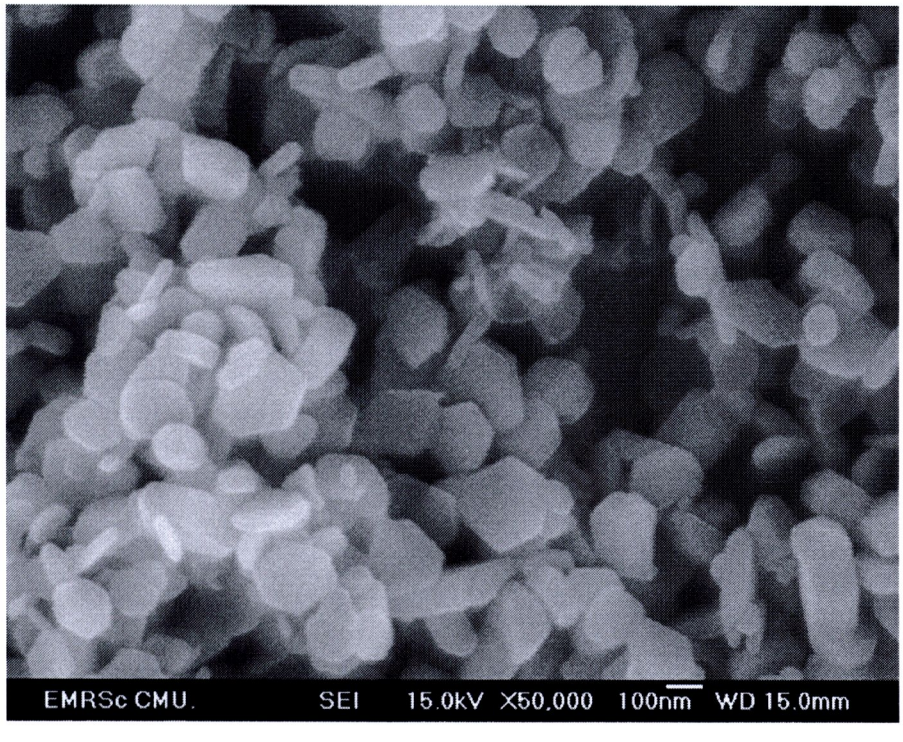

Figure 3.99 SEM image of the product synthesized in 5 g PEG6000-added solution containing 1.5 ml HCOOH at 200 °C for 5 h

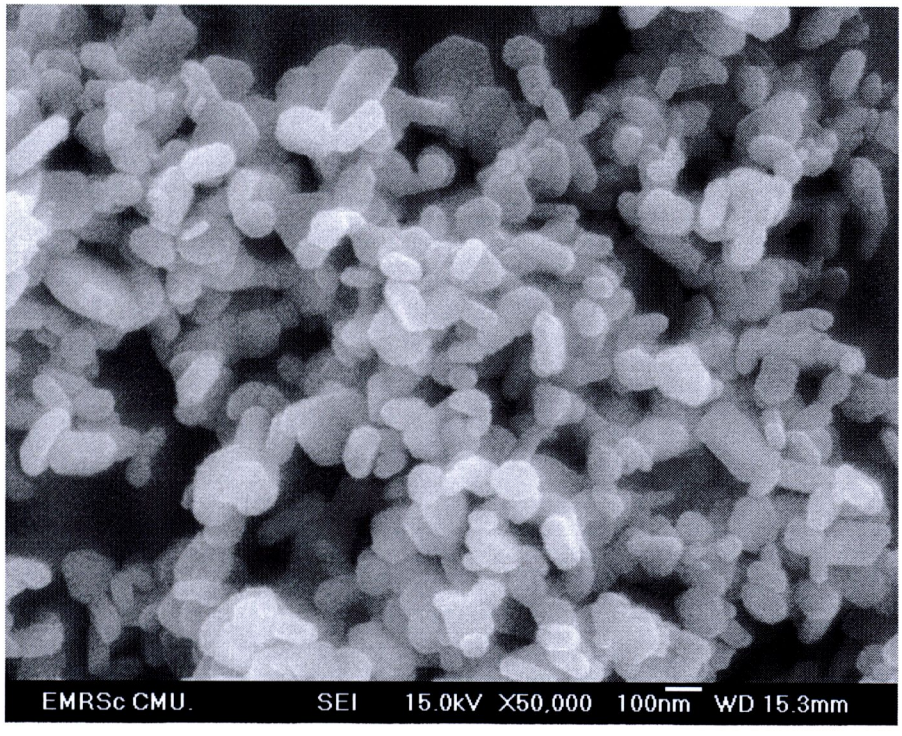

Figure 3.100 SEM image of the product synthesized in 5 g PEG6000-added solution containing 3.0 ml HCOOH at 200 °C for 5 h

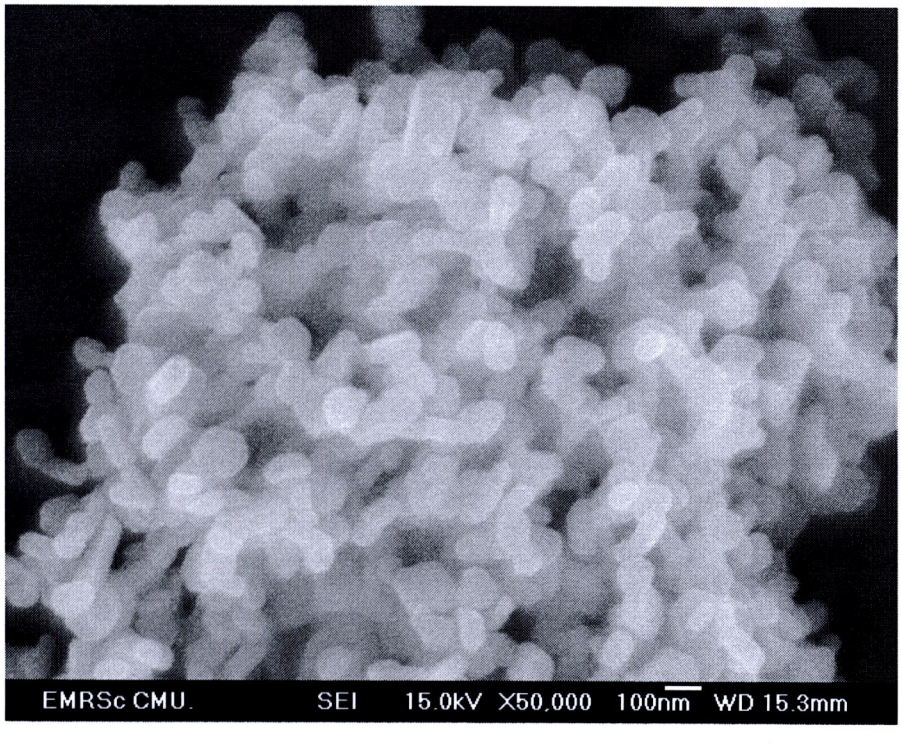

Figure 3.101 SEM image of the product synthesized in 5 g PEG6000-added solution containing 5.0 ml HCOOH at 200 °C for 5 h

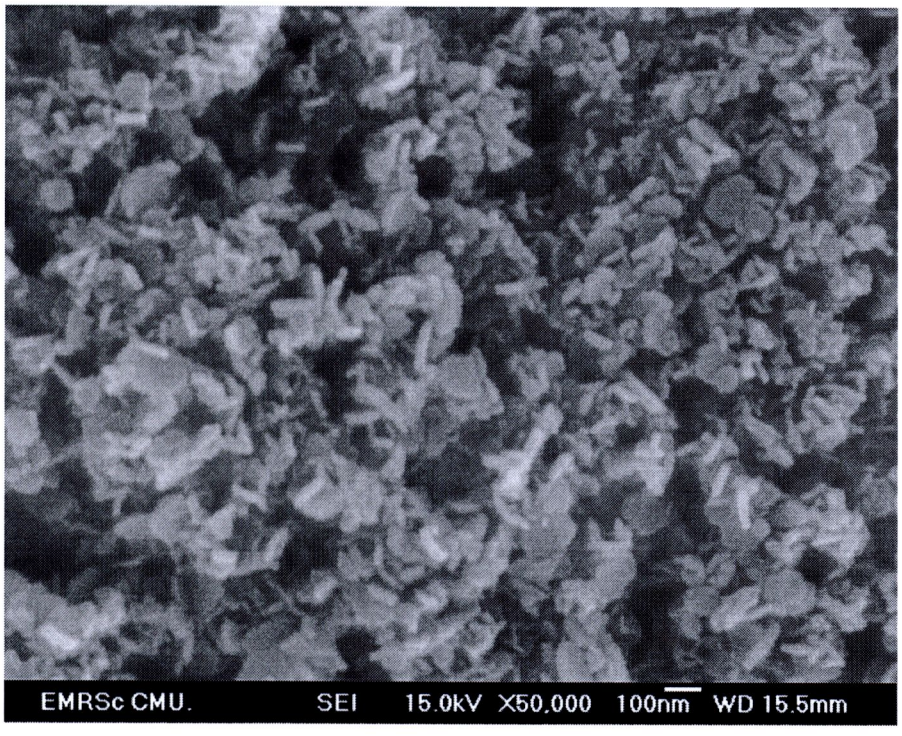

Figure 3.102 SEM image of the product synthesized in 5 g PEG6000-added solution containing 1.5 ml HCOOH at 200 °C for 1 h

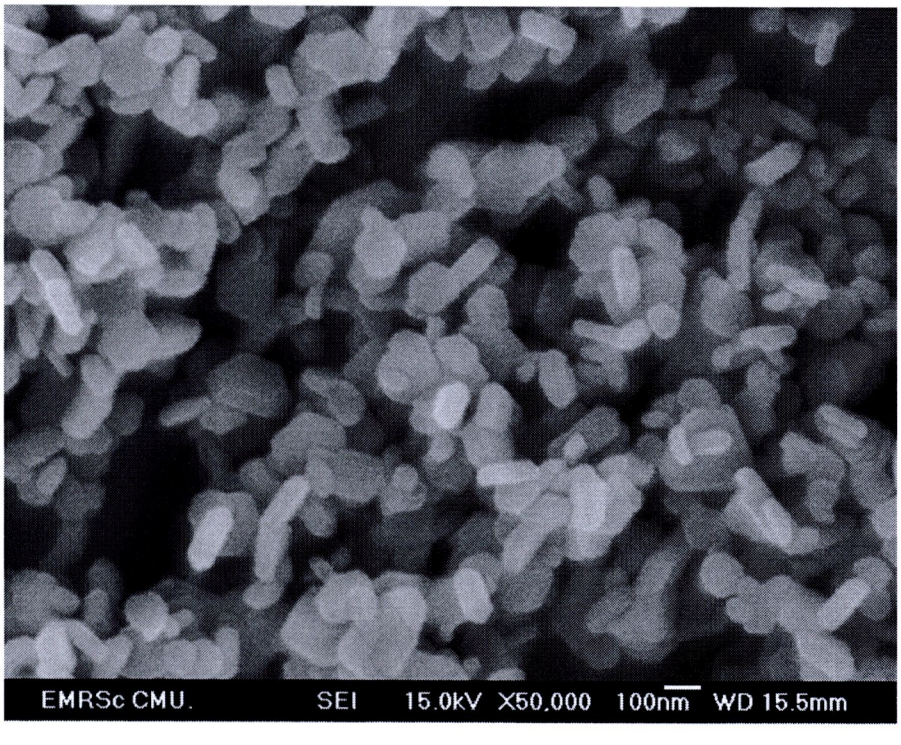

Figure 3.103 SEM image of the product synthesized in 5 g PEG6000-added solution containing 1.5 ml HCOOH at 200 °C for 3 h

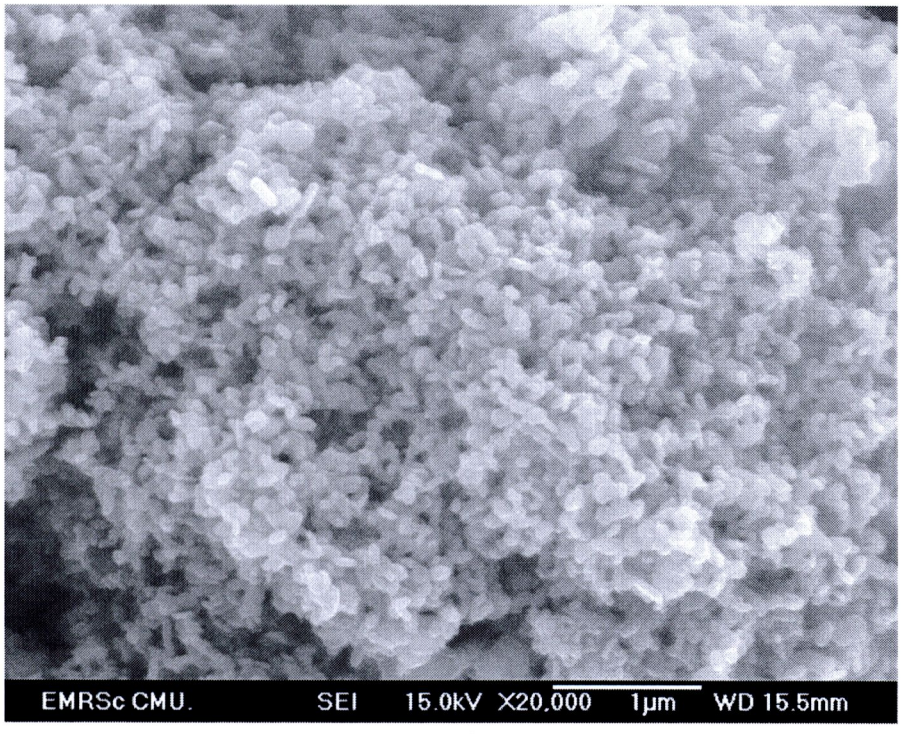

Figure 3.104 SEM image of the product synthesized in 1 g PEG6000-added solution containing 1.5 ml HCOOH at 200 °C for 5 h

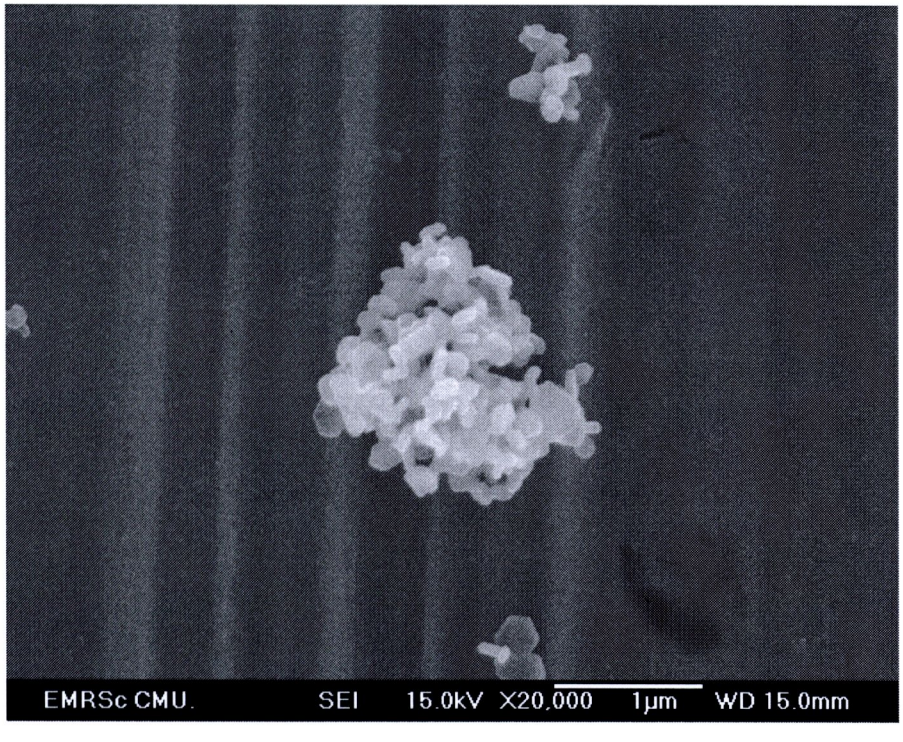

Figure 3.105 SEM image of the product synthesized in 10 g PEG6000-added solution containing 1.5 ml HCOOH at 200 °C for 5 h

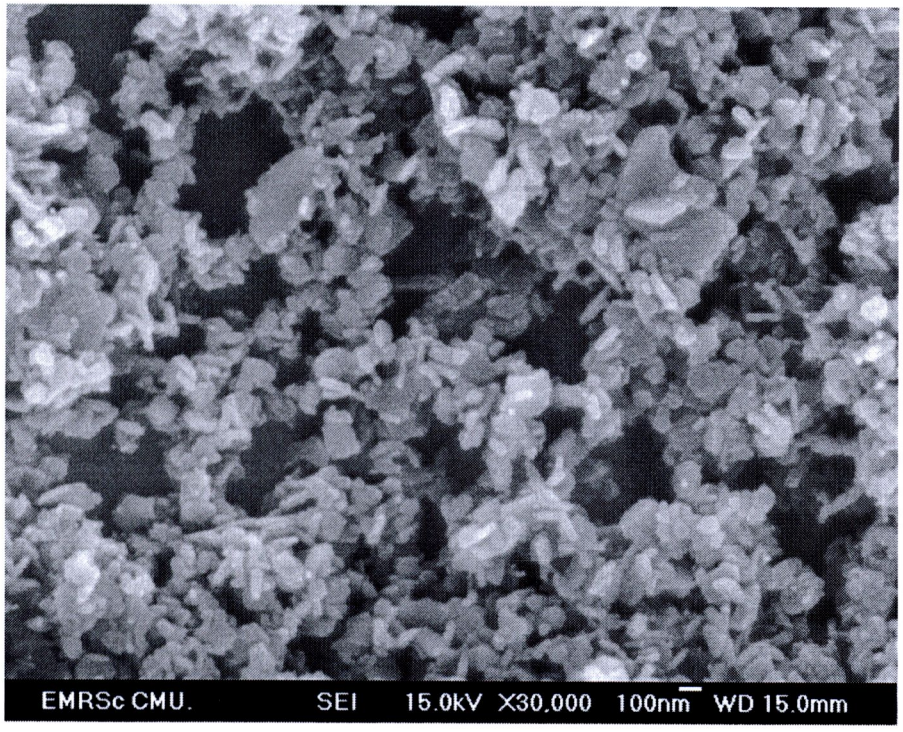

Figure 3.106 SEM image of the product synthesized in 5 g PEG8000-added solution containing 1.5 ml HCOOH at 200 °C for 5 h

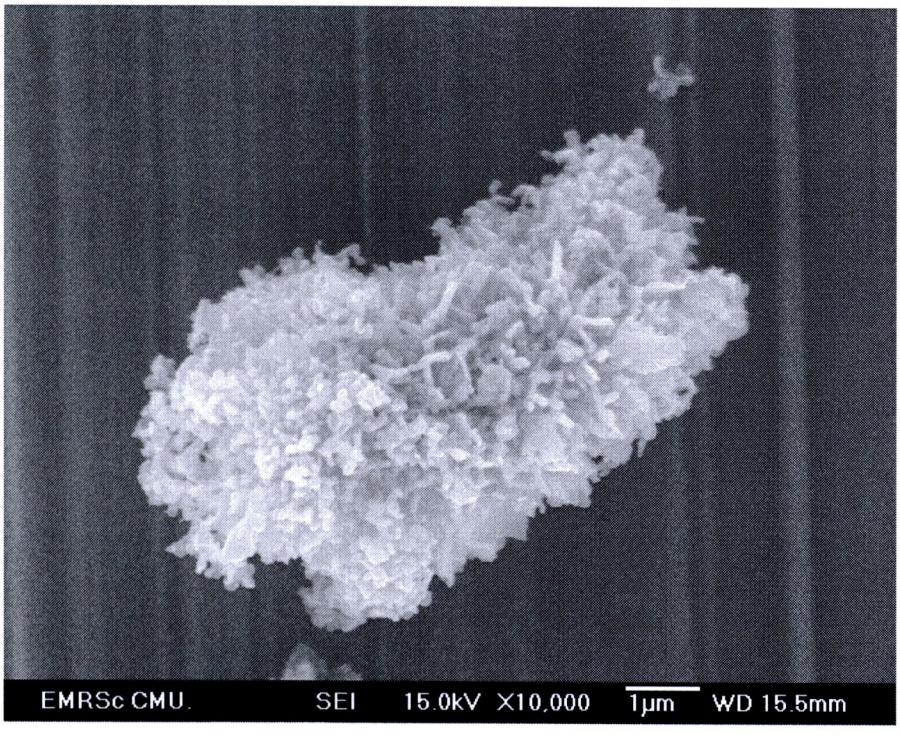

Figure 3.107 SEM image of the product synthesized in 5 g PEG10000-added solution containing 1.5 ml HCOOH at 200 °C for 5 h

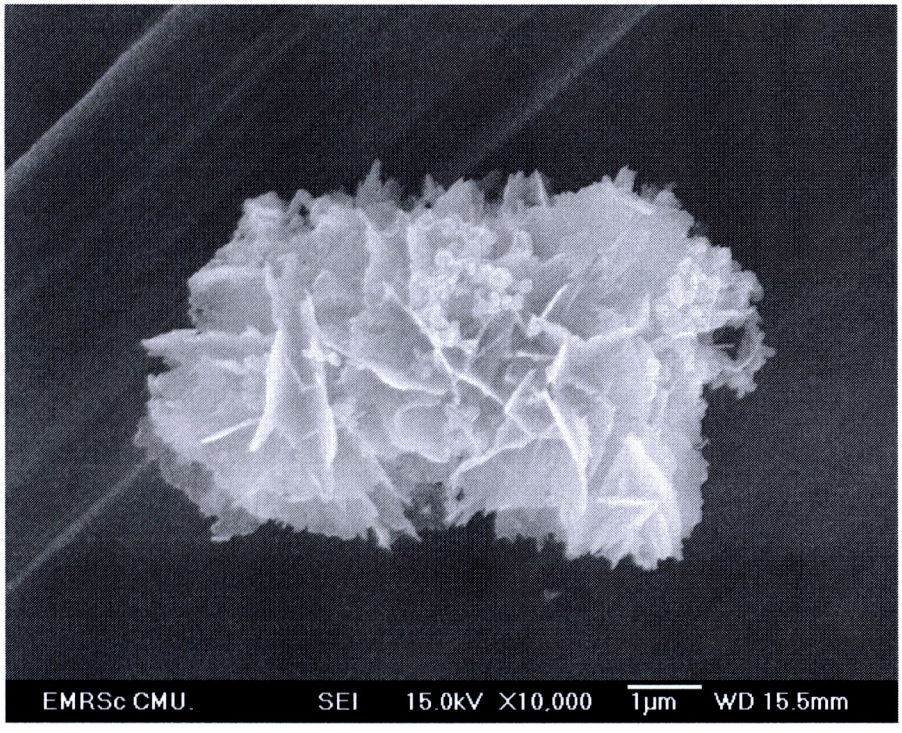

Figure 3.108 SEM image of the product synthesized in 5 g PEG12000-added solution containing 1.5 ml HCOOH at 200 °C for 5 h

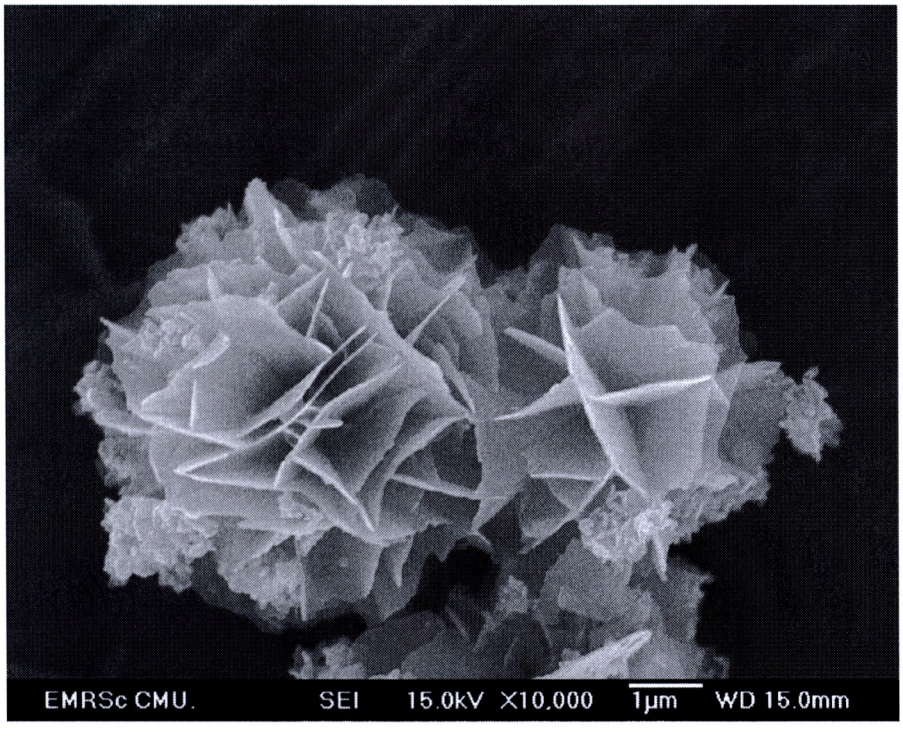

Figure 3.109 SEM image of the product synthesized in 5 g PEG20000-added solution containing 1.5 ml HCOOH at 200 °C for 5 h

3.3.4 Transmission Electron Microscopy (TEM), High Resolution Transmission Electron Microscopy (HRTEM) and selected area electron diffraction (SAED)

Figure 3.110-3.115 show TEM and HRTEM images, and SAED and simulated patterns of CuS hexagonal plates. TEM images show two primary orientations of the plate: flat-lying on (Figure 3.110) and edge-standing on (Fig. 3.111) the amorphous carbon coated-copper grid. The plate was in the shape of a hexagon with 167 nm in diameter and 22 nm thick. The (100) and (010) lattice planes with the same planar spaces of 3.3 Å were detected on the flat-lying (HRTEM) image (Figure 3.112). These two planes make an angle of 120 ° relative to each other, which is in accordance with the 120 ° basal plane of hexagonal structure. A number of parallel planes with 8.2 Å apart were also detected on the edge-standing (HRTEM) image (Figure 3.113). They correspond with the (002) crystallographic planes, to which the c axis of hexagonal structure was normal.

SAED pattern through a flat-lying hexaplate (Figure 3.114) shows regular hexagonal array of diffraction spots, corresponding to the basal plane of a hexagonal structure, with the electron beam in the [001] direction. This pattern corresponds to a single crystal of hexagonal structure covellite CuS [109]. A simulated electron diffraction pattern (Figure 3.115) appears as systematic arrays of spots, corresponding to the SAED pattern obtained from the experiment.

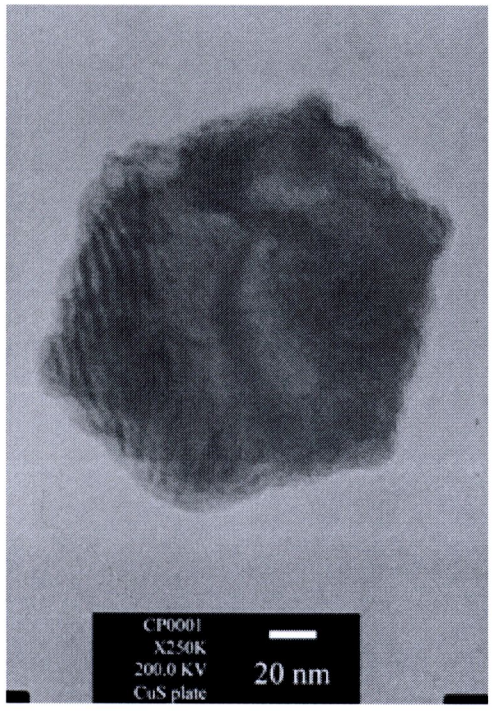

Figure 3.110 Flat-lying TEM image of CuS nanoplates in 5 g PEG6000-added solution containing 1.5 ml HCOOH at 200 °C for 5 h

Figure 3.111 Edge-standing TEM image of CuS nanoplates in 5 g PEG6000-added solution containing 1.5 ml HCOOH at 200 °C for 5 h

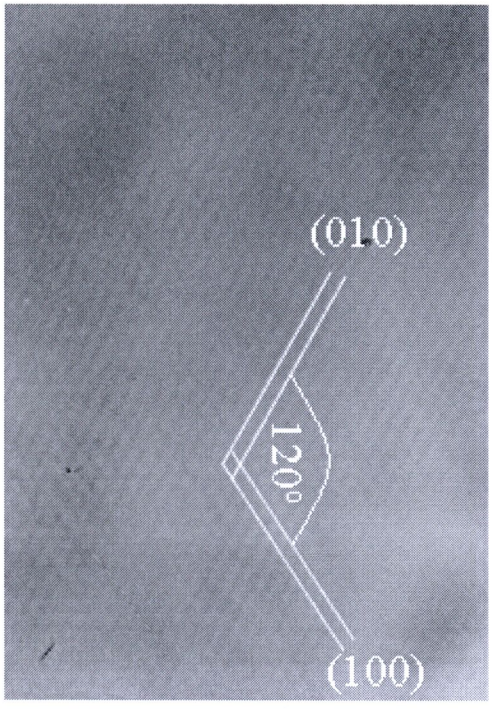

Figure 3.112 Flat-lying HRTEM image of CuS nanoplates in 5 g PEG6000-added solution containing 1.5 ml HCOOH at 200 °C for 5 h

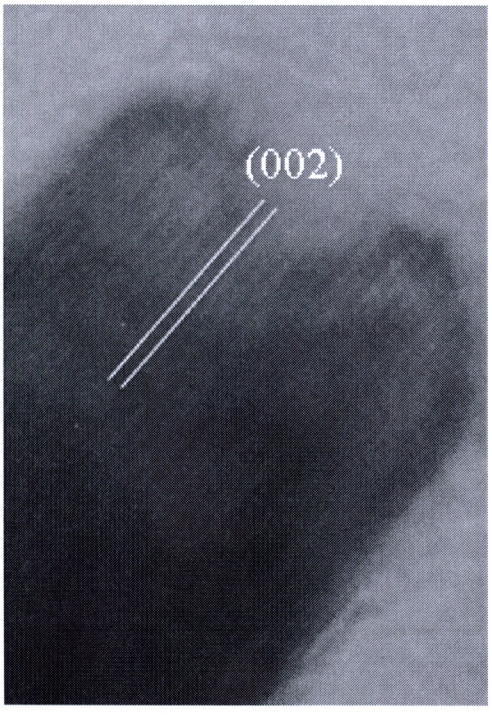

Figure 3.113 Edge-standing HRTEM image of CuS nanoplates in 5 g PEG6000-added solution containing 1.5 ml HCOOH at 200 °C for 5 h

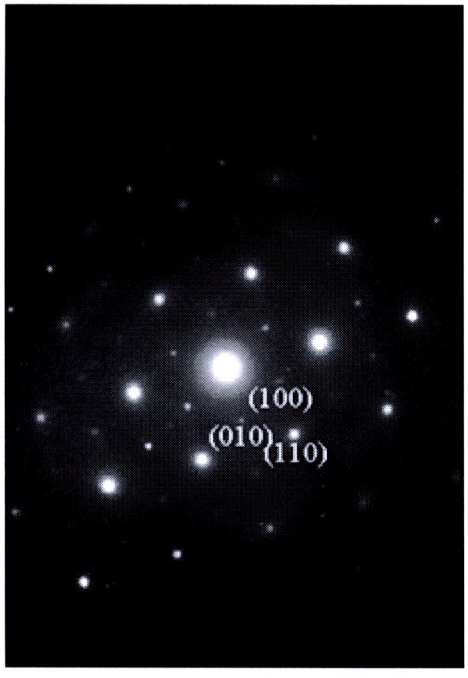

Figure 3.114 SAED pattern of CuS nanoplates in 5 g PEG6000-added solution containing 1.5 ml HCOOH at 200 °C for 5 h

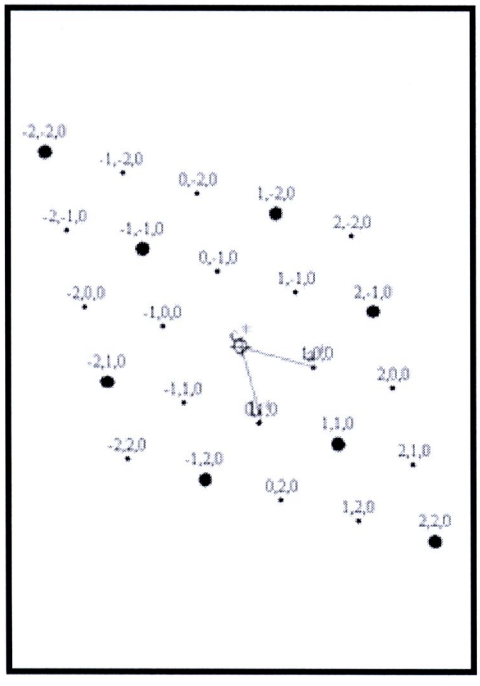

Figure 3.115 Simulated pattern of CuS nanoplates in 5 g PEG6000-added solution containing 1.5 ml HCOOH at 200 °C for 5 h

3.3.5 Optical properties

The optical properties of CuS hexaplates were investigated by UV-vis absorption and PL emission. Figure 3.116 shows UV-Vis absorption spectrum of CuS hexaplates dispersed in absolute ethanol, with its absorption edge at 610 nm (2.03 eV). A broad absorption peak of near-IR region indicates the presence of CuS (covellite) phase, which are in accordance with those obtained by other researcher [138]. PL spectrum of CuS hexaplates (Figure 3.117) was determined using a 300 nm (4.13 eV) excitation wavelength. Its emission peak is at 361 nm (3.43 eV), which is in accordance with that of CuS nanoplates at 339 nm (3.665 eV) determined by Zhang et al [136].

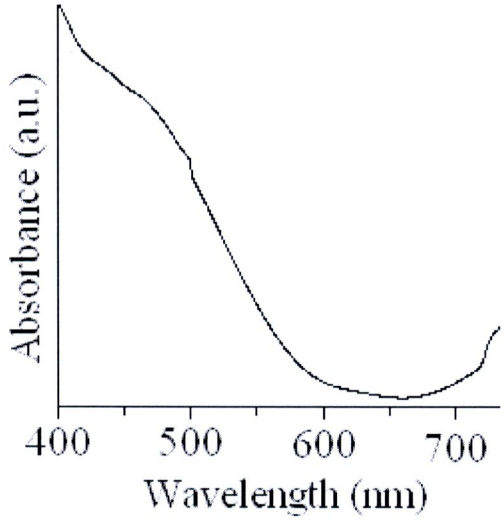

Figure 3.116 UV-vis absorption of CuS hexaplates, produced in 5 g PEG6000-added solution containing 1.5 ml HCOOH at 200 ^{o}C for 5 h

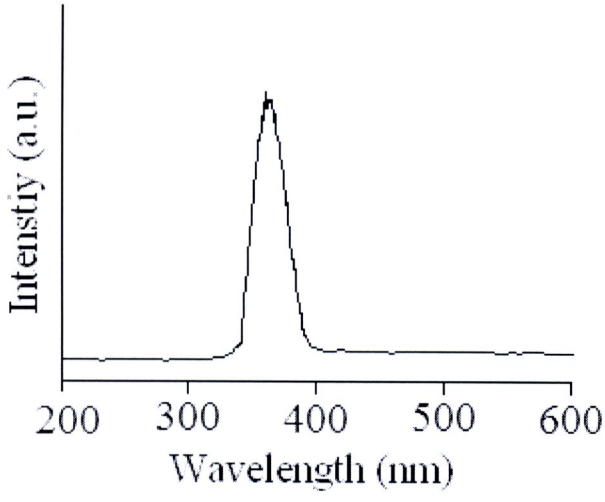

Figure 3.117 PL emission spectrum of CuS hexaplates, produced in 5 g PEG6000-added solution containing 1.5 ml HCOOH at 200 °C for 5 h

3.3.6 Utilization of CuS in solar cell

In this part, p-type CuS hexaplates was used as hole carrier in solid state DSSC. The solid-state DSSC was fabricated from transparency electrode coated on glass with a polymer-nanocomposite electrolyte containing iodine and p-type semiconductor (CuS) hexaplates. The composites are monolayer, intercalated between nanoporous ZnO base on Eosin Y dye, and Pt nanofilm acted as counter electrode (Figure 3.118a). In typical fabrication, The 1.5 cm x 2.5 cm FTO (F-doped SnO_2) was cleaned by acetone, dried by nitrogen blowing, and put in a quartz chamber containing 0.05 g Zn powder. Evacuation was done until the inside chamber was vacuum. The system was heated for 5 min to produce porous Zn film on the FTO substrate, and followed by heating it in 2.12 kPa absolute air pressure for 3 min to produce porous ZnO. Another FTO substrate was also coated with Pt on top. Then these two electrodes were composed to be a DSSC with different wt % CuS-PEG electrolyte in between. The test was done in a solar simulator (1,000 W Xenon lamp) at AM 1.5 (100 mW/cm^2).

After a photon is absorbed by the dye, the excited state is quenched by electron injection into the ZnO conduction band. The photo-oxidized dye is then regenerated by capture of an electron from the valence band of CuS, a process also referred to as hole injection. The two photoseparated charges then percolate through the two phases and, in the absence of recombination, reach the SnO_2 and back contact, respectively. Recombination consists of either (a) reduction of the oxidized dye by an electron from ZnO before hole injection into CuS regenerates the dye or (b) recombination of an electron from the ZnO with a hole in the CuS.

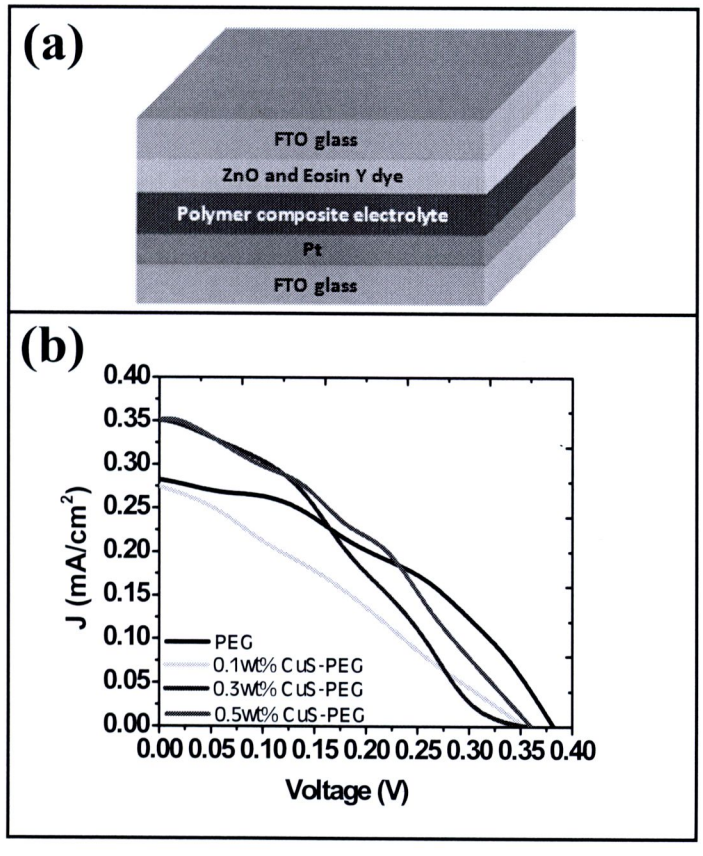

Figure 3.118 (a) A schematic diagram of our DSSC, (b) J-V curves of the DSSCs containing different wt% of CuS in electrolyte

Table 3.7 V_{oc}, J_{sc}, FF and η for different wt % CuS-PEG electrolytes

Electrolytes	V_{oc} (V)	J_{sc} (mA/cm^2)	FF	η (%)
PEG	0.382	0.282	0.410	0.044
0.1 wt% CuS-PEG	0.355	0.275	0.288	0.028
0.3 wt% CuS-PEG	0.357	0.351	0.306	0.038
0.5 wt% CuS-PEG	0.361	0.351	0.369	0.047

Figure 3.118b shows J-V curves of the solar cell containing different wt% CuS in electrolytes and their results are summarized in Table 3.5. It was found that the polymer nanocomposited electrolyte with different weight percent of CuS powder is correlated with the V_{oc}, I_{sc}, FF, and the efficiency. At 0.5 wt% CuS-PEG electrolyte, the performance shows at the best DSSC. This is because the filling of CuS nanoplates can increase the electron exchange in PEG network of electrolyte region and increase the diffusion of I_3 in the redox electrolyte. It may result the high J_{sc} less increase variation in V_{oc} of CuS-PEG. Generally, the high V_{oc} is attributed to low recombination rate, which is accounted by low series resistance $(R_s = (dV/dI)_{I=0})$ of cell under power density of the light was adjusted to 100 mW/cm^2 (AM 1.5). The slight increase of V_{oc} as increasing CuS contents in CuS-PEG may be ascribed to the low R_s of electrodes/electrolyte due to the interference of CuS in DSSCs.